



저작자표시-비영리-변경금지 2.0 대한민국

이용자는 아래의 조건을 따르는 경우에 한하여 자유롭게

- 이 저작물을 복제, 배포, 전송, 전시, 공연 및 방송할 수 있습니다.

다음과 같은 조건을 따라야 합니다:



저작자표시. 귀하는 원저작자를 표시하여야 합니다.



비영리. 귀하는 이 저작물을 영리 목적으로 이용할 수 없습니다.



변경금지. 귀하는 이 저작물을 개작, 변형 또는 가공할 수 없습니다.

- 귀하는, 이 저작물의 재이용이나 배포의 경우, 이 저작물에 적용된 이용허락조건을 명확하게 나타내어야 합니다.
- 저작권자로부터 별도의 허가를 받으면 이러한 조건들은 적용되지 않습니다.

저작권법에 따른 이용자의 권리는 위의 내용에 의하여 영향을 받지 않습니다.

이것은 [이용허락규약\(Legal Code\)](#)을 이해하기 쉽게 요약한 것입니다.

[Disclaimer](#)



저작자표시-비영리-변경금지 2.0 대한민국

이용자는 아래의 조건을 따르는 경우에 한하여 자유롭게

- 이 저작물을 복제, 배포, 전송, 전시, 공연 및 방송할 수 있습니다.

다음과 같은 조건을 따라야 합니다:



저작자표시. 귀하는 원저작자를 표시하여야 합니다.



비영리. 귀하는 이 저작물을 영리 목적으로 이용할 수 없습니다.



변경금지. 귀하는 이 저작물을 개작, 변형 또는 가공할 수 없습니다.

- 귀하는, 이 저작물의 재이용이나 배포의 경우, 이 저작물에 적용된 이용허락조건을 명확하게 나타내어야 합니다.
- 저작권자로부터 별도의 허가를 받으면 이러한 조건들은 적용되지 않습니다.

저작권법에 따른 이용자의 권리는 위의 내용에 의하여 영향을 받지 않습니다.

이것은 [이용허락규약\(Legal Code\)](#)을 이해하기 쉽게 요약한 것입니다.

[Disclaimer](#)





A THESIS  
FOR THE DEGREE OF DOCTOR OF PHILOSOPHY

**Investigation of Single Point Incremental Sheet  
Forming Process: Extraction of Constitutive  
Models and Parameters Optimization**

**Mohanraj Murugesan**

FACULTY OF MECHANICAL ENGINEERING

GRADUATE SCHOOL

JEJU NATIONAL UNIVERSITY

**August 2021**

# Investigation of Single Point Incremental Sheet Forming Process: Extraction of Constitutive Models and Parameters Optimization

**Mohanraj Murugesan**  
(Supervised by Professor Dong Won Jung)

A thesis submitted in partial fulfillment of the requirement for the degree of  
Doctor of Philosophy  
2021. 06

The thesis has been examined and approved.

.....  
**Prof. Taek Myung Hyun**  
Thesis Director

Faculty of Mechanical Engineering,  
Jeju National University

.....  
**Prof. Dong Won Jung**  
Thesis Committee Member & Supervisor

Faculty of Mechanical Engineering,  
Jeju National University

.....  
**Prof. Chang Nam Kang**  
Thesis Committee Member

Faculty of Mechanical Engineering,  
Jeju National University

.....  
**Prof. Ji-Hyun Jeong**  
Thesis Committee Member

Faculty of Mechanical Engineering,  
Jeju National University

.....  
**Prof. Chang-Whan Lee**  
Thesis Committee Member

Department of Mechanical Design and  
Manufacturing Engineering, Seoul  
National University of Science and  
Technology

June - 2021


Faculty of Mechanical Engineering  
GRADUATE SCHOOL  
JEJU NATIONAL UNIVERSITY

## Declaration of Authorship

I, MOHANRAJ MURUGESAN, declare that this thesis titled, "Investigation of Single Point Incremental Sheet Forming Process: Extraction of Constitutive Models and Parameters Optimization" and the work presented in it are my own. I confirm that:

- This work was done wholly or mainly while in candidature for a research degree at this University.
- Where any part of this thesis has previously been submitted for a degree or any other qualification at this University or any other institution, this has been clearly stated.
- Where I have consulted the published work of others, this is always clearly attributed.
- Where I have quoted from the work of others, the source is always given. With the exception of such quotations, this thesis is entirely my own research work.
- I have acknowledged all main sources of help.
- Where the thesis is based on work done by myself jointly with others, I have made clear exactly what was done by others and what I have contributed myself.

Signed:

  
MURUGESAN MOHANRAJ

Date:

2021. 07. 12



## *Abstract*

The incremental forming process (ISF) is one of the prominent sheet metal manufacturing techniques among the traditional forming methods; it's becoming more noticeable these days due to its flexibility for manufacturing complex parts without utilizing predefined forming dies. Besides, the ISF process has higher formability of formed parts at a low cost than the conventional sheet forming methods. Additionally, the consistent and reasonable work material characterization in both room and warm temperature conditions under various strain rates is remarkably essential for modeling the numerical simulation and optimizing the sheet metal forming process working parameters. This research work's contributions to the ISF process can be organized into the following sections: at first, the field emission scanning electron microscopy (FESEM) analysis combined with the energy-dispersive X-ray spectroscopy (EDS) technique is employed to conduct the elemental identification investigation. Secondly, the Digital Image Correlation (DIC) technique is used to investigate the work materials for assessing their material properties. For this purpose, the digital images at each deformation step, which provide complete displacement and strain data information until the fracture more accurately, are used. Further, the empirical models such as the original and modified Johnson-Cook models, modified Zerilli-Armstrong model, the strain-compensated Arrhenius-type constitutive equation, and hybrid machine learning model are proposed for describing the material flow behavior during hot deformation conditions. Overall, the proposed constitutive equation from the artificial neural network model combined with an optimization approach is proved to have good predictability in flow stress estimation. Eventually, the single incremental forming process (SPIF) is modeled using a customized vertical milling machine to investigate the SPIF process. The design of experiments (DOE) combined with the grey relational analysis (GRA), the response surface methodology

(RSM), and statistical analysis of variance (ANOVA) is adopted for determining the process parameter's influence on the material formability without producing a rupture. The DOE procedure, a face-centered central composite design, is adopted for the AA3003-H18 Al alloy sheets for conducting the tests. The RSM procedure is used for optimizing the process parameters and identify the optimal experimental conditions. The statistically proposed model is observed from the outcome to be in good agreement with the experimental measurements. ANOVA is conducted to explain the proposed model's adequacy and the input factor's influence on the output factor. The statistically proposed regression model is observed to agree with the experimental estimations, having a higher coefficient of determination ( $R^2$ ) (0.8931) with lower prediction error (2.78%). The process parameters, such as step size, feed rate, the interaction effect of tool radius and step size, positively influence the response variable. Similarly, the input factors are optimized using the Taguchi method to minimize the surface roughness of formed parts. Firstly, according to the smaller-the-better, the S/N ratios are estimated to make a response table for getting the optimum level of process parameters. Minimum surface roughness is accomplished when the vertical step-size is smaller, the feed-rate is high, and the forming tool radius is high. The optimum level setting is acquired at 3.0 mm of forming tool radius (level 3), 3000 rpm of spindle speed (level 1), 0.10 mm of vertical step size (level 1), and 2000 mm/min of feed rate (level 4). The ANOVA results such as  $p$ -test and  $F$ -test revealed that vertical step-size, feed-rate, and tool radius significantly affect surface roughness. In contrast, the spindle speed is witnessed to have no significant influence on surface roughness. The Taguchi design results conferred better agreement with the actual measurements with moderate model error ( $\approx 1.8\%$ ). Additionally, the microstructural evaluation revealed that the thinning behavior tended to increase as forming depth reached its maximum; the material deformation was also observed to be uniform and homogeneous.

## *Abstract (Hanguk)*

ISF(점진 성형 공정)는 기존의 성형 방법 중 대표적인 판금 제조 기법 중 하나다. 사전 정의된 성형 다이를 활용하지 않고 복잡한 부품을 제조할 수 있는 유연성으로 인해 오늘날 더욱 주목을 받고 있다. 게다가, ISF 공정은 기존의 시트 성형 방법보다 저렴한 비용으로 성형 부품의 성형성이 우수하다. 또한 다양한 변형을 하에서 실내 및 온열 온도 조건 모두에서 일관되고 합리적인 작업 재료 특성은 수치 시뮬레이션을 모델링하고 판금 성형 공정 작업 매개 변수를 최적화하는 데 매우 중요하다. 본 연구의 ISF 공정에 대한 기여는 처음에는 field emission scanning electron microscopy (FESEM) 분석과 에너지 분산 X선 스펙트럼 분석(EDS) 기법을 결합하여 소자 식별 조사를 실시하는 섹션으로 나눌 수 있다. 둘째, DIC (Digital Image Correlation) 기법을 사용하여 재료 특성을 평가하기 위한 작업 재료를 조사한다. 이를 위해 파단까지의 변위 및 변형 데이터 정보를 제공하는 각 변형 단계의 디지털 영상이 사용된다. 또한, 고온 변형 조건에서의 재료 흐름 거동을 설명하기 위해 최초 및 수정된 Johnson-Cook 모델, 수정된 Zerilli-Armstrong 모델, 변형을 보정 Arrhenius형 구성 방정식, 하이브리드 기계 학습 모델 등의 경험적 모델을 제안한다. 전반적으로, 인공지능망 모델의 제안 구성 방정식은 최적화 접근법과 결합된 흐름 응력 추정에 좋은 예측 가능성을 가지고 있는 것으로 입증되었다. 결국, 단일 점진 성형 공정(SPIF)은 SPIF 공정을 조사하기 위해 맞춤형 수직 밀링 머신을 사용하여 고안되었다. Grey relational analysis (GRA), response surface methodology (RSM), statistical analysis of variance (ANOVA)과 결합된 실험 설계(DOE)는 공정 매개변수가 파열을 일으키지 않는 상황에서 재료 성형성에 미치는 영향을 위해 채택되었다. 실험 실행을 위한 AA3003-H18 Al 합금 시트에 표면 중심의 중앙



합성 설계인 DOE 절차가 채택되었다. RSM 절차는 공정 변수를 최적화하고 최적의 실험 조건을 식별하는 데 사용된다. 통계적으로 제안된 모델은 실험 측정과 잘 일치하는 결과로부터 관찰된다. ANOVA 분석은 제안된 모형의 적합성과 입력 인자가 출력 인자에 미치는 영향을 설명하기 위해 수행된다. 통계적으로 제안된 회귀 모형은 더 높은 결정 계수( $R^2$ )(0.8931)와 더 낮은 예측 오차(2.78%)를 갖는 실험 추정과 일치하는 것으로 관찰된다. 스텝 크기, 이송 속도, 공구 반지름의 상호작용 효과, 스텝 크기와 같은 프로세스 파라미터는 반응 변수에 긍정적인 영향을 미친다. 마찬가지로 입력 계수는 Taguchi 방법을 사용하여 최적화되어 성형 부품의 표면 거칠기를 최소화한다. 첫째, 작을수록, S/N 비율은 프로세스 매개변수의 최적 수준을 얻기 위한 반응 표를 만드는 것으로 추정된다. 최소 표면 거칠기는 수직 스텝 크기가 작고 이송 속도가 높으며 성형 공구 반경이 높을 때 이루어진다. 최적의 레벨 설정은 성형 공구 반경 3.0mm (레벨 3), 스피들 속도 3000rpm (레벨 1), 수직 스텝 크기 0.10mm (레벨 1), 이송 속도 2000mm/min (레벨 4)에서 획득한다. P-시험 및 F-시험 등의 분산 분석 결과에 따르면 수직 단계 크기, 공급 속도 및 공구 반경은 표면 거칠기에 상당한 영향을 미친다. 반면, 스피들 속도는 표면 거칠기에 큰 영향을 미치지 않는 것으로 확인되었다. Taguchi 설계 결과는 중간 정도의 모형 오차(1.8%)를 갖는 실제 측정값과 더 잘 일치하는 결과를 얻었다. 또한 미세구조 평가 결과 형성 깊이가 최대에 도달하면 박리 거동이 증가하는 경향이 있었으며 재료 변형도 균일하고 균일한 것으로 관찰되었다.

## *Acknowledgements*

Foremost, I would like to express my sincere gratitude to my advisor, Professor Dong Won Jung, for his continuous support of my Ph.D. study and research, for his patience, motivation, enthusiasm, and immense knowledge. His guidance helped me in all the time of research and writing of this thesis. I could not have imagined having a better advisor and mentor for my Ph.D. research. I would also like to thank my Indian Prof. V. R. Sanal Kumar, and the rest of my thesis committee: Prof. Chang-Whan Lee, Prof. Myung Taek Hyun, Prof. Chang Nam Kang, and Prof. Ji Hyun Jeong, for their encouragement, and challenging questions.

My sincere thanks also goes to Professor Chang-Whan Lee and his laboratory students for extending me their cooperation to perform extensive experiments. I thank my fellow labmates: Muhammad Sajjad, Krishna Singh Bhandari, and Kang Ji Yun, for the inspiring discussions, and for all the fun we have had in the last three years. Also, I thank my friends at JNU: Dhanasekar, Natarajan, Ganaselvan, Abisek, Karthik, Parthiban, Vimal, Sindhuja, Karthikeyan, Alluri, and Vivek.

Last but not least, I would like to thank my family: my parents Murugesan Pon-nusamy and Arivukkannu Murugesan, for giving birth to me in the first place and supporting me mentally throughout my life. Also, I express my thanks to my family members: Chinnathambi, Nayagam, Thamizhmani, Chinna Pillai, Pazhaniyandi, Ananthraj Murugesan, Elayaraja, Elakkiya, Sandhiya, Gayathiri, Ranjith, Pugazh, Ela, Thamizh, Arun Kumar, Ezhil, Mari, Nethra, Sudhan, Sakthi, for their support and valuable prayers, caring, and sacrifices for educating and preparing me for my future. Finally, to my caring, loving, and supportive wife, Abitha Mohanraj: my deepest gratitude. Your encouragement when the times got rough is much appreciated and duly noted. It was a great comfort and relief to know that you were willing to provide management of our household activities while I completed my work. My heartfelt thanks.



# Contents

<b>Declaration of Authorship</b>	<b>iii</b>
<b>Abstract</b>	<b>v</b>
<b>Acknowledgements</b>	<b>vii</b>
<b>1 Single Point Incremental Forming Process</b>	<b>1</b>
1.1 Background . . . . .	1
1.1.1 Cold Incremental Forming Process . . . . .	1
1.1.2 Hot Incremental Forming Process . . . . .	6
1.2 Organization of the Dissertation . . . . .	8
1.3 Toolpath Strategies . . . . .	9
1.4 Surface Quality . . . . .	12
1.5 Applications . . . . .	13
1.6 Effects of Process Parameters . . . . .	14
1.7 Process Modeling and Simulation . . . . .	15
1.8 Selection of Lubrication . . . . .	16
1.9 Material Characterization . . . . .	21
1.9.1 Material Test . . . . .	21
1.9.2 Uniaxial Tensile Test . . . . .	22
1.9.3 Measurements of Strain-hardening Models . . . . .	25
1.9.4 Plastic Anisotropy . . . . .	26

1.9.5	Hot Tensile Test of AISI-1045 Steel . . . . .	29
1.9.6	Microstructural Characterization . . . . .	31
1.10	Conclusions . . . . .	34
<b>2</b>	<b>Johnson-Cook Material and Failure Models</b>	<b>35</b>
2.1	Summary . . . . .	35
2.2	Introduction . . . . .	36
2.3	Johnson-Cook Material Model . . . . .	38
2.3.1	Determination of Material Constants B and n . . . . .	39
2.3.2	Determination of Material Constant C . . . . .	40
2.3.3	Determination of the Material Constant, m . . . . .	41
2.4	Johnson-Cook Damage Model . . . . .	44
2.5	Discussion . . . . .	48
2.6	Conclusions . . . . .	53
<b>3</b>	<b>Modified Johnson-Cook and Zerilli-Armstrong Models</b>	<b>55</b>
3.1	Summary . . . . .	55
3.2	Introduction . . . . .	56
3.3	Modified Johnson-Cook model . . . . .	58
3.3.1	Determination of constants $A_1, B_1, B_2$ . . . . .	58
3.3.2	Determination of constant $C_1$ . . . . .	59
3.3.3	Determination of constants $\lambda_1, \lambda_2$ . . . . .	60
3.4	Modified Zerilli-Armstrong Model . . . . .	61
3.4.1	Determination of constants $C_2$ and $n$ . . . . .	63
3.4.2	Determination of constants $C_3$ and $C_4$ . . . . .	64
3.4.3	Determination of constants $C_5$ and $C_6$ . . . . .	66
3.5	Discussion . . . . .	68
3.6	Conclusions . . . . .	74

<b>4 Arrhenius-Type Constitutive and Artificial Neural Network Models</b>	<b>77</b>
4.1 Summary . . . . .	77
4.2 Introduction . . . . .	78
4.3 Strain Compensated Constitutive Equation . . . . .	81
4.3.1 Arrhenius-Type Constitutive Equation . . . . .	81
4.3.2 Strain Compensation . . . . .	84
4.3.3 Constitutive Model Verification . . . . .	85
4.4 Artificial Neural Network Model . . . . .	87
4.4.1 Proposing Flow Stress Model using ANN-BP Algorithm . . . . .	87
4.4.2 Optimization Procedures for Obtaining the Best ANN-BP Model . . . . .	90
4.5 Conclusions . . . . .	95
<b>5 SPIF Process Optimization using Response Surface Methodology</b>	<b>99</b>
5.1 Summary . . . . .	99
5.2 Introduction . . . . .	100
5.3 Experimental Procedures . . . . .	101
5.4 Design of Experiments . . . . .	103
5.5 Grey Relational Analysis . . . . .	105
5.6 Response Surface Methodology . . . . .	110
5.7 Results and Discussion . . . . .	112
5.8 Conclusions . . . . .	122
<b>6 Taguchi Method in Optimization of Surface Roughness</b>	<b>125</b>
6.1 Summary . . . . .	125
6.2 Introduction . . . . .	126
6.3 Experimental Design using Taguchi method . . . . .	127
6.4 Microstructure Evaluation of AA5052-H32 material in SPIF Process . . . . .	132
6.5 Microstructure Evaluation of AA3003-H18 material in SPIF Process . . . . .	135

6.6	Conclusions	137
<b>7</b>	<b>Conclusions and Future Work</b>	<b>139</b>
7.1	Conclusions	139
7.2	Suggestions for the Future Work	142
	<b>Bibliography</b>	<b>145</b>

# List of Figures

1.1	Single-point incremental forming process: 1–blank, 2–base support, 3–grip support, 4–forming tool, 5–blank initial position. . . . .	2
1.2	Experimental set-up of single-point incremental forming process. . .	2
1.3	Incrementally formed parts from SPIF process. . . . .	3
1.4	Two-point incremental forming process with partial die support: 6–partial die. . . . .	4
1.5	Two-point incremental forming process with specific die support: 7–specific die. . . . .	4
1.6	Two-point incremental forming process with counter tool support: 8–forming tool. . . . .	5
1.7	Hot incremental forming process. (a) Electric current; (b) Induction heating. . . . .	7
1.8	Tool-path options. (a) Spiral; (b) Contoured; (c) Stepped. . . . .	11
1.9	Surface quality evaluation. . . . .	13
1.10	Real-time applications of incremental forming process. . . . .	14
1.11	Contour plots of 45° pyramid geometry: (a) Forming depth; (b) Thinning behavior; (c) Strain; (d) Stress. . . . .	17
1.12	(a) Profile comparison of formed pyramid shape against real experiment and expected geometry (45°); (b) Thickness measurement (Murugesan, Sajjad, and Jung, 2020b). . . . .	17

1.13	Contour plots of 60° pyramid geometry: (a) Forming depth; (b) Thinning behavior; (c) Strain; (d) Stress. . . . .	18
1.14	(a) Profile comparison of formed pyramid shape against real experiment and expected geometry (60°); (b) Thickness measurement (Murugesan, Sajjad, and Jung, 2020b). . . . .	18
1.15	(a) Lubricants used; (b) Temperature comparison plot. . . . .	19
1.16	2D surface roughness profile of the formed material using different lubricants from the 3D nano profiler: (a) Original surface; (b) Grease; (c) Oil; (d) Combination of oil and grease. . . . .	20
1.17	Field emission scanning electron microscopy (FESEM) analysis (a) Microstructure observation at initial state; (b) Microstructure observation after fracture; (c) Tested samples. . . . .	22
1.18	Energy dispersive X-ray spectroscopy (EDS) analysis (a) Element spectrum corresponding to AA5052-H32 material; (b) EDS elemental mapping images showing the distribution of chemical elements. . . . .	23
1.19	(a) Experimental setup used for the uniaxial tension test with Aramis; (b) Yield and tensile strength data at 0°, 45° and 90° to the RD; (c) Major strain measurements by Digital Image Correlation (DIC) just before and after fracture. . . . .	25
1.20	Experimental set-up. (a) Test machine; (b) Specimen with thermocouples. . . . .	31
1.21	True stress-strain data obtained from hot tensile tests. . . . .	32

1.22	Micro-structure mapping images of AISI-1045 medium carbon steel material at deformation temperature (850 °C). (a–d) 0.05 s <sup>-1</sup> ; (e–h) 0.1 s <sup>-1</sup> ; (i–l) 0.5 s <sup>-1</sup> ; (m–o) 950 °C/0.5 s <sup>-1</sup> ; observation by field emission scanning electron microscopy (FESEM) and energy dispersive X-ray spectroscopy (EDS) on various magnifications (Murugesan and Jung, 2019a; Murugesan and Jung, 2019b; Murugesan, Sajjad, and Jung, 2019a; Murugesan, Sajjad, and Jung, 2020c).	33
2.1	Relationship between $\ln(\sigma - A)$ and $\ln\dot{\epsilon}^*$ under the reference conditions.	40
2.2	Relationship between $\frac{\sigma}{(A+B\epsilon^n)}$ and $\ln\dot{\epsilon}^*$ under the reference conditions.	41
2.3	Relationship between $\ln\left[1 - \frac{\sigma}{(A+B\epsilon^n)}\right]$ and $\ln T^*$ under the reference conditions.	43
2.4	Experimental set-up to perform tension test at room temperature. (a) Test machine; (b) Un-notched and pre-notched specimens.	46
2.5	Finite element models. (a) Fine mesh in notching region; (b) Stress estimation region.	47
2.6	Relationship plot of strain to fracture and stress triaxiality.	48
2.7	Comparison between experimental and predicted flow stress data using the modified Johnson-Cook model.	50
2.8	Relationship plots.	52
3.1	Relationship between $\sigma$ and $\epsilon$ at reference conditions.	59
3.2	Relationship between $\sigma/(A_1 + B_1\epsilon + B_2\epsilon^2)$ and $\ln\dot{\epsilon}^*$ .	60
3.3	Relationship between $\lambda$ and $\ln\dot{\epsilon}$ .	61
3.4	$\ln\left\{\sigma/(A_1 + B_1\epsilon + B_2\epsilon^2)(1 + C_1 \ln\dot{\epsilon}^*)\right\}$ and $T^*$ . (a) $\dot{\epsilon}=0.05\text{ s}^{-1}$ ; (b) $\dot{\epsilon}=0.1\text{ s}^{-1}$ ; (c) $\dot{\epsilon}=0.5\text{ s}^{-1}$ ; (d) $\dot{\epsilon}=1.0\text{ s}^{-1}$ .	62
3.5	Relationship between $\ln\sigma$ and $T^*$ .	64
3.6	Relationship between $\ln(\exp(I_1) - C_1)$ and $\ln\dot{\epsilon}$ .	65

3.7	Relationship between $S_1$ and $\epsilon$ . . . . .	65
3.8	Relationship between $\ln\sigma$ and $\ln\dot{\epsilon}^*$ at $\epsilon=0.15$ and $T=1123$ K. . . . .	66
3.9	Flow chart of optimization procedure. . . . .	67
3.10	Relationship between $S_2$ and $\ln\sigma$ at $\epsilon=0.175$ . . . . .	68
3.11	Comparison plot using modified Johnson–Cook (JC) model. (a) 923 K ; (b) 1123 K ; (c) 1223 K ; (d) correlation plot. . . . .	72
3.12	Comparison plot using modified Zerilli-Armstrong (ZA) model. (a) 923 K ; (b) 1123 K ; (c) 1223 K ; (d) correlation plot. . . . .	73
4.1	Relationship plots of $\sigma$ and $\epsilon$ at $\epsilon = 0.02$ (a) $\ln\dot{\epsilon}$ and $\ln\sigma$ ; (b) $\ln\dot{\epsilon}$ and $\sigma$ . . . . .	83
4.2	Relationship plot of $\sigma$ and $\dot{\epsilon}$ at $\epsilon = 0.02$ (a) $\ln\dot{\epsilon}$ and $\ln(\sinh(\alpha\sigma))$ ; (b) $10^3/T$ and $\ln(\sinh(\alpha\sigma))$ . . . . .	84
4.3	Correlation plot of stress and strain rate at $\epsilon = 0.02$ . . . . .	84
4.4	Comparison plot (a) $0.05 \text{ s}^{-1}$ ; (b) $0.1 \text{ s}^{-1}$ ; (c) $0.5 \text{ s}^{-1}$ ; (d) $1.0 \text{ s}^{-1}$ . . . . .	86
4.5	Back-propagation artificial neural network (BP-ANN) architecture for flow stress prediction (supervised learning). . . . .	88
4.6	BP-ANN model with an optimization procedures (OP) for flow stress prediction. . . . .	92
4.7	Flow chart of optimization procedures. . . . .	93
4.8	Comparison between experimental and predicted flow stress data using BP-ANN/OP model with TANSIG. . . . .	95
4.9	(a) Correlation plot; (b) Residual plot of an ANN-BP model; (c) Residual plot of an optimized ANN-BP model. (inset histogram plots). . . . .	96
4.10	Graphical validation. (a) BP-ANN and BP-ANN/OP models comparison at various strain rates; (b) Prediction error comparison for proposed models. . . . .	97



5.1	Experimental procedures of the single-point incremental forming process. . . . .	102
5.2	(a) Flow chart of experimental design process; (b) CCF design; (c) truncated conical geometry. . . . .	105
5.3	Incrementally formed truncated conical shape parts and thickness measurement. . . . .	114
5.4	Estimated shape error using the ATOS 3D scanner. (a) 60°; (b) 30°. . .	115
5.5	Full model. (a) correlation plot; (b) residual plot; (c) residual plot of reduced model. . . . .	116
5.6	Process parameters vs. GRG values: (a) main effects; (b) interaction effects. . . . .	119
5.7	(a) Scatter plot of observed data; (b) Measured vs. predicted data of GRG value. . . . .	121
6.1	Experimental set-up of single-point incremental forming process. . .	127
6.2	Main Effects Plot of S/N ratios. . . . .	129
6.3	(a) SPIF process illustration and final part; (b) microstructure of aluminum alloy (AA3003) material at various forming stages, observation by FESEM at 500 $\mu\text{m}$ magnification. . . . .	133
6.4	Microstructure observation of aluminum alloy (AA3003) material by FESEM at various magnifications at: (a) location 2; (b) location 3. . .	134
6.5	FESEM images at various magnifications: (a) surface from oil-grease lubricant used; (b) unfractured scanned surface from 60° part; (c) unfractured scanned surface from 30° part; (d) fractured surface. . . . .	136



## List of Tables

1.1	Model coefficients of Ramberg-Osgood model. . . . .	26
1.2	Mechanical properties of the AA5052-H32 material. . . . .	28
1.3	Mechanical properties of the AA3003-H18 material. . . . .	29
1.4	Mechanical properties of the AZ31B material. . . . .	29
1.5	Chemical composition of AISI-1045 medium carbon steel (in wt.%). . . . .	30
2.1	JC material model parameters of AISI-1045 steel. . . . .	43
2.2	Stress triaxiality data obtained from FE simulations. . . . .	47
2.3	Johnson-Cook fracture model parameters. . . . .	48
2.4	Statistical measurements of optimized JC model. . . . .	49
3.1	Parameters of AISI-1045 steel for the modified ZA model. . . . .	69
3.2	Statistical measurements of modified JC model. . . . .	70
3.3	Statistical measurements of modified ZA model. . . . .	70
3.4	Statistical parameters estimation from random experiments at deformation temperature 1023 K. . . . .	71
4.1	Estimated coefficients of fitted empirical models. . . . .	85
4.2	Estimated statistical values of the conventional Arrhenius-type constitutive model. . . . .	86
4.3	Estimated statistical values of the modified Arrhenius-type constitutive model. . . . .	87

4.4	Network model instructions used for constructing flow stress model.	89
4.5	Computed statistical parameters from an ANN-BP model. . . . .	91
4.6	Statistical parameters from an optimized ANN-BP model. . . . .	93
5.1	Chemical composition of AA3003-H18 material. . . . .	102
5.2	Design spaces of forming parameters and their levels. . . . .	103
5.3	CCF experimental design and experimental results of 30° cone angle	106
5.4	CCF experimental design and experimental results of 60° cone angle	107
5.5	Grey relational generation values. . . . .	109
5.6	Evaluation of deviation sequence. . . . .	109
5.7	Estimated values of grey relational coefficient. . . . .	110
5.8	Computed values of the grey relational grade (GRG) and rank. . . . .	110
5.9	Analysis of Variance (ANOVA) table for GRG values. . . . .	117
5.10	Main effects of considered parameters on mean GRG values. . . . .	118
5.11	Interaction effects of the selected parameters on mean GRG values. .	118
5.12	Analysis of Variance (ANOVA) table for GRG values. . . . .	120
6.1	Experimental Design from Taguchi L16 Orthogonal Array. . . . .	128
6.2	Main effects of process parameters (means and S/N ratio) for surface roughness . . . . .	130
6.3	Analysis of variance for means (surface roughness) . . . . .	130
6.4	Analysis of variance for S/N ratio (surface roughness) . . . . .	131

# List of Abbreviations

<b>ISF</b>	incremental sheet forming process
<b>SPIF</b>	single-point incremental forming process
<b>DIC</b>	digital image correlation
<b>SS</b>	stress ( $\sigma$ )–strain ( $\epsilon$ )
<b>SEM</b>	scanning electron microscopy
<b>FESEM</b>	field emission scanning electron microscopy
<b>EDS</b>	energy dispersive X-ray spectroscopy
<b>JC</b>	Johnson–Cook
<b>MJC</b>	modified Johnson–Cook
<b>MZA</b>	modified Zerilli–Armstrong
<b>AC</b>	Arrhenius-type constitutive
<b>ANN</b>	artificial neural network
<b>BP</b>	back-propagation
<b>FE</b>	finite element
$\epsilon$	strain (mm/mm)
$\dot{\epsilon}$	strain rate ( $s^{-1}$ )
$T$	deformation temperature ( $^{\circ}C$ )

$\sigma$	flow stress (MPa)
<b>ML</b>	Machine learning
$n$	number of samples
<b>HN</b>	number of neurons in hidden layer
<b>IN</b>	number of variables in input layer
<b>NO</b>	number of variables in output layer
<b>NT</b>	number of training data
$X_N$	normalized data
$X$	measurements from experiment
$X_{\min}$	minimum value of experimental data
$X_{\max}$	maximum value of experimental data
<b>TANSIG</b>	Tan-Sigmoid
<b>LOGSIG</b>	Log-Sigmoid
$R^2$	coefficient of determination
<b>RMSE</b>	root mean square error
<b>MSE</b>	mean square error
<b>AARE</b>	average absolute relative error
<b>OP</b>	optimization procedures
<b>fmincon</b>	find minimum of constrained nonlinear multivariable function
<b>IP</b>	interior-point
<b>GA</b>	genetic algorithm
<b>TOL</b>	Tolerance

$W_{ij}$	network weights
$b_i$	network biases
<b>IW</b>	weights in hidden layer
<b>LW</b>	weights in output layer
<b>b1</b>	biases in hidden layer
<b>b2</b>	biases in output layer
<b>trainbr</b>	Bayesian regularization
<b>trainlm</b>	Levenberg-Marquardt
<b>learngdm</b>	Gradient descent with momentum weight and bias learning function
<b>CNC</b>	computer numerical control
<b>HSS</b>	high-speed steel
<b>DOE</b>	design of experiments
<b>CCD</b>	central composite design
<b>CCF</b>	central composite face-centered
<b>RSM</b>	response surface methodology
<b>GRA</b>	grey relational analysis
<b>GRG</b>	grey relational grade
<b>ANOVA</b>	statistical analysis of variance

## Chapter 1

# Single Point Incremental Forming Process

## 1.1 Background

### 1.1.1 Cold Incremental Forming Process

Nowadays, manufacturing procedures need to be optimized to reduce the production cost and time without compromising the product quality. Existing conventional metal forming methods are designed to produce only predefined shapes; in the case of design alteration, the entire experimental setup has to be redesigned in terms of manufacturing tools. In mass production, this kind of preparation requires more production time, increasing the costs by manufacturing new parts such as dies, punches, and molds (Min et al., 2018). The incremental sheet forming process (ISF), called dieless forming, does not require any external die to produce the desired components as the new parts can be manufactured using the predefined contour tool path. The ISF process contributes a more beneficial material formability limit when compared to the conventional metal forming process. The ISF process includes tool path generation using the expected geometry CAD profile and a CNC machine's help to develop the final part. The base fixture and the blank holder are utilized to



clamp the blank sheet rigidly, and the forming tool goes past the sheet blank as per the numerical control program command lines to achieve the final component. This forming process uses the designed tool path to create a step-by-step deformation on the sheet metal part using the punch tool; a conceptual schematic diagram of the single-point incremental forming process (SPIF) process is illustrated in Figure 1.1.

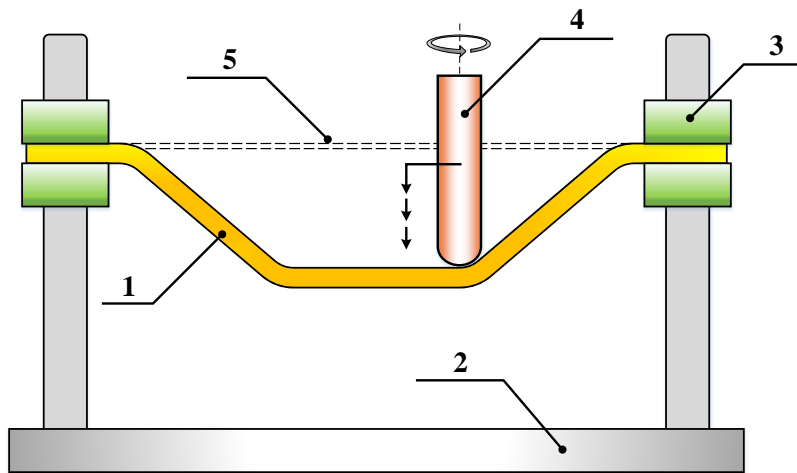


FIGURE 1.1: Single-point incremental forming process: 1-blank, 2-base support, 3-grip support, 4-forming tool, 5-blank initial position.

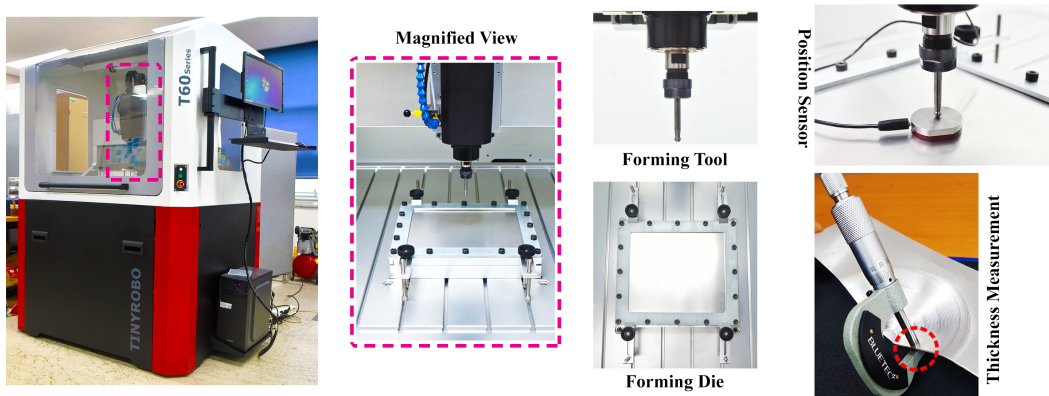


FIGURE 1.2: Experimental set-up of single-point incremental forming process.

This forming process, which involves no specific dies and punches, can be used to produce a wide range of shapes. The advantages include: highly economical for



FIGURE 1.3: Incrementally formed parts from SPIF process.

low volume production, increased material formability, less forming force, dieless, parts size limited by machine's working space, and better surface quality (Ajay, Boopathi, and Kavin, 2019). However, the dimensional accuracy of the manufactured product from the SPIF process mainly depends on the operating parameters: punch tool radius, vertical step size, spindle speed, feed rate, the design parameters: geometry shape, wall-angle, and thickness of the sheet blank. The SPIF process mainly employs three-axis CNC-controlled machines to produce the part. The SPIF experimental set-up used in this research work is outlined in Figure 1.2, and the incrementally formed parts using our forming machine are displayed in Figure 1.3.

Besides, the two-point incremental sheet forming (TPIF) is also called positive incremental sheet forming that needs either support or counter forming tools to form the metal sheet blank into the desired product. In this process, the parts are produced by introducing two different kinds of forming supports: contact between sheet blank and primary forming tool, and contact between supports or dies or counter forming tool and the sheet blank. The main reason behind the contact support improvements is to control the excessive, inappropriate material deformation during the forming process. The TPIF process is explained in Figs. 1.4, 1.5, and 1.6. Figure 1.4 shows that the forming process involves partial die support, whereas the specific die support is used in Figure 1.5. Similarly, the counter forming tool support is used to control the excessive material deformation, as shown in Figure 1.6. Advantages of the TPIF

process over the SPIF process: parts accuracy in terms of shape and dimensions, higher wall-angle achievement, can control the redundant thinning behavior.

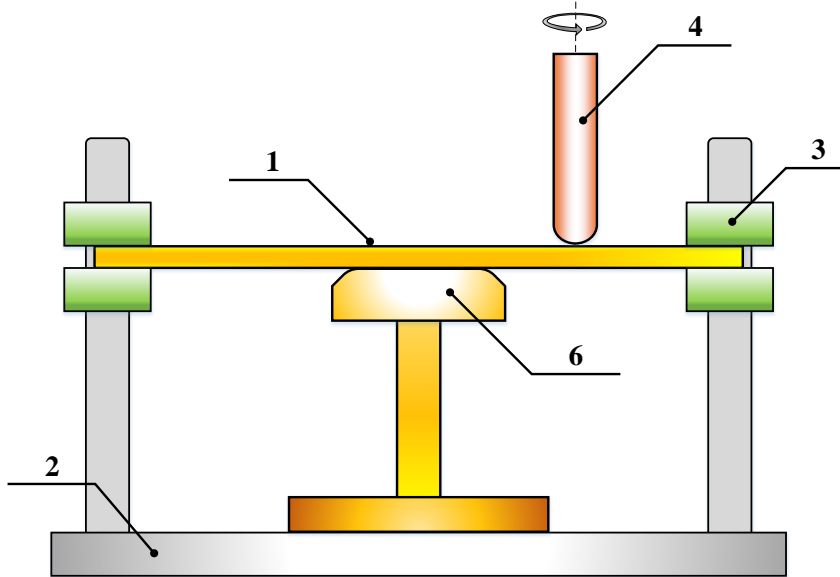


FIGURE 1.4: Two-point incremental forming process with partial die support: 6–partial die.

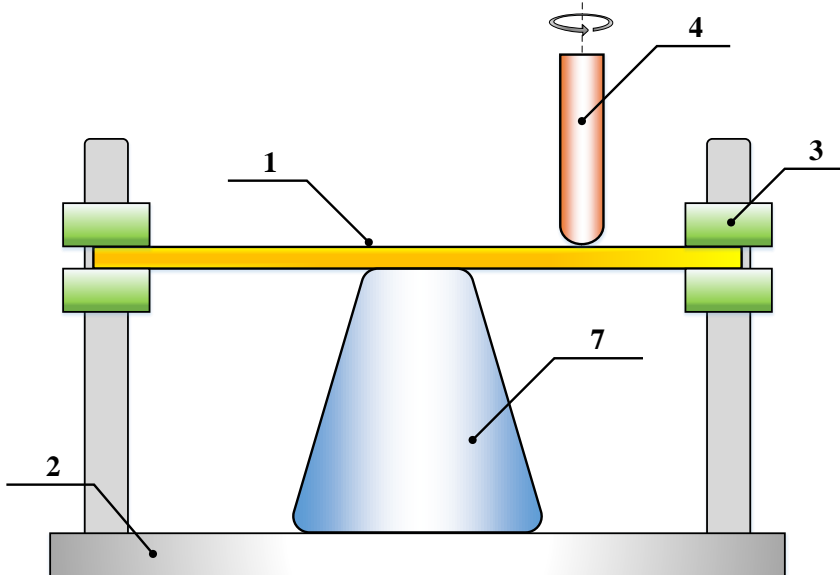


FIGURE 1.5: Two-point incremental forming process with specific die support: 7–specific die.

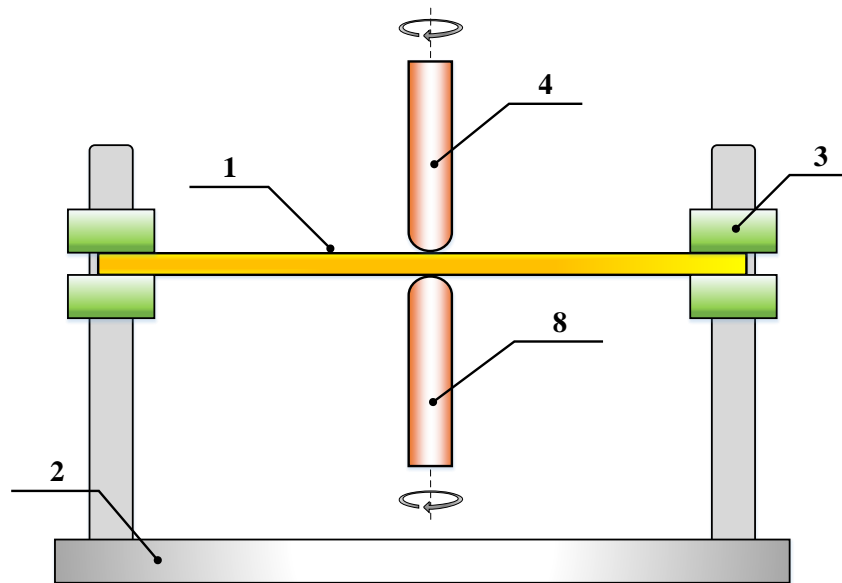


FIGURE 1.6: Two-point incremental forming process with counter tool support: 8-forming tool.

Furthermore, there are many other factors that impact the material formability in terms of the parts accuracy: mechanical properties (elastic-plastic properties), material plastic anisotropy, lubrication selection, and tool-path strategies. (Ren et al., 2019; Wei et al., 2019; Maqbool and Bambach, 2018; Chang and Chen, 2020; Fiorentino, Giardini, and Ceretti, 2015; Said et al., 2016). Besides, the forming force also has a significant impact in the ISF process because excessive forming force can tear the sheet material due to thinning behavior, and the moderate forming force cannot deform the sheet metal to the desired shape (Bansal et al., 2017; Chang, Li, and Chen, 2019; Saidi et al., 2015). So, choosing the proper forming punch tool is critical for preventing fractures and producing flawless parts (Ai et al., 2017; Davarpanah et al., 2015; Raju, Haloi, and Narayanan, 2017). Even though numerous research works have been completed, the SPIF process is still being developed to produce better components with good surface quality and formability (Murugesan, Sajjad, and Jung, 2019b; Murugesan, Sajjad, and Jung, 2020b; Murugesan, Sajjad,

and Jung, 2020a).

### 1.1.2 Hot Incremental Forming Process

The high-strength materials are challenging to form at room temperatures using the conventional ISF process because of their poor material ductility behavior. Therefore, the heat-assisted ISF methods have been proposed by several researchers for improving the material formability of such materials and minimize the geometrical accuracy problems (Ajay, Boopathi, and Kavin, 2019; Honarpisheh, Abdolhoseini, and Amini, 2015; Liu, 2018; Vahdani et al., 2019; Lee and Yang, 2020; Ortiz et al., 2014), as shown in Figure 1.7. For enhancing the material formability, surface quality, and geometric accuracy, the forming process for high-strength aluminum and magnesium alloys uses a direct current source onto the sheet blank, and homogeneous heating is achieved quickly. Sy et al. (Sy and Nam, 2013) stated that the accuracy and formability were improved and eliminated the spring-back. Besides, the forming parameters, such as depth step and feed-rate, were sensitive to AZ31 material deformation because of micro-structure transformations at high temperatures.

Similarly, Manel Sbayti et al. (Sbayti et al., 2016) investigated the titanium alloy Ti-6Al-4V material for medical applications using the hot ISF process to increase material formability. They adopted the finite element (FE) simulations using the Johnson-Cook (JC) constitutive and failure models for modeling the hot ISF process. They concluded that the geometry accuracy was enhanced, and the forming parameters such as forming temperature and forming tool diameter showed a positive impact on the accuracy of the parts. Likewise, Guoqiang Fan et al. (Fan et al., 2008) examined the hot forming process for titanium and magnesium alloys using electric current to form the high-strength metal sheets by producing heat onto the sheets. They declared that forming parameters, namely, current, step-size, feed-rate, punch tool radius, and resistivity, were influenced the material formability. In contrast,

the temperature was noticed to be decreased when the process parameters such as feed-rate, tool radius, and step size increased. Amar Al-Obaidi et al. (Al-Obaidi, Kräusel, and Landgrebe, 2015) also used the same processing technique but with the induction heating process to improve the material formability for high-strength steels. They found that the local heating provides smooth forming and formability enhanced as the residual stress, the spring back, and the forming forces reduced in the formed parts.

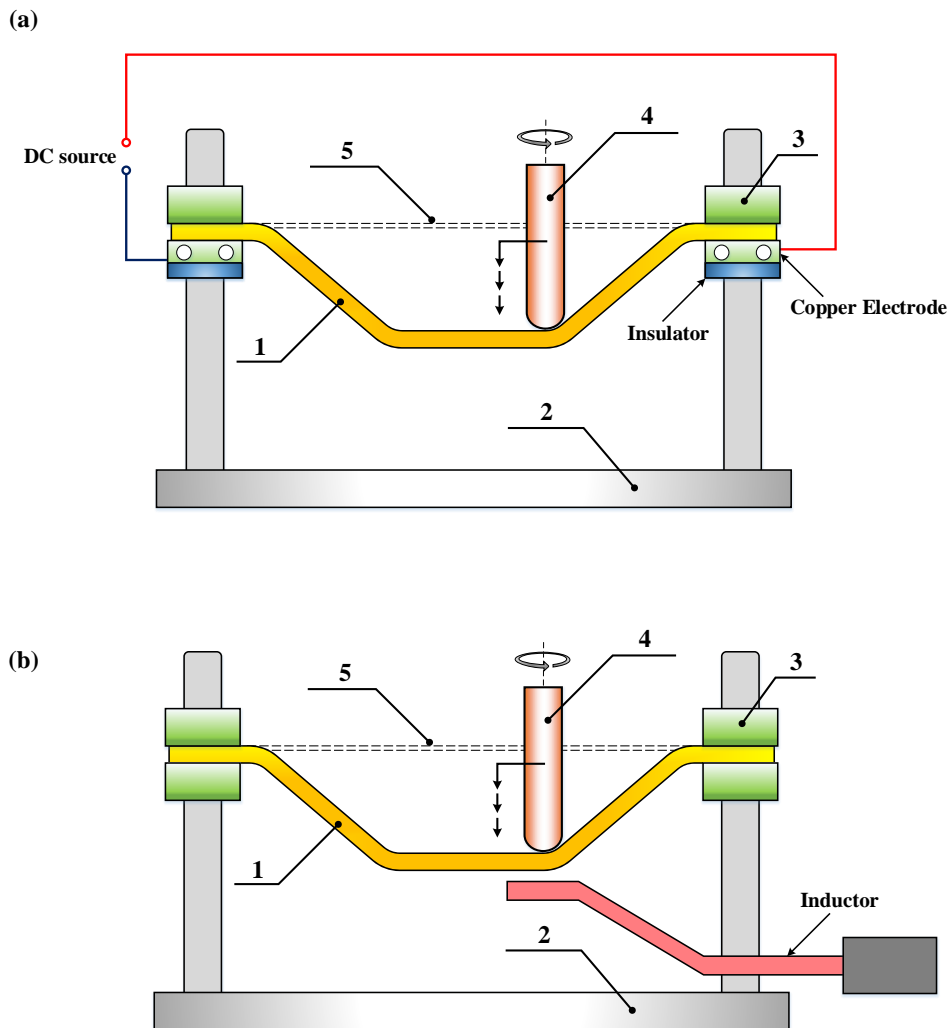


FIGURE 1.7: Hot incremental forming process. (a) Electric current; (b) Induction heating.

## 1.2 Organization of the Dissertation

This thesis is arranged in 7 distinct chapters as a summary of published research articles (Murugesan, Sajjad, and Jung, 2021b; Sajjad, Murugesan, and Jung, 2020; Murugesan and Jung, 2019a; Murugesan and Jung, 2019b; Murugesan, Sajjad, and Jung, 2020c; Murugesan, Sajjad, and Jung, 2019a; Murugesan and Jung, 2021; Murugesan, Sajjad, and Jung, 2019b; Murugesan, Sajjad, and Jung, 2020b; Murugesan, Sajjad, and Jung, 2020a).

- Chapter 1 introduces the concise introduction of the incremental forming process (ISF) and reveals the process parameters that influence material formability and the potential applications. Afterward, it includes extensive information about the lubrication selection and the material characterization, such as material test, material properties estimation, plastic anisotropy calculation, and microstructure investigation of tested samples from uniaxial tensile tests at both room and high temperatures.
- Chapter 2 includes the Johnson-Cook model construction for the material deformation behavior prediction using AISI-1045 medium carbon steel flow stress data. Besides, the detailed fracture model development is added that can be used for a wide range of metal forming applications.
- Chapter 3 presents a comparative study of modified Johnson-Cook (MJC) and modified Zerilli-Armstrong (MZA) models. Here, the well-constructed empirical model development is explained and discussed both advantages and drawbacks of the proposed models.
- Chapter 4 deeply researches the importance of strain compensation and modifying the Zener-Holloman parameter on the Arrhenius-type constitutive

equation construction. In addition, this chapter includes the artificial neural network model development combined with the optimization procedures to capture the material plastic instability phenomenon, which occurs during the hot uniaxial tensile tests. Thus, the advantages of the ANN-BP model over other available traditional flow stress models are discussed in detail.

- Chapter 5 studies the influence of the forming parameters such as forming tool radius, vertical step size, and feed rate on the material formability considering five responses using the design of experiments (DOE), the response surface methodology (RSM) coupled with the grey relational analysis (GRA), and analysis of variance (ANOVA) approach.
- Chapter 6 gives comprehensive information about the Taguchi method procedure for obtaining mathematical model to achieve better surface quality by minimizing the surface roughness. Lastly, a discussion about the microstructure examination on both fractured and unfractured formed parts from the single point incremental forming (SPIF) process.
- Chapter 7 includes overall thesis conclusions and possible future research works. It is anticipated that the present research work provides better knowledge about the necessity of material properties estimation and the SPIF manufacturing process.

### 1.3 Toolpath Strategies

The ISF process is based on the concept of step-by-step incremental deformation, and as a result, a blank is formed into an expected shape using a CNC machine along with the smooth end forming tool, which follows the specific toolpath. The forming toolpath generation is crucial as it is directly linked to part accuracy in terms of



shape and dimensions, as illustrated in Figure 1.8. Besides, it also affects surface finish, material forming limit, machining time, and thinning behavior (Rauch et al., 2009; Ambrogio et al., 2004). The tool path design strategies have been proven to significantly affect the forming process and alter the material formability, resulting in loss of achievable part accuracy. So, choosing the proper optimal tool path and its sequences is vital for ensuring higher part accuracy.

Amar et al. examined the problem mentioned above (Behera et al., 2013; Behera, Lauwers, and Duflou, 2014). They (Behera et al., 2013) proposed an error prediction tool for generating an error response surface to continuously monitor the geometry deviations using the multivariate adaptive regression splines method. From the outcome, they found that the accuracy of the manufactured part improved significantly in terms of average absolute deviation when the developed response surfaces were combined with a rib offset strategy. In addition, the same authors (Behera, Lauwers, and Duflou, 2014) proposed a network analysis methodology to obtain various aspects that affect the final geometry accuracy using conceptual graphs and then the optimized contour paths achieved from the modeled framework. They concluded that the deviations were reduced adequately in the complete formed part. Ebot et al. (Memicoglu, Music, and Karadogan, 2017) investigated the multi-pass single-point incremental forming process (MSPIF) process using an intermediate geometries tool-path strategy to improve the material formability. They provided the information for calculating the rigid body motion of the forming tool along the tool path. They concluded that using the proposed methodology, an MSPIF approach, improves material formability. Zhaobing Liu (Liu, Li, and Meehan, 2014) aimed to develop suitable tool path strategies for multi-pass deformation design. They concluded that deformation passes and tool path strategies impact the thickness strain distribution and material formability. Therefore, they suggested that a proper toolpath has to be designed to reduce the material thinning and improve the process

formability considering the geometrical characteristics.

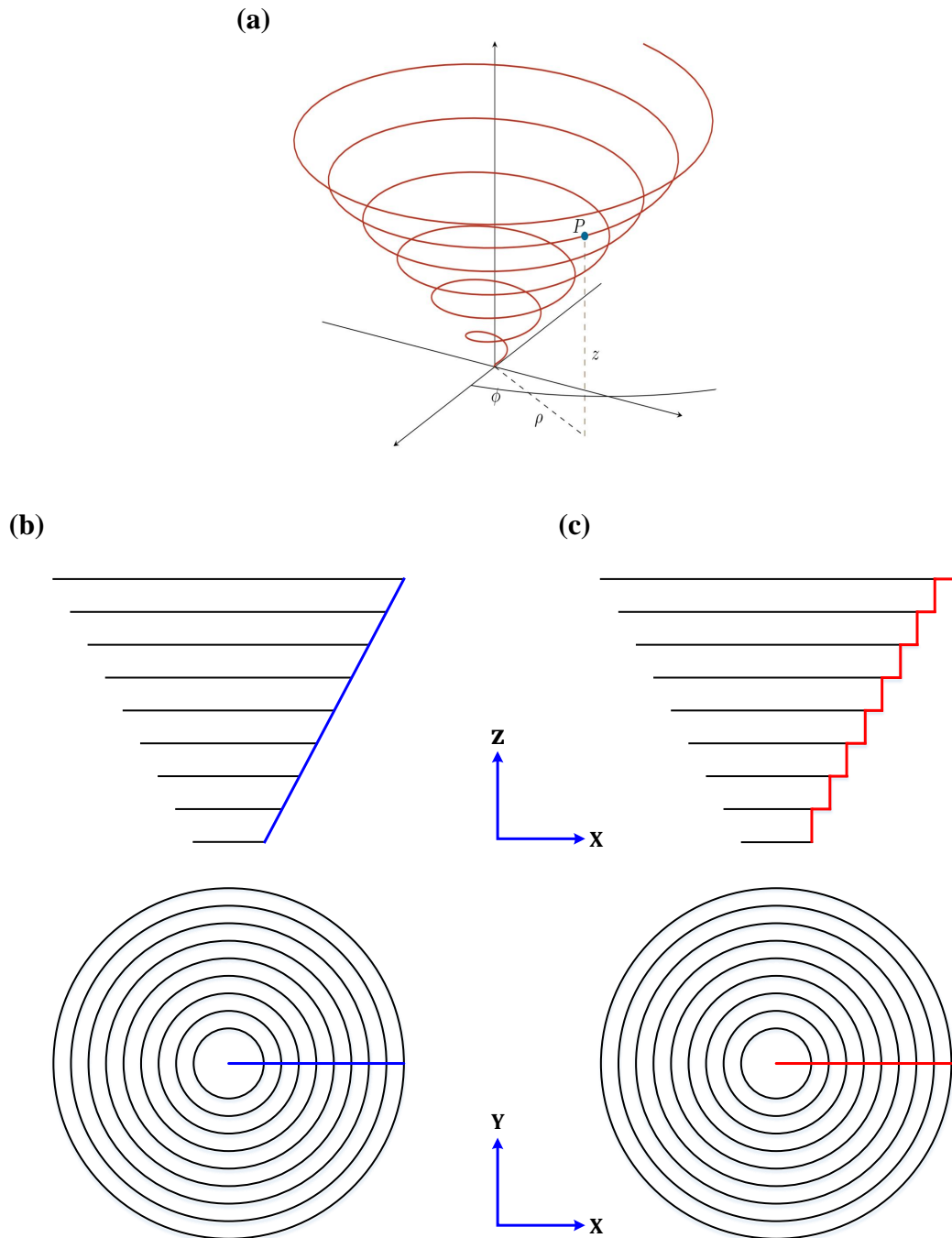


FIGURE 1.8: Tool-path options. (a) Spiral; (b) Contoured; (c) Stepped.

## 1.4 Surface Quality

Surface quality investigation of a material's surface is conducted by roughness analysis of the tested sample's surface. Numerous procedures have been manifested to accomplish this objective, including geometrical analysis and surface roughness analysis, as illustrated in Figure 1.9. The geometric analysis provides a visual and subjective examination of roughness (a qualitative assessment). In contrast, the roughness parameter computation is a quantitative evaluation and provides a regulated interpretation of the surfaces (Tonietto et al., 2019). Kumar et al. (Kumar and Gulati, 2019) investigated the influence of process parameters on the surface quality of the formed parts. For obtaining the optimum level of forming parameters, the Taguchi method was chosen with the help of the design of experiments and statistical analysis of variance (ANOVA). The tool diameter was found to influence the surface roughness, whereas the tool shape and the lubricant also produced significant influence in terms of the surface roughness. The proposed prediction model results showed better agreement with the confirming experiments for the optimized parameters.

Chang et al. (Chang and Chen, 2019) investigated the ISF process by considering the irregular thickness distribution induced by elastic deflection and plastic deformation. A detailed study on the surface roughness development was conducted to understand the forming mechanism; from this experience, analytical models to predict roughness were constructed. The proposed model was tested by adopting a conical shape against different materials, and the surface morphologies were analyzed. Jawale et al. (Jawale et al., 2018) conducted similar research to investigate the reasons behind the surface roughness improvement. A polycrystalline copper sheet with a truncated conical shape and various lubricants was considered, and tests were conducted until fracture. The formed parts were investigated from the microstructural point of view; the authors observed a significant lubrication influence

on the surface. The forming tool marks and the grain boundaries were identified as the reason for surface roughness increase.

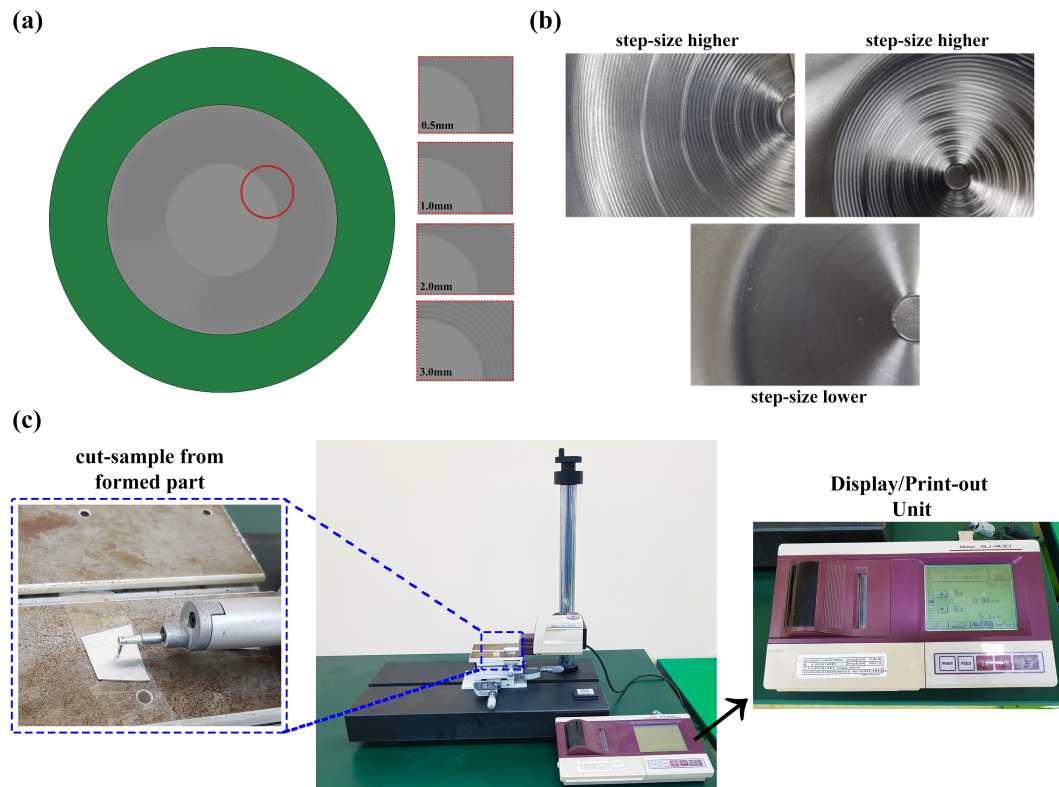


FIGURE 1.9: Surface quality evaluation.

## 1.5 Applications

Incremental sheet forming (ISF) is a dieless manufacturing process that has a wide range of applications in the following areas: Biomedical Implant, Automobile, Aerospace, Nuclear Reactors, and Defense. Due to its advantage of having no specific die requirement, it can be adopted to produce any complex parts within a day, even within an alteration of shape and size. That is why this method is listed as a rapid prototyping manufacturing process. In contrast, this is not included in mass production because of its time consuming but uniquely suitable for small

batch production. For example, the human body parts are complex and troublesome to make. However, using the ISF process, it can be formed just by using various toolpath generation, and no need of external die design, as shown in Figure 1.10.

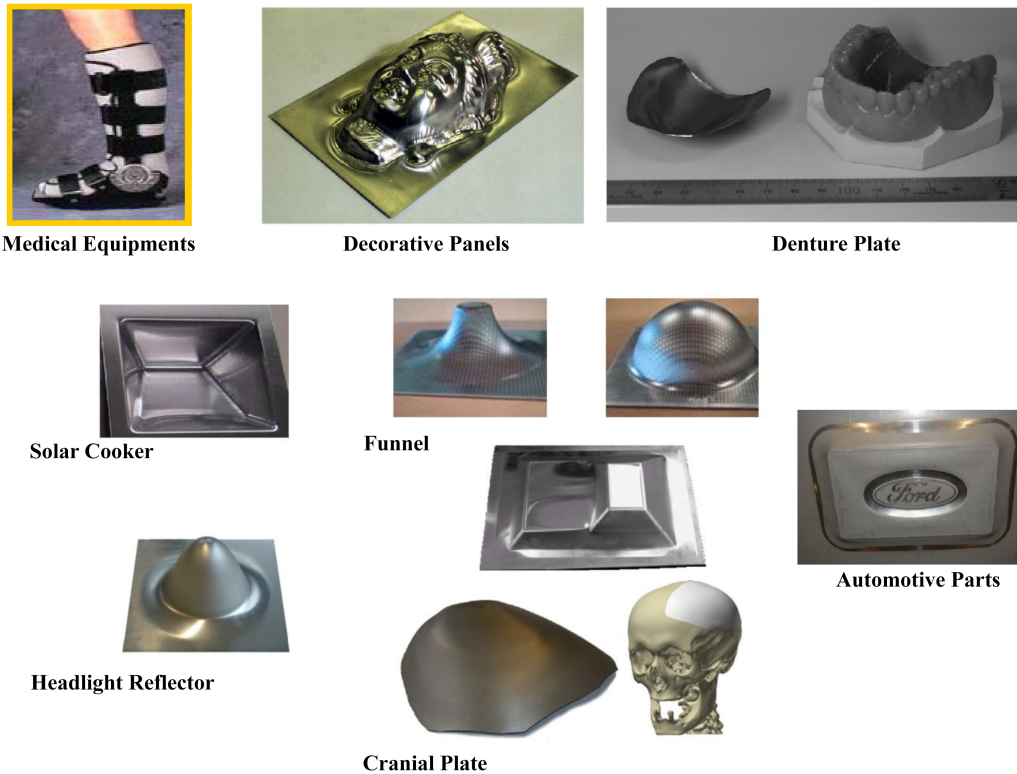


FIGURE 1.10: Real-time applications of incremental forming process.

## 1.6 Effects of Process Parameters

The process parameters such as forming tool radius, vertical step-size, feed-rate, forming tool spindle speed, sheet thickness have to be reviewed and optimized for improving the material formability, namely accuracy of the parts, accurate forming angle, lesser thickness reduction, higher forming depth. Maqbool et al. (Maqbool and Bambach, 2019) analyzed the relationship between dimensional accuracy and residual stresses considering various process parameters like tool diameter, tool

step-down, and wall angle. From the detailed investigation, the wall angle was found to be the most significant working parameter, and the effects occurred mostly in the transverse direction of the punch tool movement. Saidi et al. (Saidi et al., 2017) investigated the process considering two materials, titanium grade 2 and AISI 304L stainless steel, to obtain the optimum forming force to ensure that both parts and the machine are adequately controlled to eliminate the failures. Three parameters (maximum tensile strength, tool diameter, and tool displacement) were adopted to develop a mathematical model for minimizing the forming force. For that purpose, a response surface methodology (RSM), along with the Taguchi method, was used. They concluded that the considered forming parameters significantly influenced the formed parts. Baruah et al. (Baruah, Pandivelan, and Jeevanantham, 2017) aimed to improve formability and minimize surface roughness in the ISF process. The grey relational analysis (GRA) procedures considering Taguchi's method were adopted, and surface roughness measurement from three directions—rolling, transverse, and angular—was used as the response variable. They reported that the formability contribution was mainly based on the lubrication, and conversely, the feed rate had the least contribution.

## 1.7 Process Modeling and Simulation

In the SPIF process, understanding deformation and fracture mechanisms plays a significant role in enhancing the formability of the formed products, as shown in Figs. 1.11 to 1.14; detailed investigations have been conducted by Said et al. (Said et al., 2017), Mohammad et al. (Mirnia and Shamsari, 2017), and Shakir Gatea et al. (Gatea et al., 2017). Ben et al. (Said et al., 2017) examined the damage mechanism in the SPIF process using numerical simulations considering the conical geometry. The user subroutine was developed, including two damage models: an elastoplastic model

with quadratic yield criteria of Hill'48 and the mixed isotropic/kinematic hardening behavior for modeling the process. They found that a mixed formulation, including isotropic-kinematic hardening, more accurately captured the damage evolution. The phenomenological modified Mohr–Coulomb (MMC3) model was implemented into the user subroutine material card for the commercial numerical code to examine the ductile damage in SPIF by Mirnia et al. (Mirnia and Shamsari, 2017). Using an inverse approach, the MMC3 criterion was evaluated using the devised tensile tests for AA6061-T6 aluminum alloy sheet, and localized deformations were examined in detail. They reported that a deviation of 10% was recorded with the experimental measurements, and the prediction of fracture locations agreed well with the real observations. A modified Gurson–Tvergaard–Needleman (GTN) damage model considering shear proposed by Gatea et al. (Gatea et al., 2017) showed a better ductile damage prediction in the SPIF process compared to the original GTN model under shear loading conditions. They mentioned that in the forming process, the damage propagation tends to be accelerated because of the shear under meridional tensile stress. Memicoglu et al. (Gambirasio and Rizzi, 2016) researched the importance of numerical modeling in the flexible forming process, as the forming process mechanism has not been completely studied. They developed fast simulation models by reducing the computational time up to 24 times for the SPIF process, and the maximum model shape error was around 8%. They stated that the presented approach could be adopted to model the forming process with reasonable computational time.

## 1.8 Selection of Lubrication

To quantitatively evaluate the effect of lubricant performance on the surface quality assessment, the prepared sample was investigated using three different lubricants: oil, grease, and a combination of oil and grease, as displayed in Figure 1.15a.



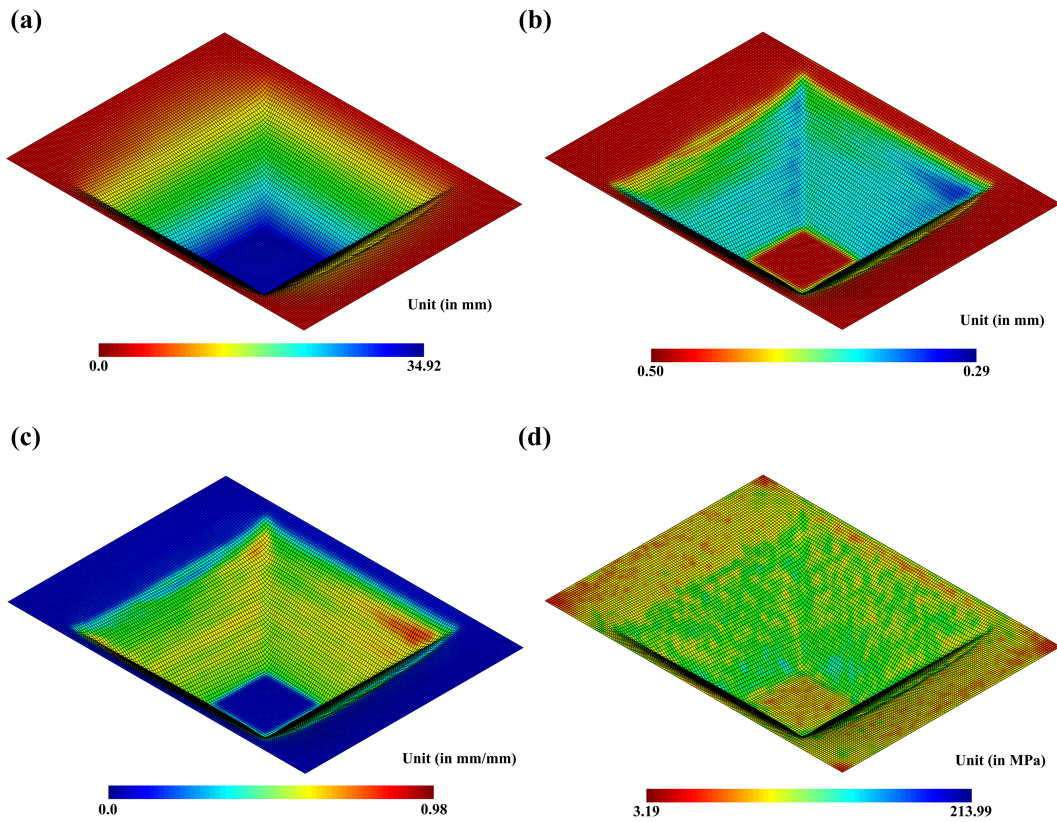


FIGURE 1.11: Contour plots of 45° pyramid geometry: (a) Forming depth; (b) Thinning behavior; (c) Strain; (d) Stress.

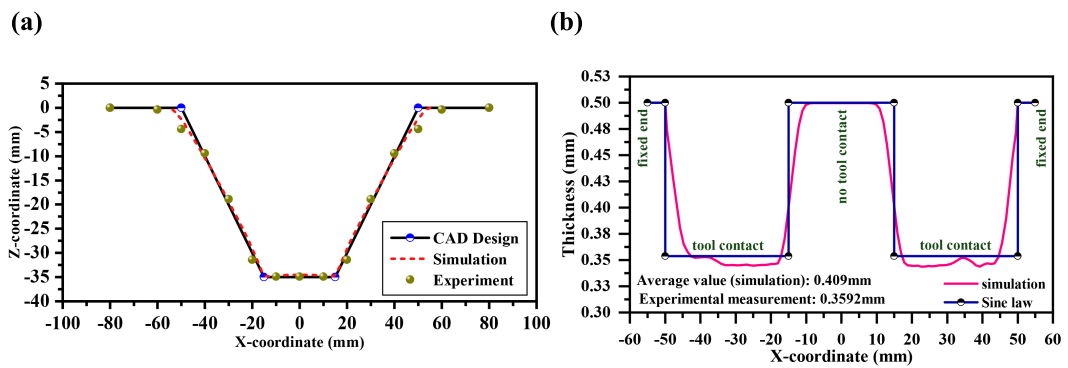


FIGURE 1.12: (a) Profile comparison of formed pyramid shape against real experiment and expected geometry (45°); (b) Thickness measurement (Murugesan, Sajjad, and Jung, 2020b).



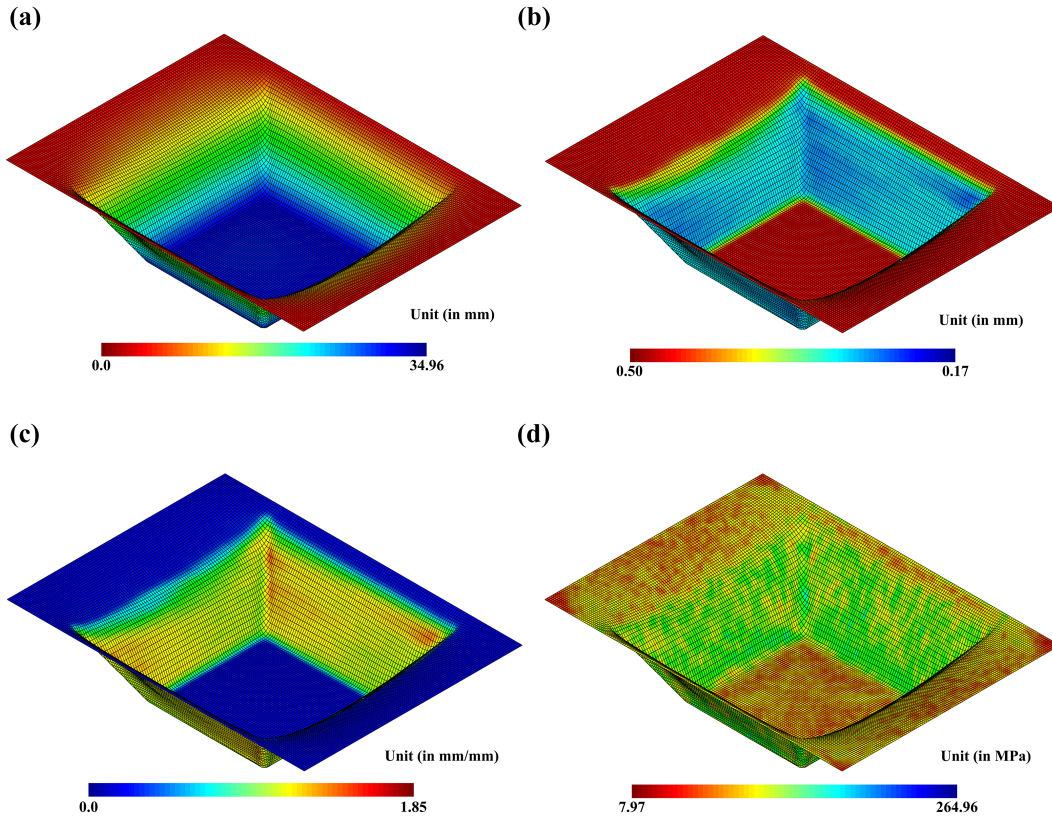


FIGURE 1.13: Contour plots of 60° pyramid geometry: (a) Forming depth; (b) Thinning behavior; (c) Strain; (d) Stress.

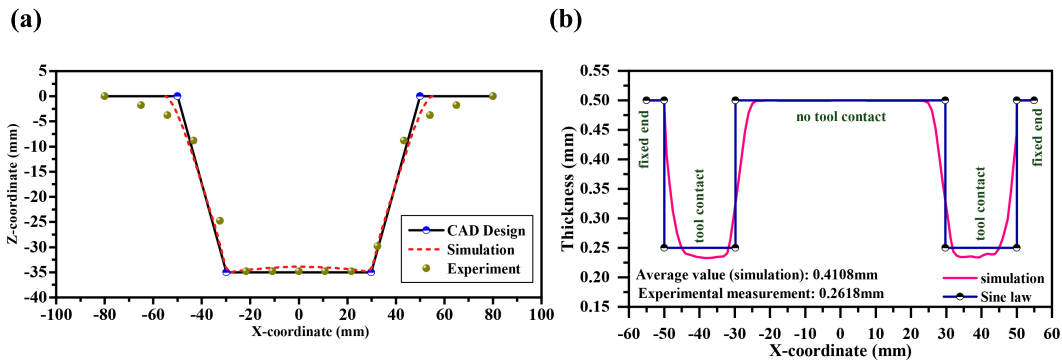


FIGURE 1.14: (a) Profile comparison of formed pyramid shape against real experiment and expected geometry (60°); (b) Thickness measurement (Murugesan, Sajjad, and Jung, 2020b).

The forming conditions were modeled to be the same for all tested cases to facilitate comparison for choosing the best lubricant. Using 3D nano surface profiler equipment (Jeju National University, Jeju-si, South Korea), the roughness was measured as 0.56, 0.80, 0.66, and 0.64  $\mu\text{m}$  for the original surface, oil lubricant, grease lubricant, and oil–grease lubricant, respectively. From the outcome, the lubricant combining oil and grease was found to be the best option. The scanned 2D surface roughness profile of the samples is illustrated in Figure 1.16a–d (Murugesan and Jung, 2021).

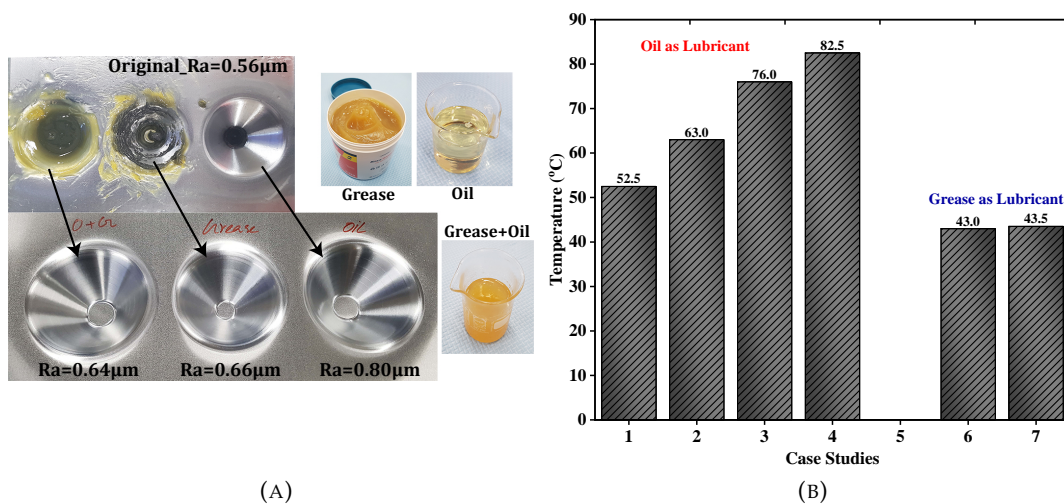


FIGURE 1.15: (a) Lubricants used; (b) Temperature comparison plot.

The contact during the forming process between the blank and the generally shaped forming tool is quick, transient, and temporary, which poses challenges for measuring the temperature changes in the test sample on the exact contact-forming area. However, in this research, the temperature changes were monitored and recorded from the lubricant using a manually controlled thermometer at a specified machining time to provide the results of heat transfer from the work piece and the forming tool to the lubricant during the forming process. Figure 1.15b shows that the oil lubricant tended to produce higher temperature changes than the grease lubricant because of its semisolid state and viscosity. As viscosity mainly depends

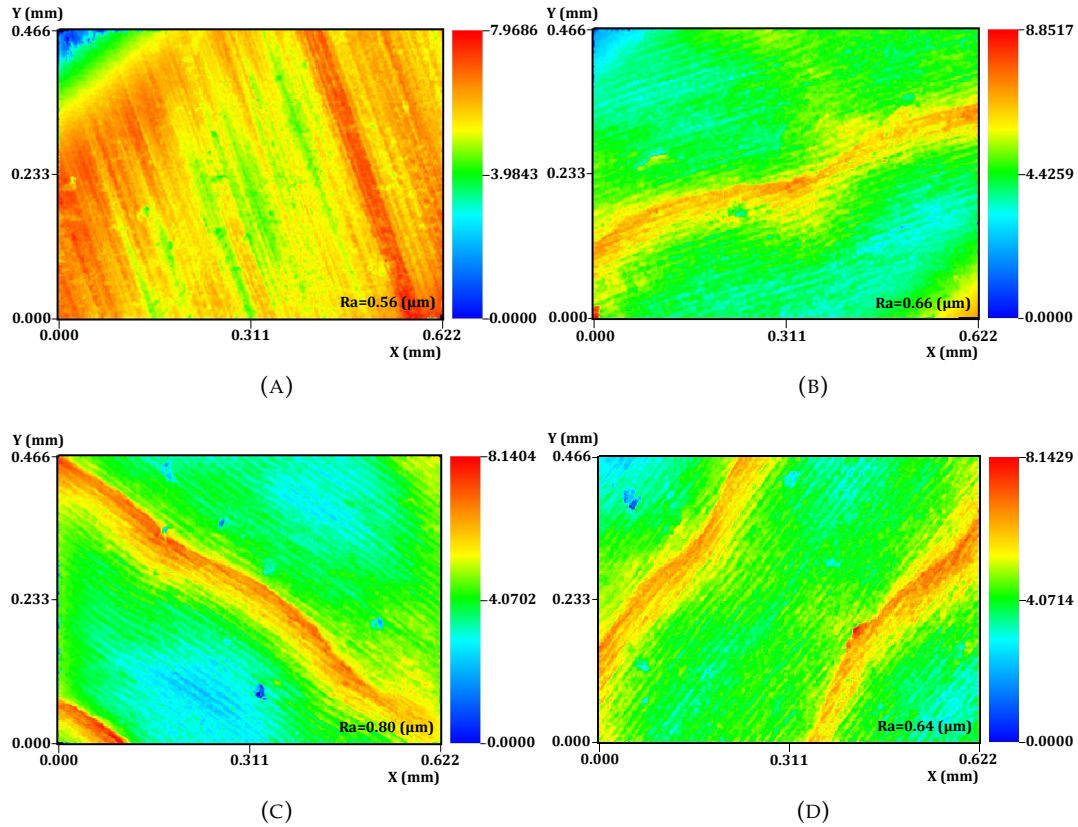


FIGURE 1.16: 2D surface roughness profile of the formed material using different lubricants from the 3D nano profiler: (a) Original surface; (b) Grease; (c) Oil; (d) Combination of oil and grease.

on the temperature, the heat transfer among the grease lubricant and the test piece caused the viscosity of the grease to lower, increasing its temperature to a certain point, as shown in Figure 1.15a (grease turned black). The temperature of oil–grease lubricant did not change during the forming process, and the lubricant had a lower roughness, which was more favorable for producing a better surface quality on the formed parts compared to the other lubricants (Murugesan and Jung, 2021; Murugesan and Jung, 2019a; Murugesan and Jung, 2019b; Murugesan, Sajjad, and Jung, 2021b; Murugesan, Sajjad, and Jung, 2020c).

## 1.9 Material Characterization

For extracting the material mechanical properties and the anisotropy coefficients required for the finite element simulations, several uniaxial experimental tests are carried out to characterize the mechanical behavior of the selected materials, such as aluminum sheet alloys (AA3003-H18 and AA5052-H32) and magnesium alloy (AZ31B). Similarly, to describe the mechanical behavior of any material, the flow stress models are proposed using AISI 1045 steel material by performing the uniaxial tensile tests at elevated temperatures. The reason behind the material selection is that it is widely used in the metal forming industry for many aerospace and automobile applications due to its impeccable material properties like good weldability, machinability, and high strength and impact properties. The framework presented in this dissertation can be adopted to develop constitutive models for any new material. The parameters of interest to be estimated (Murugesan, Sajjad, and Jung, 2021b; Murugesan, Sajjad, and Jung, 2021a):

- Material properties: at  $0^\circ$ ,  $45^\circ$  and  $90^\circ$  to the rolling direction
- Anisotropy parameters: at  $0^\circ$ ,  $45^\circ$  and  $90^\circ$  to the rolling direction
- Constitutive models for performing the hot forming process.

### 1.9.1 Material Test

The sheet material studied in this research work is an aluminum alloy (AA5052-H32) for the cold roll forming application. The material sheet was received with three thicknesses of 0.8 mm, 1.0 mm, and 1.5 mm, respectively. The chemical compositions of the sheet material in wt % are as follows: 0.25% Si, 0.10% Mn, 2.2–2.8% Mg, 0.10% Cu, 0.15–0.35% Cr, 0.40% Fe, 0.10% Zn, and remaining % Al. Scanning electron microscope (SEM), MIRA3 TESCAN (Secondary electron detector, Jeju National University, Jeju-si, Korea), equipped with energy-dispersive X-ray spectroscopy (EDS),



for surface analysis was employed. Figure 1.17 depicts the FESEM analysis data of AA5052-H32 Al alloy material. The test specimen micro-structure observations before and after deformation (at the fractured surface) are depicted in Figure 1.17a,b. Moreover, the fracture region magnified scanning electron microscope (SEM) image shows a high proportion of waviness/stretching at a scale of 50  $\mu\text{m}$ , exposing a ductile fracture criterion, as shown in Figure 1.17b. The tensile specimen's localized necking zone in terms of orientation was estimated to be  $\approx 25^\circ$ ,  $\approx 24^\circ$ , and  $\approx 25^\circ$  for the test samples at  $0^\circ$ ,  $45^\circ$ , and  $90^\circ$  to the rolling directions as illustrated in Figure 1.17c. The test sample's elemental analysis is carried out using the FESEM-EDS method combined with an element mapping, where an image is exhibiting the spatial dispersion of elements, as shown in Figure 1.18a,b. From the element spectrum results comparison, Figure 1.18a, the alloy element's presence was observed to be nearly the same as the chemical composition mentioned earlier from the material database (Murugesan, Sajjad, and Jung, 2021b).

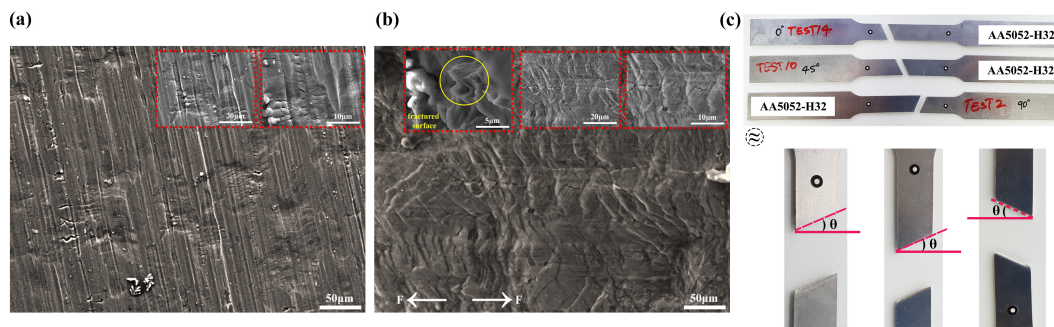


FIGURE 1.17: Field emission scanning electron microscopy (FESEM) analysis (a) Microstructure observation at initial state; (b) Microstructure observation after fracture; (c) Tested samples.

## 1.9.2 Uniaxial Tensile Test

Room temperature tensile tests were carried out using the test samples prepared from the blank sheet (AA5052-H32), considering three angles, such as  $0^\circ$ ,  $45^\circ$ ,

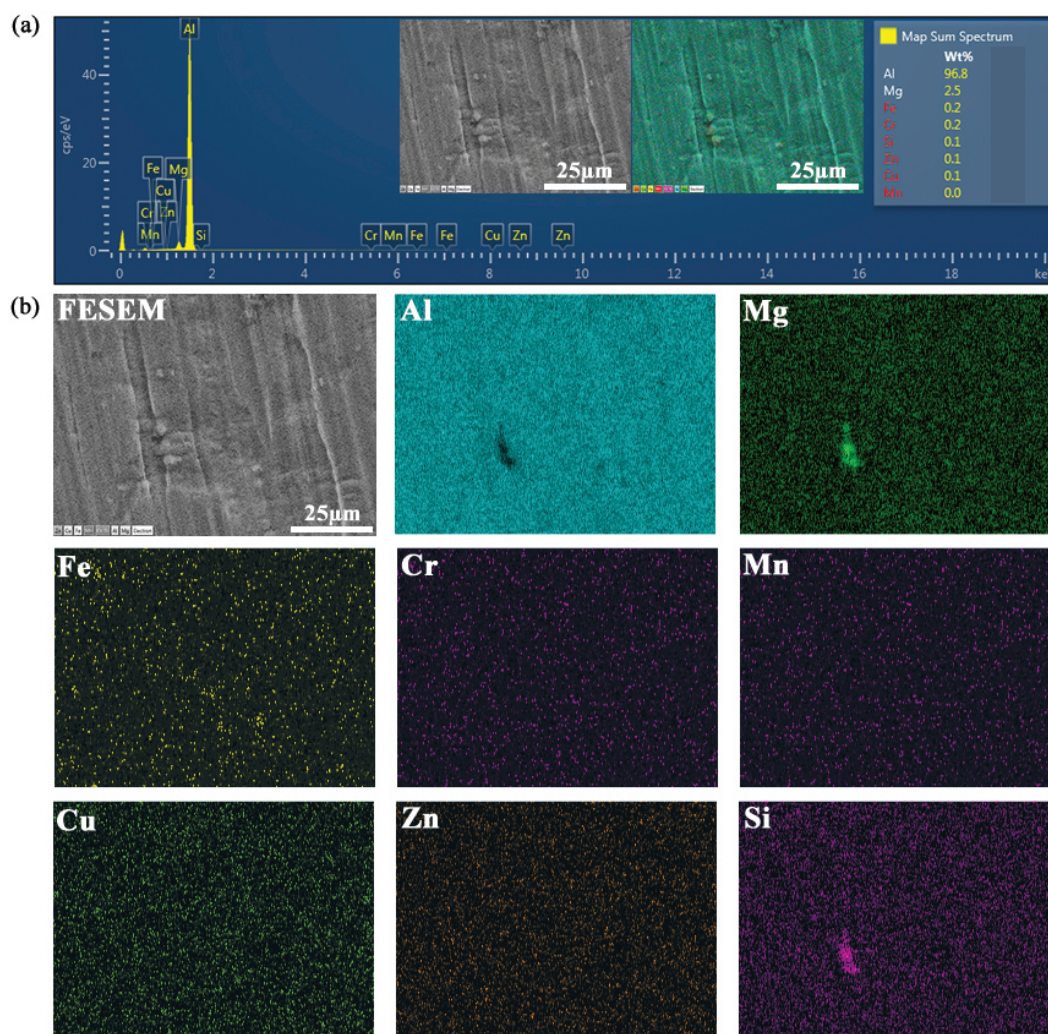


FIGURE 1.18: Energy dispersive X-ray spectroscopy (EDS) analysis (a) Element spectrum corresponding to AA5052-H32 material; (b) EDS elemental mapping images showing the distribution of chemical elements.

and  $90^\circ$ , to the rolling direction, respectively. The rectangle samples were cut down using the laser cutting machine based on ASTM-E8 standard with a gauge length of 50 mm, a thickness of 1.0 mm, and a sample gauge area of  $50 \times 12.5 \text{ mm}^2$ , respectively. The experiment was performed employing an TSM-100 machine with a maximum load capacity of 99.64 kN, and the test samples were tested at room temperature with a strain rate of  $0.001 \text{ s}^{-1}$ , as shown in Figure 1.19a.

The standard GOM–ARAMIS technique was adopted for investigating the local deformations in the samples using the recorded digital images during the tensile test till the rupture (Lee et al., 2015; Zhuang et al., 2012; Aydin and Oz, 2018). The major strain in terms of technical strain (%) in the test sample was measured using the digital image correlation (DIC) system (Aramis) just before and after the rupture, as illustrated in Figure 1.19c. The average major strain extraction from the test sample along the longitudinal axis up to fracture was compared against the strain estimated based on the gauge length before and after the test to ensure that the calculation was done correctly. For this purpose, a perpendicular line of roughly 50 mm considering the gauge length was marked along the undeformed sample's longitudinal axis.

For the gauge length based computation, standard tensile test procedures were used as follows:

$$\sigma_e = \frac{F}{A_0}, \quad \varepsilon_e = \frac{\delta L}{L_0} \quad (1.1)$$

$$\sigma_t = \sigma_e(1 + \varepsilon_e), \quad \varepsilon_t = \ln(1 + \varepsilon_e). \quad (1.2)$$

where as  $\sigma_e$ ,  $\varepsilon_e$ ,  $\sigma_t$  and  $\varepsilon_t$  are the engineering stress, the engineering strain, the true stress, and the true strain, respectively (Lee et al., 2015; Zhuang et al., 2012; Aydin and Oz, 2018; Chen et al., 2019; Tomáš et al., 2019; Hedayati, Madoliat, and Hashemi, 2017; Kirbach et al., 2015; Ashrafi and Tuttle, 2016; Wang et al., 2010; Murugesan and Jung, 2019b). In Equation (1.1),  $F$ ,  $A_0$ ,  $\delta L$ ,  $L_0$  are the load applied, the initial area of sample cross-section, the length change and the gauge length, respectively.

Similarly, the material properties of aluminum alloy (AA3003-H18) and magnesium alloy (AZ31B) are estimated using the procedures mentioned above. The obtained mechanical properties of aluminum sheet alloys (AA3003-H18 and AA5052-H32) and magnesium alloy (AZ31B) are summarized in Table 1.2, Table 1.3, and Table 1.4.

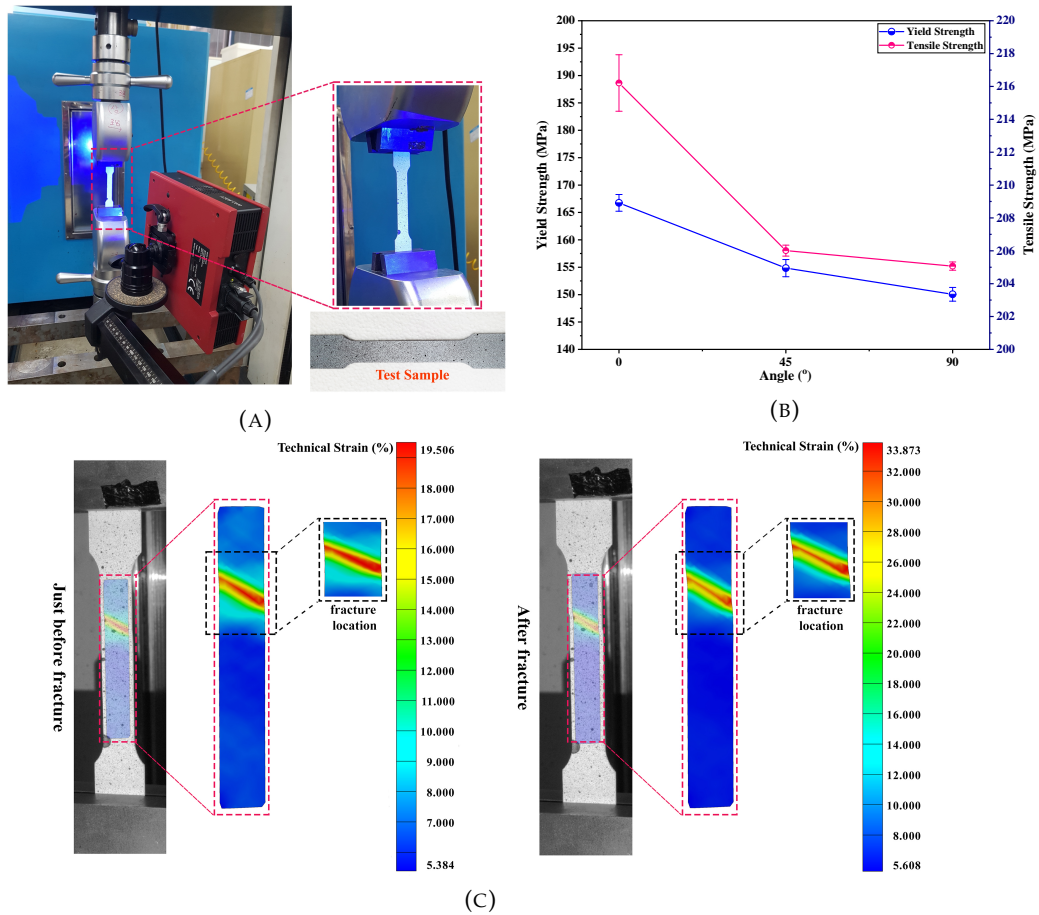


FIGURE 1.19: (a) Experimental setup used for the uniaxial tension test with Aramis; (b) Yield and tensile strength data at 0°, 45° and 90° to the RD; (c) Major strain measurements by Digital Image Correlation (DIC) just before and after fracture.

### 1.9.3 Measurements of Strain-hardening Models

Theoretical equations, such as Hollomon power-law and Ramberg-Osgood, are used to model the relationship between stress and strain of the tested material. In detail, the Ramberg-Osgood equation predicts and describes the relationship between stress and strain of the material near its yield point, whereas the power-law explains the material flow behavior in the plastic region (Murugesan, Sajjad, and Jung, 2021a). The true SS curves were approximated for modeling the material plastic behavior



in the numerical model. The Hollomon power-law equation was used for curve approximation, as shown in Equation (1.3). The model coefficients in Equation (1.3), such as strength,  $K$ , and strain-hardening,  $n$ , were estimated using the curve fitting method (Murugesan, Sajjad, and Jung, 2019b; Murugesan, Sajjad, and Jung, 2020b). Here, the fitted model coefficients of theoretical equations are tabulated in Table 1.1, Table 1.2, Table 1.3, and Table 1.4. The equations used as expressed below:

$$\text{Hollomon power-law equation } \sigma = K\varepsilon^n \quad (1.3)$$

$$\text{Ramberg-Osgood equation } E\varepsilon = \sigma + \alpha\sigma(\sigma/\sigma_0)^{(n-1)} \quad (1.4)$$

TABLE 1.1: Model coefficients of Ramberg-Osgood model.

Ramberg-Osgood	AA3003-H18			AA5052-H32			AZ31B		
	$\theta$ in $^\circ$			$\theta$ in $^\circ$			$\theta$ in $^\circ$		
	0	45	90	0	45	90	0	45	90
$\alpha$	0.041	0.340	0.204	2.617	1.746	1.679	0.7034	0.9959	1.1118
$n$	19.796	13.105	20.307	7.597	7.764	7.253	6.6289	6.5668	6.6042

#### 1.9.4 Plastic Anisotropy

The plastic strain ratio ( $R$ -value), which is generally employed to characterize sheet metal's ability to resist thickening or thinning, was estimated from a uniaxial tensile test adopting the conventional procedures assuming the volume constancy. For this purpose, the recorded digital images of deformation information from GOM-ARAMIS software was used. The test sample length change during the tensile test operation was acquired from recorded digital images till the fracture. Later, the collected load-displacement data from the tested samples was used to calculate the ratio of width strain and longitudinal strain, respectively. Considering the volume constancy, the longitudinal (length change) and transverse (width change) strains

were computed from the tensile sample after roughly 20% plastic strain because the standard procedures generally suggest that the best range to determine the  $R$ -value is after the material yield point and before the tensile strength. The plastic strain ratio ( $R$ ) can be determined as shown in Equation (1.5) (Lee et al., 2015; Zhuang et al., 2012; Aydin and Oz, 2018; Chen et al., 2019; Tomáš et al., 2019; Hedayati, Madoliat, and Hashemi, 2017; Kirbach et al., 2015; Ashrafi and Tuttle, 2016; Wang et al., 2010):

$$R = \frac{\varepsilon_w}{\varepsilon_t} = \frac{\ln(W_0/W_f)}{\ln(t_0/t_f)} \quad (1.5)$$

Because of difficulty in accurate thickness measurements in the test sample during the tensile test, it is presumed that the sample volume remains constant. So, Equation (1.5) can be rewritten as follows (Lee et al., 2015; Zhuang et al., 2012; Aydin and Oz, 2018; Chen et al., 2019; Tomáš et al., 2019; Hedayati, Madoliat, and Hashemi, 2017; Kirbach et al., 2015; Ashrafi and Tuttle, 2016; Wang et al., 2010):

$$R = \frac{\ln(W_0/W_f)}{\ln(L_f W_f / L_0 W_0)} \quad (1.6)$$

In Equations (1.5) and (1.6),  $W_0$ ,  $W_f$ ,  $t_0$ ,  $t_f$ ,  $L_0$ , and  $L_f$  are the original width, the final width, the thickness before the deformation, the thickness after the deformation, the original and the final length, respectively. Besides, the average plastic strain ratio ( $\bar{R}$ ) and the planar anisotropy ( $|\Delta R|$ ) can be determined using Equations (1.7) and (1.8), respectively, as expressed below (Lee et al., 2015; Zhuang et al., 2012; Aydin and Oz, 2018; Chen et al., 2019; Tomáš et al., 2019; Hedayati, Madoliat, and Hashemi, 2017; Kirbach et al., 2015; Ashrafi and Tuttle, 2016; Wang et al., 2010):

$$\bar{R} = \frac{(R_0 + 2R_{45} + R_{90})}{4} \quad (1.7)$$

$$|\Delta R| = \frac{(R_0 - 2R_{45} + R_{90})}{2} \quad (1.8)$$

The estimated aluminum alloy material tensile properties are listed in Table 1.2 (Rana, Narayanan, and Kailas, 2019; Jeon et al., 2014; Xiao et al., 2020). The uniaxial tensile tests were performed three times for each sample, considering the chosen angle to the rolling direction. The material properties are computed for each sample; from the standard deviation estimation, the error plot of yield and tensile strength of the material is plotted, as shown in Figure 1.19b. Finally, the computed plastic anisotropy properties of aluminum sheet alloys (AA3003-H18 and AA5052-H32) and magnesium alloy (AZ31B) are tabulated in Table 1.2, Table 1.3, and Table 1.4 (Murugesan, Sajjad, and Jung, 2021b).

TABLE 1.2: Mechanical properties of the AA5052–H32 material.

Parameters	Units	Angle to Rolling Direction		
		0°	45°	90°
Density	kg m <sup>-3</sup>		2680	
Modulus of Elasticity	GPa		70.3	
Poisson's ratio			0.33	
Yield strength	MPa	166.747	154.835	150.059
Ultimate tensile strength	MPa	216.212	206.010	205.068
Total elongation (%)		9.655	11.437	10.746
Plastic strain ratio ( <i>R</i> )		0.664	0.560	0.718
Hardening coefficient ( <i>K</i> )	MPa	341.250	315.950	325.700
Strain-hardening exponent ( <i>n</i> )		0.148	0.136	0.146
Average yield Strength	MPa		157.214	
Average ultimate tensile strength	MPa		209.097	
Average plastic strain ratio ( $\bar{R}$ )			0.626	
Planar anisotropy ( $ \Delta R $ )			0.131	
Average hardening coefficient ( <i>K</i> )	MPa		327.633	
Average strain-hardening exponent ( <i>n</i> )			0.143	

TABLE 1.3: Mechanical properties of the AA3003–H18 material.

Parameters	Units	Angle to Rolling Direction		
		0°	45°	90°
Density	kg m <sup>-3</sup>		2730	
Modulus of Elasticity	GPa		69.581	
Poisson's ratio			0.33	
Yield Stress	MPa	167.473	164.088	190.518
Ultimate tensile stress	MPa	205.853	192.878	214.564
Total elongation (%)		6.669	4.948	4.747
Plastic strain ratio ( <i>R</i> )		0.827	1.126	0.773
Strain hardening exponent ( <i>n</i> )		0.128	0.125	0.098
Hardening coefficient ( <i>K</i> )	MPa	362.105	335.665	342.350
Average strain hardening exponent ( <i>n</i> )			0.117	
Average hardening coefficient ( <i>K</i> )	MPa		346.707	

TABLE 1.4: Mechanical properties of the AZ31B material.

Parameters	Units	Angle to Rolling Direction		
		0°	45°	90°
Density	kg m <sup>-3</sup>		1770	
Modulus of Elasticity	GPa		45.126	
Poisson's ratio			0.35	
Yield Stress	MPa	176.265	182.388	193.767
Ultimate tensile stress	MPa	266.047	270.874	272.914
Total elongation (%)		23.33	23.178	21.718
Plastic strain ratio ( <i>R</i> )		1.26 1	1.662	1.488
Strain hardening exponent ( <i>n</i> )		0.175	0.179	0.179
Hardening coefficient ( <i>K</i> )	MPa	433.45	447.415	450.115
Average strain hardening exponent ( <i>n</i> )			0.178	
Average hardening coefficient ( <i>K</i> )	MPa		443.66	

### 1.9.5 Hot Tensile Test of AISI-1045 Steel

The AISI-1045 medium carbon steel material was investigated in the present research work, and the chemical composition (in wt.%) of the steel is listed in Table 1.5. The

specimens were prepared by the water jet cutting process from the AISI-1045 steel plates and were further used in uniaxial tensile tests to obtain the flow stress-strain data to characterize the hot deformation flow behavior. In detail, the tensile test specimens were prepared with a gauge length of 25 mm and a thickness of 3 mm, according to the ASTM-E8M-subsize standard. Tensile tests were performed at elevated deformation temperatures (650–950 °C) and high strain rates (0.05–1.0 s<sup>-1</sup>) on a computer-controlled servo-hydraulic testing machine, as shown in Figure 1.20a, which can heat the specimen to a maximum of 950 °C. From Figure 1.20a, it can be seen that the clamped tensile specimen was covered with the isolation part to achieve isothermal conditions, and, in addition, a detailed view of the prepared tensile specimen, which was inside the testing machine, is shown in Figure 1.20b. Before conducting the tests, as displayed in Figure 1.20b, the calibrations were done using the thermocouples to determine the heating time to obtain an approximately uniform temperature distribution for the specific temperature value, and then, the noted details were used to conduct the experiments. During the experiment, two specimens were tested for each case, and the averaged load-stroke data were converted into the true stress-strain data using the standard equations of the simple tensile tests. The obtained flow stress-strain data are displayed in Figure 1.21. Subsequently, the elastic region was removed from the flow stress-strain curve in order to get the true plastic flow stress-strain data for the purpose of estimation of the constitutive model parameters.

TABLE 1.5: Chemical composition of AISI-1045 medium carbon steel (in wt.%).

C	Fe	Mn	P	S
0.42–0.50	98.51–98.98	0.60–0.90	≤0.04	≤0.05

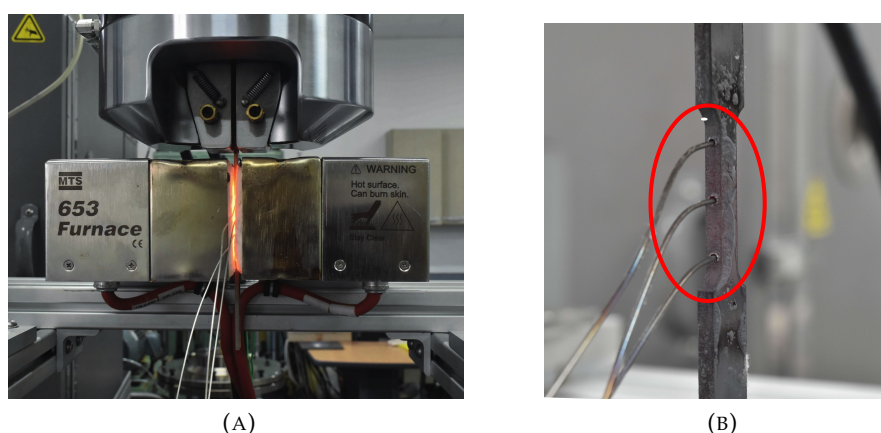


FIGURE 1.20: Experimental set-up. (a) Test machine; (b) Specimen with thermocouples.

### 1.9.6 Microstructural Characterization

For evaluating micro-structure evolution in AISI-1045 medium carbon steel material, the FESEM (MIRA3 TESCAN, secondary electron detector, Jeju National University, Jeju-si, Jeju Island, South Korea) along with the EDS mapping setup was utilised in this research work. Using the test setup, the deformation temperature (850 °C, 950 °C) and strain rate (0.05–0.5 s<sup>-1</sup>) dependent surface morphology, thickness and elemental identification analysis were observed at the fractured surface for various magnifications as illustrated in Figure 1.22. From Figure 1.22a,e,i, for strain rates at deformation temperature (850 °C), it can be seen that specimen growth and nucleation was found to be coarse at low strain rate and as strain rate kept increasing, the nucleation and growth transformation was noticed to be finer, uniform, and homogeneous at a 50 μm scale. As seen in Figure 1.22b,f,j, the FESEM images are presented with micro and nanopores, a highly interconnected porous structure observed at 20 μm scale. However, observation at a higher magnification scale level (5 μm) revealed that a porous and interconnected structure was found to be discontinuous and irregular as shown in Figure 1.22c,g,k. In addition, Figure 1.22i,k comparisons against Figure 1.22m,n show that due to temperature changes, a macro

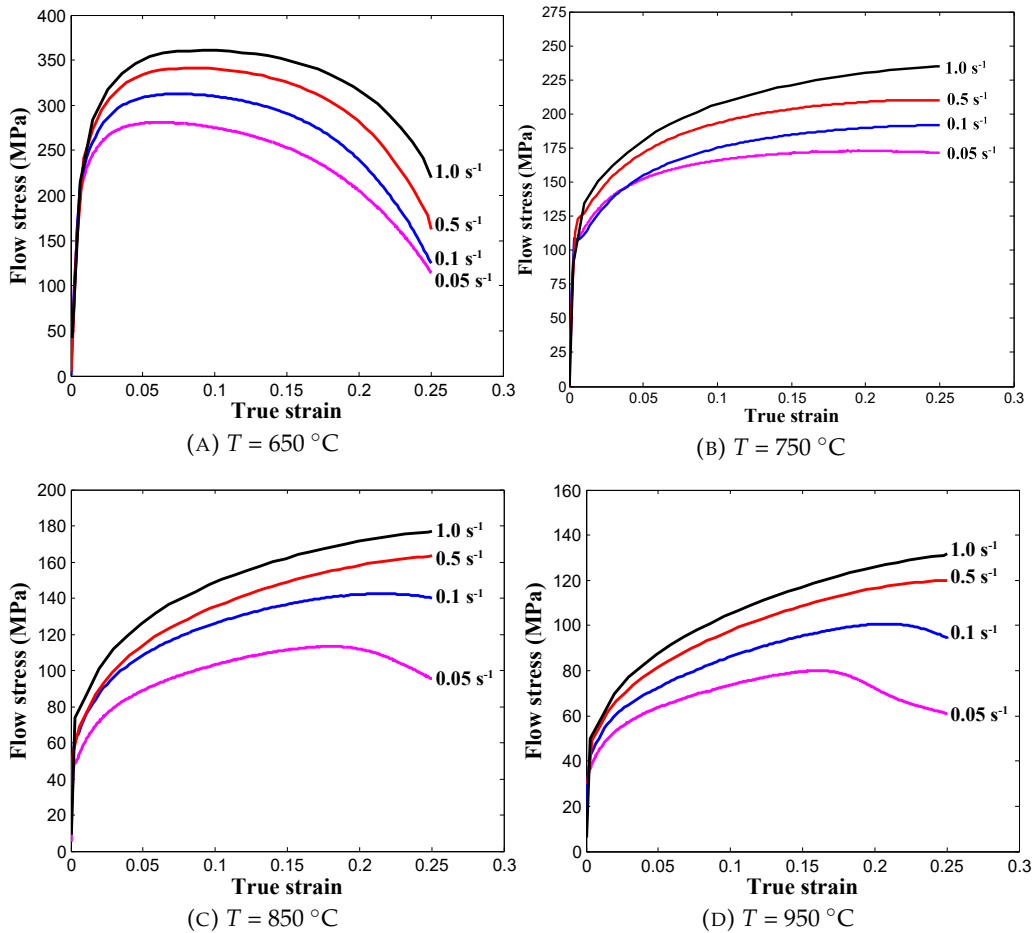


FIGURE 1.21: True stress-strain data obtained from hot tensile tests.

porous structure was formed and furthermore, we observed the apparent growth, nucleation of nanoneedles, and reduction of pore size. Moreover, the magnified portion (at  $5\text{ }\mu\text{m}$  scale) of the sample image confirms the formation of micro-fibrils and moderate growth of nanoneedles. The reason behind this clear difference in microstructure is possibly due to slow and strong self-association of grains at low temperature. Besides, at magnification  $100\text{ }\mu\text{m}$  scale, for test conditions ( $850\text{ }^{\circ}\text{C}$ ) and ( $950\text{ }^{\circ}\text{C}$ ) at strain rate ( $0.5\text{ s}^{-1}$ ), the EDS mapping analysis of test specimens proves the presence of iron (Fe) and carbon (C) elements throughout the scanned surface. The microstructure images of fractured specimens at  $500\text{ }\mu\text{m}$  scale, as shown



in Figure 1.22d,h,l,o, confirms the reduction of specimen thickness at the fracture location at tested conditions. The inset images show the rough surface morphology at fractured surface (5  $\mu\text{m}$  scale).

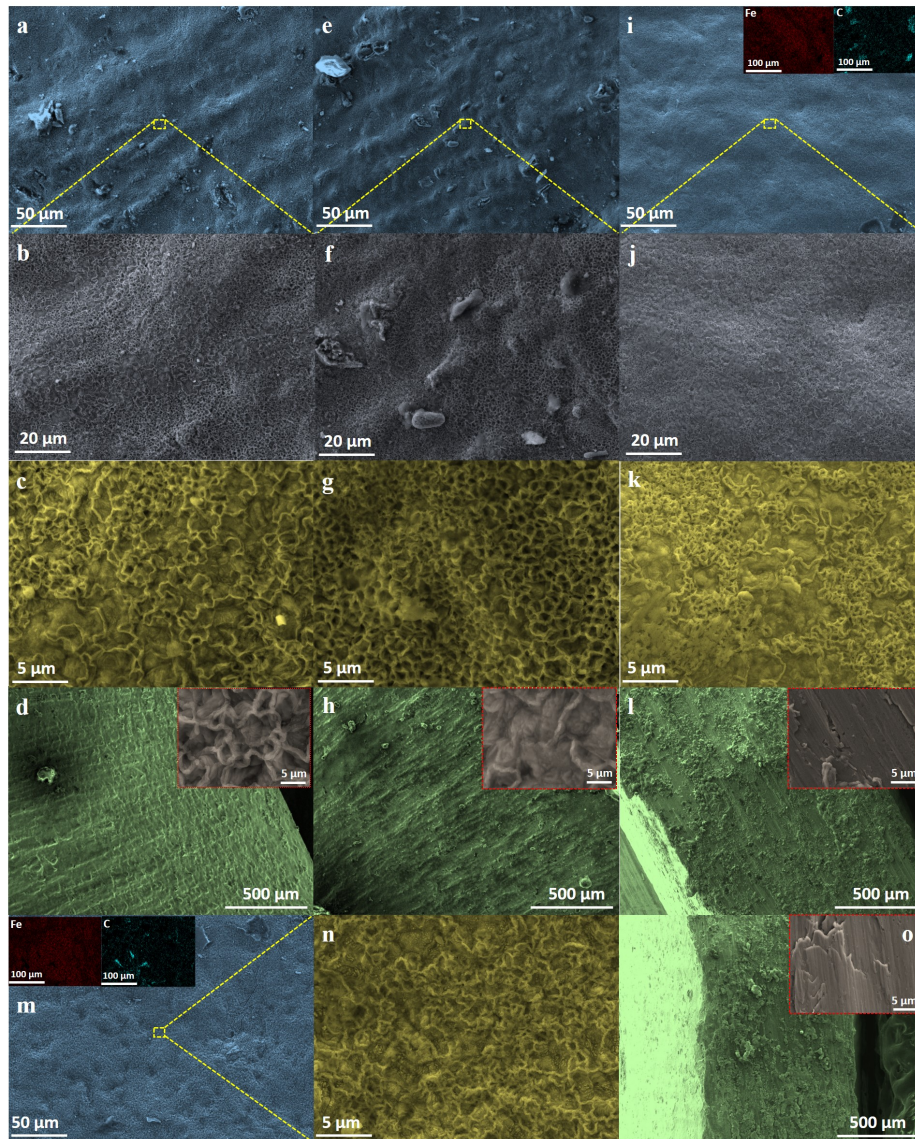


FIGURE 1.22: Micro-structure mapping images of AISI-1045 medium carbon steel material at deformation temperature (850  $^{\circ}\text{C}$ ). (a–d)  $0.05\text{ s}^{-1}$ ; (e–h)  $0.1\text{ s}^{-1}$ ; (i–l)  $0.5\text{ s}^{-1}$ ; (m–o)  $950\text{ }^{\circ}\text{C}/0.5\text{ s}^{-1}$ ; observation by FESEM and EDS on various magnifications (Murugesan and Jung, 2019a; Murugesan and Jung, 2019b; Murugesan, Sajjad, and Jung, 2019a; Murugesan, Sajjad, and Jung, 2020c).



## **1.10 Conclusions**

The incremental forming methods, involving the fundamentals and modeling procedures, have been comprehensively reviewed here. By starting with the theoretical background of the ISF process, this chapter was followed by including the material characterization. The cold and hot forming process fundamentals were well-reviewed with the help of published research articles. Furthermore, the importance of process forming parameters was studied for effectively conducting this research work. Subsequently, the lubrication selection as a combination of oil and grease was carried out well using literature guidelines. Besides, the material characterization was performed on the chosen materials, namely AA3003–H18, AA5052–H32, and AZ31B, for determining their material properties at room temperatures. In addition, the hot tensile tests were conducted to propose constitutive models for modeling the numerical simulation of the hot forming process. Eventually, the micro-structure evaluations were carried out on the test samples to describe their deformation behavior before and after the failure. Overall, as this chapter is well-arranged, it can be used as a guideline for understanding and performing not only the ISF process several metal forming process numerically as well as experimentally.

## Chapter 2

# Johnson-Cook Material and Failure Models

### 2.1 Summary

The objective of this work was to formulate an appropriate flow stress model to characterize the flow behavior of AISI-1045 medium carbon steel over a practical range of deformation temperatures (650–950 °C) and strain rates (0.05–1.0 s<sup>-1</sup>). Subsequently, the Johnson-Cook flow stress model was adopted for modeling and predicting the material flow behavior at elevated temperatures. Furthermore, surrogate models were developed based on the constitutive relations, and the model constants were estimated using the experimental results. As a result, the constitutive flow stress model was formed and the constructed model was examined systematically against experimental data by both numerical and graphical validations. In addition, to predict the material damage behavior, the failure model proposed by Johnson and Cook was used, and to determine the model parameters, seven different specimens, including flat, smooth round bars and pre-notched specimens, were tested at room temperature under quasi strain rate conditions. From the results, it can be seen that the developed model over predicts the material behavior at a low temperature for all strain rates. However, overall, the developed model can produce a fairly accurate

and precise estimation of flow behavior with good correlation to the experimental data under high temperature conditions. Furthermore, the damage model parameters estimated in this research can be used to model the metal forming simulations, and valuable prediction results for the work material can be achieved.

## 2.2 Introduction

Understanding the damage caused by plastic deformation in the metal forming process is essential to make safe the operation of structures in the working field as well as to reduce the cost and time consumption of the experiments. In industrial practice, the JC material and damage model is extensively incorporated into most of the available finite element (FE) tools to model metal forming simulations because of its ability to predict the model parameters with less effort. It is undeniable that the well-made and reliable proposed flow stress model is more supportive over a wide range of strain rates and elevated temperatures for product design in terms of predicting the material ductility behavior efficiently. Even though the flow stress models are broken down into different categories, such as physically-based, empirical, and semi-empirical, the aim of these models to achieve accurate prediction of the material behavior for a specific material remains the same (He et al., 2018b). So, developing a proper flow stress model for the design process is essential to predict material deformation behavior at high strain rates and deformation temperatures, and, as a result, reasonable research has been performed considering various materials. Aviral Shrot et al. (Shrot and Baker, 2012) proposed a method using the Levenberg-Marquardt search algorithm for the inverse identification of JC material parameters. A set of JC parameters was used to develop an idealized FE model for the machining process. Then, the inverse identification method was used to estimate the JC by looking at the chip morphology and the cutting force during the

process. They concluded that it is possible to re-identify the model parameters by inverse methods; however the estimated parameters from the simulation results were almost identical to the original set. Luca Gambirasio et al. (Gambirasio and Rizzi, 2014) adopted various procedures for calibrating the JC model parameters under the high strain rate phenomenon by expressing the deviatoric behavior of elasto-plastic materials. In addition, the Taylor impact test experimental data was also included for the evaluation of the JC strength model parameters.

From a literature survey, it was identified that constructing a proper FE model typically requires expensive experimental effort, and appropriate modeling of fracture behavior is necessary, and the damage model should consider both damage initiation and damage evolution. Even though many researchers were worked with the original JC model, only very few researchers were reported about the strategy to optimize the JC model constants to improve the model predictability. Furthermore, so far, there has been no attempt to develop a detailed JC material and damage model for AISI-1045 medium carbon steel material. The aim of this research was to identify the most consistent JC constitutive and damage model parameters for AISI-1045 medium carbon steel material, and, in addition, to exploit an empirical model approach in order to fit the constitutive equation using experimental data. Isothermal tensile tests were carried out at elevated temperatures (650–950 °C) and at low strain rates (0.05–1.0 s<sup>-1</sup>) to determine the model properties. To improve the predictability of the JC material model, an optimization procedure based on the non-linear programming solver, find minimum of constrained nonlinear multivariable function (fmincon), was employed, considering the strain rate hardening and the thermal softening parameters. Also, an extensive series of experiments, including un-notched and pre-notched flat and round bar specimens, were conducted at quasi-static strain rates (0.0001–0.05 s<sup>-1</sup>) to estimate the damage model parameters of the JC model.

## 2.3 Johnson-Cook Material Model

The metallic material relationships between stress and strain can be described by the JC model under the conditions of large deformation, high strain rate and elevated temperatures. Being in a simple form and as it requires less effort to estimate the material constants, it has been widely employed by many researchers to predict the flow behavior of materials. The flow stress model is expressed as follows (Abbasi-Bani et al., 2014; He et al., 2013; Maheshwari, 2013; Akbari, Mirzadeh, and Cabrera, 2015; Zhan et al., 2014; Samantaray, Mandal, and Bhaduri, 2009):

$$\sigma = (A + B\varepsilon^n)(1 + C \ln \dot{\varepsilon}^*)(1 - T^{*m}), \quad (2.1)$$

where  $\sigma$  is the equivalent stress, and  $\varepsilon$  is the equivalent plastic strain. The material constants are  $A$ ,  $B$ ,  $n$ ,  $C$  and  $m$ .  $A$  is the yield stress of the material under reference conditions,  $B$  is the strain hardening constant,  $n$  is the strain hardening coefficient,  $C$  is the strengthening coefficient of strain rate, and  $m$  is the thermal softening coefficient (Cao et al., 2014b).

The three parenthesis components in Equation (2.1) represent, from left to right, the strain hardening effect, the strain rate strengthening effect and the temperature effect, which influences the flow stress values (Murugesan et al., 2017). In the flow stress model,  $\dot{\varepsilon}^*$  and  $T^*$  are

$$\dot{\varepsilon}^* = \frac{\dot{\varepsilon}}{\dot{\varepsilon}_{\text{ref}}}, \quad T^* = \frac{T - T_{\text{ref}}}{T_m - T_{\text{ref}}},$$

where  $\dot{\varepsilon}^*$  is the dimensionless strain rate,  $T^*$  is the homologous temperature,  $T_m$  is the melting temperature of the material, and  $T$  is the deformation temperature.  $\dot{\varepsilon}_{\text{ref}}$  and  $T_{\text{ref}}$  are the reference strain rate and the reference deformation temperature, respectively (Murugesan et al., 2017). In the present study, regarding the experimental conditions, the reference strain rate,  $\dot{\varepsilon}_{\text{ref}}$ , and the reference temperature,  $T_{\text{ref}}$ , were

taken as 1223 K and  $1 \text{ s}^{-1}$ , respectively. In accordance with the reference conditions, the material constant,  $A$ , was determined to be 50.103 MPa for further calculations.

### 2.3.1 Determination of Material Constants $B$ and $n$

When the deformation temperature is  $T = T_{ref} = 1223 \text{ K}$ , and the deformation strain rate is  $\dot{\epsilon} = \dot{\epsilon}_{ref} = 1 \text{ s}^{-1}$ , Equation (2.1) is modified as follows (Murugesan et al., 2017):

$$\sigma = (A + B\epsilon^n). \quad (2.2)$$

Here, the influences of strain rate strengthening and thermal softening effects are neglected. By rearranging Equation (2.2) and taking the natural logarithm on both sides of Equation (2.2), the modified equation can be obtained as shown below (Murugesan et al., 2017):

$$\ln(\sigma - A) = n \ln\epsilon + \ln B. \quad (2.3)$$

By substituting the flow stress and strain values at the reference deformation conditions into Equation (2.3), the linear relationship plot between  $\ln(\sigma - A)$  and  $\ln\epsilon$  was drawn, and then the first-order regression model was used to fit the data points as depicted in Figure 2.1. From Figure 2.1, it is noted that more than 96 percent of the data lies very close to the regression line, which shows the better predictability of the data distribution. As a result, the material constants  $B$  and  $n$  were estimated to be 176.09 MPa and 0.5176 from the slope and intercept of the fitted curve.

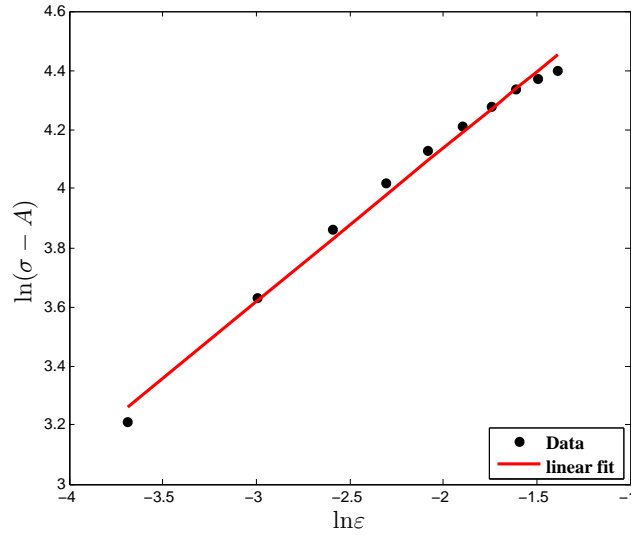


FIGURE 2.1: Relationship between  $\ln(\sigma - A)$  and  $\ln\dot{\epsilon}$  under the reference conditions.

### 2.3.2 Determination of Material Constant C

When the deformation temperature is  $T = T_{ref} = 1223$  K, Equation (2.1) can be remodeled as shown below (Murugesan et al., 2017):

$$\sigma = (A + B\epsilon^n)(1 + C \ln\dot{\epsilon}^*), \quad (2.4)$$

whereas, the influences of thermal softening effects are ignored. Rearranging Equation (2.4) will result in the following form:

$$\frac{\sigma}{(A + B\epsilon^n)} = (1 + C \ln\dot{\epsilon}^*). \quad (2.5)$$

Initially, the values of material constants  $A$ ,  $B$  and  $n$ , obtained in Section 2.3.1, were substituted into Equation (2.5); then,  $\frac{\sigma}{(A + B\epsilon^n)} \sim \ln\dot{\epsilon}^*$  was drawn as a curve, as shown in Figure 2.2. Subsequently, linear fitting was carried out using the first-order regression model with an intercept value of 1, considering flow stress values at four strain rates ( $0.05 \text{ s}^{-1}$ ,  $0.1 \text{ s}^{-1}$ ,  $0.5 \text{ s}^{-1}$  and  $1 \text{ s}^{-1}$ ). Finally, the slope of the fitting curve,

the material constant value,  $C$ , was estimated to be 0.1056. Here, it is important to mention that at first, the material constant,  $C$ , was estimated based on the traditional method considering all strain values. However, in this research, the optimization procedure was adopted to find out the optimum  $C$  value in order to reduce the prediction error compared with the experimental data. For this purpose, the material constant,  $C$ , was estimated at ten discrete strain values, and, as a result, ten different values of  $C$  were obtained from the fitted linear model. Thereafter, the estimated values were further used in the optimization calculations.

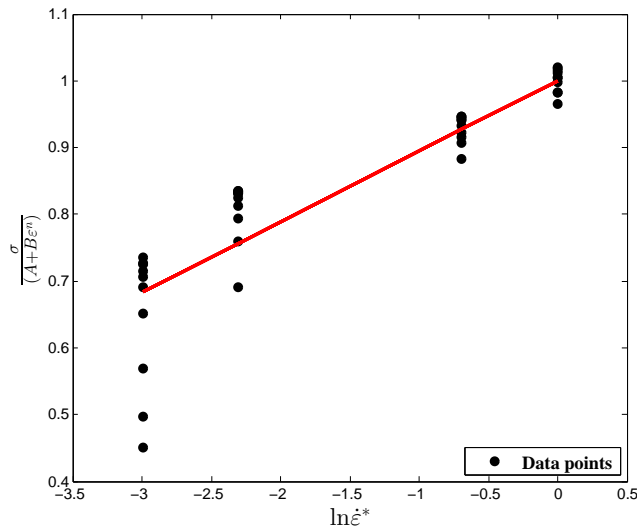


FIGURE 2.2: Relationship between  $\frac{\sigma}{(A+B\epsilon^n)}$  and  $\ln\dot{\epsilon}^*$  under the reference conditions.

### 2.3.3 Determination of the Material Constant, $m$

When the deformation strain rate is  $\dot{\epsilon} = \dot{\epsilon}_{ref} = 1 \text{ s}^{-1}$ , Equation (2.1) can be simplified as (Murugesan et al., 2017):

$$\sigma = (A + B\epsilon^n)(1 - T^{*m}). \quad (2.6)$$



Here, the influences of the strain rate strengthening effect are neglected. Equation (2.6) is rearranged into the following form:

$$1 - \frac{\sigma}{(A + B\varepsilon^n)} = T^{*m}. \quad (2.7)$$

Taking the natural logarithm on both sides of Equation (2.7), the following equation can be obtained as:

$$\ln \left[ 1 - \frac{\sigma}{(A + B\varepsilon^n)} \right] = m \ln T^*. \quad (2.8)$$

Substituting the values of material constants  $A$ ,  $B$  and  $n$  into Equation (2.8) and fitting the data points using the first-order regression model, as shown in Figure 2.3, the material constant,  $m$ , was determined to be 0.5655 from the slope of fitted curve considering the conventional method. As with the material constant,  $C$ , from the estimation at ten discrete strain points, ten different  $m$  values were obtained from the flow stress values of two different temperatures (923 K, 1123 K) for optimization purposes. Hereafter, a bounds constrained optimization procedure was used to find the optimum solution of the material constants  $C$  and  $m$ , and the optimization formulation used in the present work is expressed below:

$$\left\{ \begin{array}{l} \text{Minimize:} \\ \quad x \\ \quad \text{AARE} = \frac{1}{n} \sum_{i=1}^n \left| \frac{\sigma_{\text{exp}}^i - \sigma_{\text{pred}}^i}{\sigma_{\text{exp}}^i} \right| \times 100\%, \\ \text{where, } \sigma_{\text{pred}} = (A + B\varepsilon^n)(1 + x(1)\ln\dot{\varepsilon}^*)(1 - T^{*x(2)}) \\ \text{subjected to} \quad \left\{ \begin{array}{l} C_{\min} \leq x(1) \leq C_{\max} \\ m_{\min} \leq x(2) \leq m_{\max} \end{array} \right. \end{array} \right.$$

To solve this optimization problem, the nonlinear programming solver, `fmincon`,

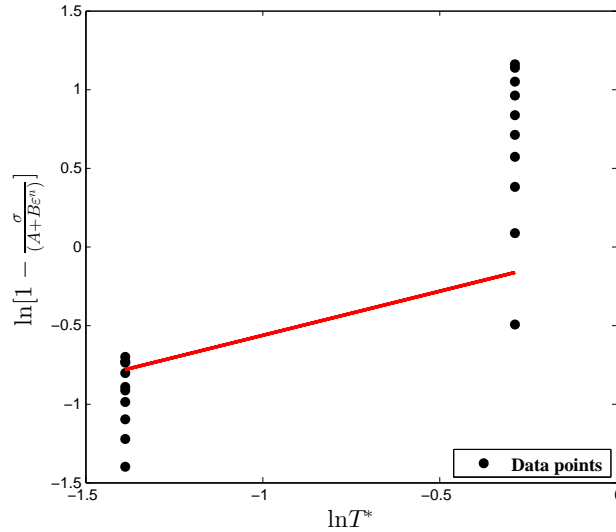


FIGURE 2.3: Relationship between  $\ln \left[ 1 - \frac{\sigma}{(A+B\epsilon^n)} \right]$  and  $\ln T^*$  under the reference conditions.

was used with the interior-point (IP) algorithm to minimize the average absolute relative error between the experimental data and the predicted data. The main reason to use the IP algorithm was because the aim was to find the minimum of an objective function in the presence of bound constraints alone. The optimization problem was solved after 29 successful iterations with the function value, the minimized prediction error, 17.62%, and the optimum solutions for the material constants  $C$  and  $m$  were 0.095 and 0.6622, respectively. The material constants, which were estimated from the constitutive equations and the optimization procedure of the proposed JC model, are listed in Table 2.1.

TABLE 2.1: JC material model parameters of AISI-1045 steel.

Regular JC Model					Optimized JC Model				
$A$ (MPa)	$B$ (MPa)	$n$	$C$	$m$	$A$ (MPa)	$B$ (MPa)	$n$	$C$	$m$
50.103	176.091	0.5176	0.1056	0.5655	50.103	176.091	0.5176	0.095	0.6622

Thus, the material constants were substituted into Equation (2.1) to form a final

flow stress model. Thereafter, the relations among stress,  $\sigma$ , strain,  $\varepsilon$ , the deformation strain rate,  $\dot{\varepsilon}$ , and the deformation temperature,  $T$ , were established according to the JC model, as follows:

$$\hat{\sigma}_{\text{pred}} = (50.103 + 176.09\varepsilon^{0.518}) \left( 1 + 0.095 \ln \left( \frac{\dot{\varepsilon}}{1.0} \right) \right) \left( 1 - \left( \frac{T - 1223}{1623 - 1223} \right)^{0.662} \right) \text{ (MPa)}.$$

## 2.4 Johnson-Cook Damage Model

Johnson and Cook proposed that fracture strain typically depends on the stress triaxiality ratio, the strain rate and the temperature. The JC fracture model can be written as follows (Banerjee et al., 2015; Zhanga, Outeirob, and Mabroukic, 2015):

$$\varepsilon_f = \left[ D_1 + D_2 \exp \left( D_3 \left( \frac{\sigma_m}{\sigma_{\text{eq}}} \right) \right) \right] [1 + D_4 \ln (\dot{\varepsilon}_p^*)] [1 + D_5 T^*] \quad (2.9)$$

where  $D_1$  to  $D_5$  are the damage model constants,  $\sigma_m$  is the mean stress, and  $\sigma_{\text{eq}}$  is the equivalent stress (Murugesan et al., 2017). The damage of an element is defined based on a cumulative damage law, and it can be represented in a linear way as shown below (Murugesan et al., 2017; Buzyurkin, Gladky, and Kraus, 2015):

$$D = \sum \left( \frac{\Delta \varepsilon}{\varepsilon_f} \right), \quad (2.10)$$

where  $\Delta \varepsilon$  is the equivalent plastic strain increment, and  $\varepsilon_f$  is the equivalent strain to fracture under the present conditions of stress, strain rate and temperature. Due to the fracture occurrence, the material strength reduces during deformation, and the constitutive relation of stress for the damage evolution can be expressed as (Banerjee et al., 2015)

$$\sigma_D = (1 - D)\sigma_{\text{eq}}. \quad (2.11)$$

In Equation (2.11),  $\sigma_D$  is the damaged stress state, and  $D$  is the damage parameter, ( $0 \leq D < 1$ ). Furthermore, the stress triaxiality (Bai and Wierzbicki, 2008; Brunig et al., 2008; Mirone and Corallo, 2010; Cao et al., 2014a; Bao, 2005) and the equivalent stress can be obtained from undamaged material considering the plastic behavior until the necking formation (Murugesan et al., 2017).

At first, the un-notched and pre-notched specimens were fabricated using the machine cutting process, and more than one sample was used to obtain the flow curve to get a better outcome in terms of the mechanical properties of the material in order to control the experimental error. A series of experiments including un-notched and pre-notched round bar, flat specimens were carried out simultaneously, as shown in Figure 2.4, at room temperature considering a wide range of quasi-static strain rate conditions to investigate the effect of stress triaxiality on the damage behavior of AISI-1045 medium carbon steel material. The flow curves accomplished from the tests were decomposed into elastic and plastic regions until necking for the identification of material properties as well as for the numerical model inputs. In addition, the mechanical properties of the material were determined carefully from performed experiments, because these properties needed to replicate the material's behavior in the real situations as accurately as possible. Furthermore, the estimated properties were incorporated into commercial tools, and the work hardening behavior was simulated by considering the multi-linear isotropic hardening model for the assessment of stress triaxiality. The FE models were modeled using half symmetry conditions and meshed by different mesh sizes to reduce the computational time without affecting the accuracy, as shown in Figure 2.5a. From the outcome, a good correlation between experimental observations and the FE model was achieved in the elastic and plastic range until necking. The estimation of mechanical properties from the experiments was done perfectly and can be further used to perform the estimation of stress triaxiality without any barrier.

Subsequently, the stress components, such as,  $\sigma_1$ ,  $\sigma_2$ , and  $\sigma_3$ , were chosen from the center of the cross-section of the specimen. Ductile damage mostly tends to occur at this region due to maximum stresses, as displayed in Figure 2.5b. Thus, the stress components were substituted into Equation (2.12) to determine the mean stress,  $\sigma_m$ , and the equivalent stress,  $\sigma_{eq}$ , and the set of stress triaxialities estimated for an entire specimens is listed in Table 2.2.

$$\sigma^* = \frac{(\sigma_1 + \sigma_2 + \sigma_3)}{3 \times \sqrt{0.5 \times [(\sigma_1^2 - \sigma_2^2) + (\sigma_2^2 - \sigma_3^2) + (\sigma_3^2 - \sigma_1^2)]}} \quad (2.12)$$



FIGURE 2.4: Experimental set-up to perform tension test at room temperature. (a) Test machine; (b) Un-notched and pre-notched specimens.

Rearranging Equation (2.9) by neglecting the effects of strain rate and temperature, the failure model equation can be rewritten only in terms of the stress triaxiality effect with respect to fracture strain as follows (Murugesan et al., 2017):

$$\epsilon_f = D_1 + D_2 \exp(D_3 \sigma^*). \quad (2.13)$$

By substituting the stress triaxialities and corresponding fracture strain values

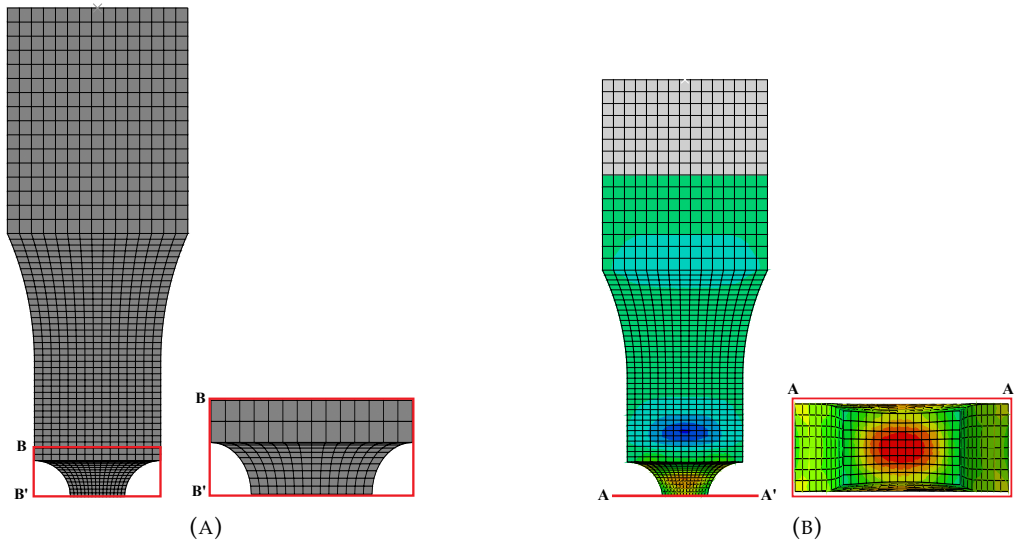


FIGURE 2.5: Finite element models. (a) Fine mesh in notching region; (b) Stress estimation region.

TABLE 2.2: Stress triaxiality data obtained from FE simulations.

T	$\dot{\epsilon}$ (s <sup>-1</sup> )	Flat 6w	N-R0	N-R1	N-R2	N-R3
27 °C	0.001	0.3345	–	0.8523	0.7756	–
	0.005	0.3337	–	0.9017	0.7782	–
	0.010	0.3332	–	0.8961	0.7852	–
	0.050	0.3333	–	0.9015	0.7829	–
	0.0001	–	0.3359	0.5082	0.6070	0.7473
	0.001	–	0.3299	0.4989	0.6152	0.7641
	0.010	–	–	0.4897	0.5983	0.7438

into Equation (2.13), the relationship plot,  $\epsilon_f \sim \sigma^*$ , was developed, and from the coefficients of the fitted equation, as shown in Figure 2.6, the model parameters  $D_1$ ,  $D_2$  and  $D_3$  were computed. Subsequently, the strain rate and the temperature dependent damage parameters  $D_4$  and  $D_5$  were obtained from two sets of high temperature and strain rate data by interpreting the failure strain variation (Murugesan et al., 2017). The estimated JC fracture model parameters are outlined in Table 2.3, and the model parameters can be used in the metal forming applications to predict the ductile fracture behavior.

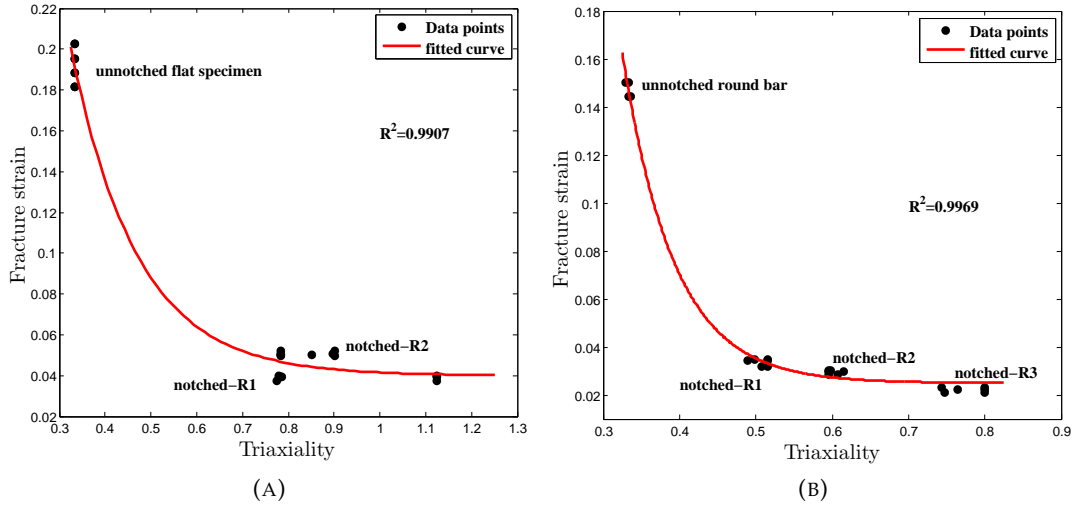


FIGURE 2.6: Relationship plot of strain to fracture and stress triaxiality.

TABLE 2.3: Johnson-Cook fracture model parameters.

Round Bar and Notched Specimens					Flat and Notched Specimens				
D1	D2	D3	D4	D5	D1	D2	D3	D4	D5
0.025	16.93	-14.8	0.0214	0	0.04	1.519	-6.905	-0.023	1.302

## 2.5 Discussion

Numerous isothermal experiments were conducted over a practical range of deformation temperatures (650–950 °C) and strain rates (0.05–1.0 s<sup>-1</sup>) to develop the JC material model to predict the flow stress data of AISI-1045 medium carbon steel. In addition, the experimental data obtained from the quasi-static strain rate tensile tests at room temperature were employed for the evaluation of damage model parameters. To verify the model adequacies and predictability, the proposed constitutive model predictions were compared with the experimental observations and were also incorporated into the numerical simulations for inverse calibrations. Figure 2.7 depicts the comparison of experimental stress-strain flow curves with the predicted flow curves by using the proposed JC model, whereas the model parameters were



estimated from the optimization method. The data plotted in Figure 2.7 and the numerical data outlined in Table 2.4 clearly display that the presented optimized JC model is in good agreement with the experimental observations at higher temperatures for all strain rates, and on the contrary, the model cannot offer a better prediction of flow stress at the deformation temperature, 650 °C, for all tested strain rates. Thus, from the prediction error comparison, the flow stress data obtained in the optimized JC model were found to be more consistent with the experimental data than the conventional JC model.

TABLE 2.4: Statistical measurements of optimized JC model.

Conditions	$R^2$	Overall- $R^2$	AARE (%)	Overall-AARE (%)
923 K	0.0115		40.9341	
1123 K	0.8679	0.4836	5.9313	17.6112
1223 K	0.8419		5.9689	

To perform the model evaluation, standard statistical measurements such as  $R^2$  and an average absolute relative error (AARE) were adopted to quantify the proposed JC model predictability at discrete strains with an interval of 0.025 for all strain rates and temperatures. The  $R^2$  provides information about the prediction strength of the linear relationship between the experimental observations and the predicted values, whereas AARE was estimated through a term-by-term comparison of the relative error. To perform this quantification, the following expressions were employed (Kyunghoon et al., 2017; Mohanraj, Beom-Soo, and Kyunghoon, 2015):

$$R^2 = 1 - \frac{\sum_{i=1}^n (\sigma_{\text{exp}}^i - \sigma_{\text{pred}}^i)^2}{\sum_{i=1}^n (\sigma_{\text{exp}}^i - \bar{\sigma}_{\text{exp}})^2}, \quad (2.14)$$

$$\text{AARE} = \frac{1}{n} \sum_{i=1}^n \left| \frac{\sigma_{\text{exp}}^i - \sigma_{\text{pred}}^i}{\sigma_{\text{exp}}^i} \right| \times 100\%, \quad (2.15)$$

where  $\sigma_{\text{exp}}$ ,  $\sigma_{\text{pred}}$ ,  $\bar{\sigma}_{\text{exp}}$  are the experimental flow stress, the predicted flow stress, and the mean flow stress, respectively, and  $n$  is the total number of data points.

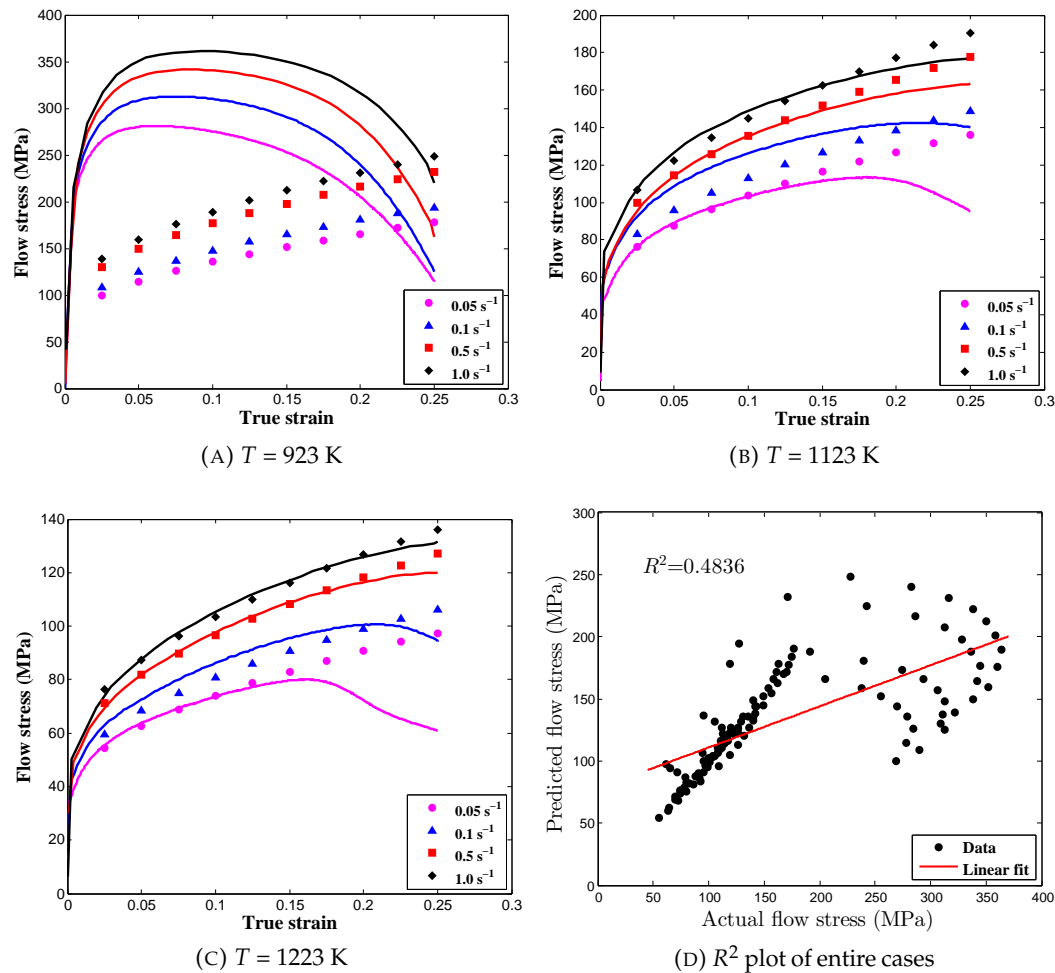


FIGURE 2.7: Comparison between experimental and predicted flow stress data using the modified Johnson-Cook model.

In this research, each test condition was examined by estimating the values of  $R^2$  and AARE for each case rather than the traditional method, in which the entire data set was used to compute the statistical parameters as mentioned in Table 2.4. In this way, the prediction strength of the proposed JC model can be discussed in detail in terms of each and every test condition. The predicted flow curves and

the graphical validation of the optimized JC model are shown in Figure 2.7 for all strain rates and deformation temperatures. Figure 2.7a depicts the comparison plot between predicted flow curves and experimental data and it shows that the developed model overpredicts the flow stress data. The numerical values  $R^2$  and AARE were found to be 0.0012, lacking the prediction of the linear relationship as illustrated in Figure 2.8a, and 40.9341, respectively. From these numbers, it is clear that the optimized JC model cannot predict the material behavior at a deformation temperature of 923 K for all strain rate conditions. However, somehow, as shown in Figure 2.8a, there is some abnormal behavior in the distribution of data points. To verify this phenomenon, the residual plot, decomposed into three parts—low, exact, and high predictions—is plotted in Figure 2.8d. From Figure 2.8d, it is clearly shown that the proposed model mostly under predicts the flow stress, as the most of the data points were distributed linearly, somehow in exponential form, above the exact prediction line. This phenomenon explains that by adding some noise function into a negative linear or exponential form to the original flow stress model, this prediction error can be avoided. Likewise, Figure 2.7b shows that at a deformation temperature of 1123 K for all strain rates, it is evident that most of the predicted flow stress data are close to the experimental observations, whereas Figure 2.8b exhibits a good correlation between actual and predicted data. In addition, the computed corresponding values of the statistical parameters,  $R^2$ , 0.8679, and AARE, 5.9313%, show that the proposed JC model has considerable potential to predict the flow stress under the tested conditions. Furthermore, Figures 2.7c and 2.8c illustrate the good correlation between experimental and predicted data under the tested conditions.  $R^2$  and AARE were found to be 0.8419 and 5.9689%, respectively. Besides, it is noted that the prediction error minimization considering the material parameters,  $c$  and  $m$  using the optimization procedure led to significant improvement in the JC model prediction. For all test conditions, the overall AARE reduced from 18.12% to

17.61%. The differences between the models may be small but this small error can cause the false estimation of flow stress which leads to the inaccurate prediction of material behavior.

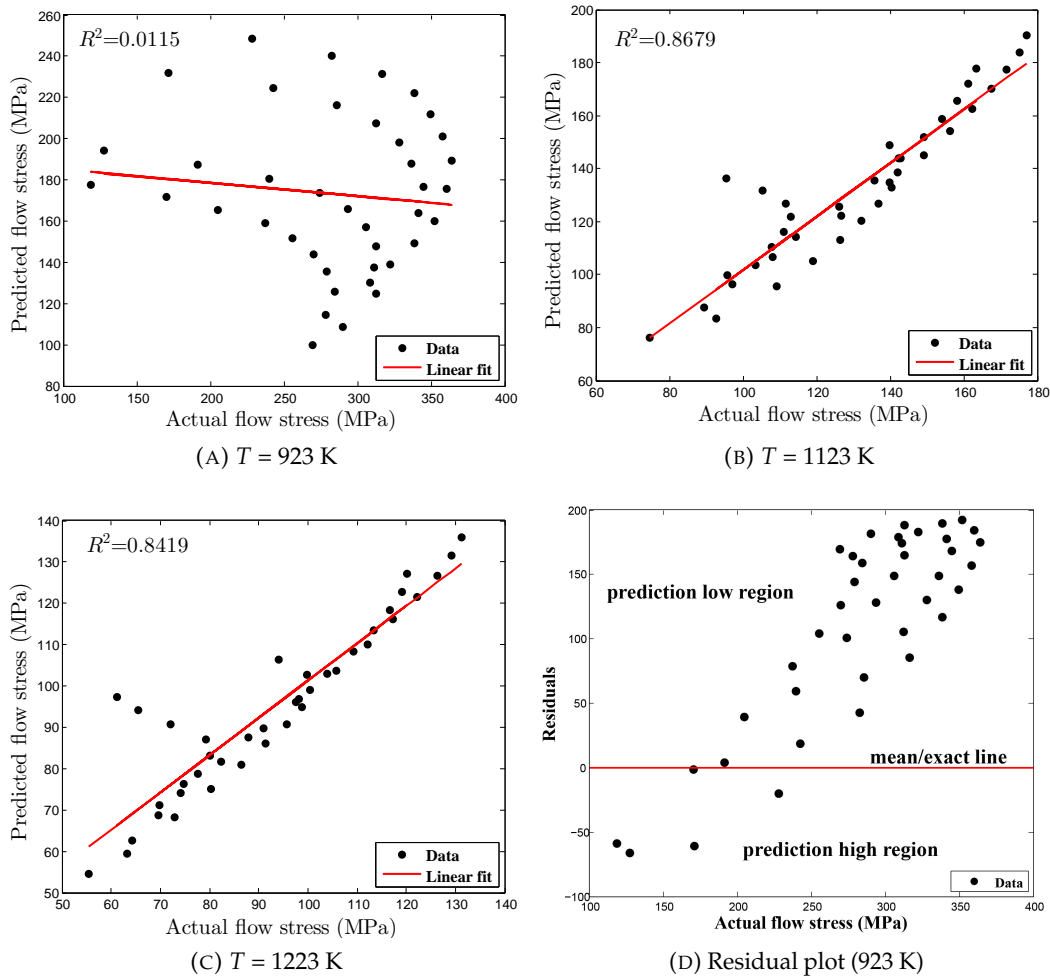


FIGURE 2.8: Relationship plots.

Overall, it was observed that the optimized JC model for AISI-1045 medium carbon steel can be used for flow stress prediction at high temperatures over the entire tested range of strain rates. Even though the overall flow stress prediction was good, in a few cases, for example, at deformation temperature 1123 K and at a strain rate of  $0.05 \text{ s}^{-1}$ , deviation was found to occur. The reason for the deviation is mainly

because of the softening behavior and the drop in flow stress that happens in the early stages at the following deformation temperatures: 923 K (at  $0.05 \text{ s}^{-1} \sim 1.0 \text{ s}^{-1}$ ), 1123 K (at  $0.05 \text{ s}^{-1}$ ) and 1223 K (at  $0.05 \text{ s}^{-1}$ ). The decreased flow stress values led to the improper estimation of the model parameters, because the JC model is just a phenomenological model that does not consider any of the material physical aspects. In addition, sometimes numerical numbers such as  $R^2$  can lead to error, even though the model is adequate numerically. So, in order to remove this misinterpretation, graphical validation is necessary, and if both numerical and graphical outputs are admissible, then the developed flow stress model is good to use for future the calculations.

## 2.6 Conclusions

Numerous isothermal hot tensile tests at elevated temperatures (650–950 °C) and strain rates ( $0.05\text{--}1.0 \text{ s}^{-1}$ ) were carried out to identify the Johnson-Cook material model parameters for AISI 1045 medium carbon steel. The nonlinear programming solver fmincon-based optimization procedure was employed for minimizing the prediction error between the experiments and the predictions to improve the ability of the proposed JC constitutive model. Overall, the results obtained from the optimized JC model showed better agreement with the experimental observations than those of the traditional method. However, more computational time is required to achieve the JC material constants while performing the optimization procedures than with the conventional method. Besides, the developed model predictability was evaluated in terms of the metrics  $R^2$  and AARE. In addition, using the commercial tool, the numerical simulations were modeled extensively in order to develop the damage model using the experimental observations obtained from the quasi-static

tensile tests with smooth and notched specimens at room temperature. The numerical results displayed a good agreement with the corresponding experimental data. From the discussion, it was found that the JC material model requires less effort to predict the model parameters and, on the contrary, the JC damage model requires numerous experimental data to find the model parameters, which necessitates extensive time and cost efforts. Besides, the prediction error between the experimental and predicted data ensures that the proposed constitutive model is credible at elevated temperatures and higher strain rates. Based on these research outcomes, the detailed identification of the JC material and damage model can be devised using the procedure presented here to predict material ductile fracture behavior.

## Chapter 3

# Modified Johnson-Cook and Zerilli-Armstrong Models

### 3.1 Summary

The tensile deformation behavior of AISI-1045 steel material is investigated at deformation temperatures (923 – 1223 K) and strain rates ( $0.05 - 1.0 \text{ s}^{-1}$ ). This chapter proposes a detailed research to characterize the material flow behavior based on modified JC and ZA models, respectively, as well as the predictability of these two models are discussed. The experimental flow stress-strain data are employed to fit the constitutive equations to estimate the elected model material parameters. To demonstrate the validity and the accuracy of the proposed models, the model adequacies such as coefficient of determination and average absolute relative error are discussed. From the observation made, the authors found that the modified ZA model is more appropriate for predicting the material behavior as the predicted flow stress data and the experimental data displayed better correlation among them. To make this point more concrete, random experiments are conducted to validate the proposed constitutive models and the obtained results also show that the developed modified ZA model exhibits a better relationship with the experimental data.



## 3.2 Introduction

The flow stress models such as physically-based and empirical models can provide more accurate representation of the material deformation behavior over a wide range of temperatures and strain rates (Lin and Chen, 2011; He et al., 2018a; Lin et al., 2018; Chen et al., 2017; Jiang et al., 2018). However, each model has its own disadvantages, for example, physically-based models often require more experimental data and high computational time for the material constants estimation. But, the empirical model, JC, can be modified to increase the predictability of the proposed model as well as the model can be incorporated into readily available commercial finite element software, where ZA model has a ability to consider the coupled effect of strain rate and temperature to predict the deformation behavior. Recently, it is proved that the artificial neural network model is capable of solving highly non-linear problems and also the model has an ability to understand the complex and non-linear relationships of stress, strain, strain rate and deformation temperature (Siamak, 2007). So, developing a proper flow stress model for the design process. is essential to predict the materials deformation behavior at high strain rates and deformation temperatures and as a result, reasonable research has been performed considering various materials (Li et al., 2013a; Zhang et al., 2009; Cai et al., 2015; Maheshwari, 2013; Akbari, Mirzadeh, and Cabrera, 2015; Lin, Chen, and Liu, 2010; Song et al., 2013; Li et al., 2013b).

In the material processing, theoretical constitutive models are generally used to describe the material behavior considering the combined effects of strain hardening, strain rate hardening and thermal softening at different strain rates and deformation temperatures (Wang et al., 2013; Tan et al., 2015; Hou and Wang, 2010; Mirzaie, Mirzadeha, and Cabrerab, 2016). Understanding the behavior of ductile materials is essential for modeling the actual structural behavior in terms of numerical model using finite element(FE) tools. In an alternative way, it is recognized that this is the

foundation of numerical modeling in FE tools to solve the actual thermal-mechanical behavior of the materials accurately. Because an appropriate flow stress model has the capability to mathematically characterize the mechanical properties and their responses for wide range of loading conditions. The reason for employing the constitutive models is that most of the model parameters are determined systematically by fitting the measured flow stress values. Therefore, the developed constitutive models can have the capability to accurately characterize the material flow behavior. Johnson and Cook proposed the JC flow stress model for metals to characterize the ductile material behavior under large deformation conditions (He et al., 2013). However, it is important to note down that the combined effects of strain and strain rate hardening and thermal softening are independent of each other, which means the coupled effects are not accounted, in the original JC model. Due to the aforementioned issue, there was a possibility of losing the prediction accuracy of material flow stress values, which acquired from the original JC model (Li et al., 2013c).

This present work aims to evaluate and formulate the flow behavior of AISI-1045 steel at elevated temperatures by conducting isothermal uniaxial tensile experiments over a practical range of deformation temperatures (923 – 1223 K) and strain rates ( $0.05 - 1.0 \text{ s}^{-1}$ ). For this purpose, based on the literature survey, the two flow stress models such as the modified JC and the modified ZA models are chosen. As well as the comparative study on the selected models are conducted in order to discuss their capability to predict the material flow behavior accurately. The advantage of the proposed modified JC and the modified ZA models is that it can be successfully incorporated into several FE tools to characterize the material deformation behavior. Finally, the proposed model adequacies are evaluated statistically by comparing the values of  $R^2$ , the AARE that determined from the measured and the estimated observations.

### 3.3 Modified Johnson-Cook model

The modified JC model can be represented as follows (Wang et al., 2013; Tan et al., 2015; Hou and Wang, 2010):

$$\sigma = (A_1 + B_1\varepsilon + B_2\varepsilon^2)(1 + C_1 \ln\dot{\varepsilon}^*)\exp[(\lambda_1 + \lambda_2 \ln\dot{\varepsilon}^*)T^*], \quad (3.1)$$

$$\dot{\varepsilon}^* = \frac{\dot{\varepsilon}}{\dot{\varepsilon}_{\text{ref}}} \quad \text{and} \quad T^* = T - T_{\text{ref}},$$

where  $\sigma$  is the equivalent flow stress,  $\varepsilon$  and  $\dot{\varepsilon}$  are the equivalent plastic strain and strain rate, respectively.  $\dot{\varepsilon}_{\text{ref}}$  is the reference strain rate, in this present work, it is defined as  $1.0\text{s}^{-1}$  according to the experimental data.  $T$  and  $T_{\text{ref}}$  are the current working temperature and reference temperature, in this present study, it is taken as 1223 K, respectively.  $A_1$ ,  $B_1$ ,  $B_2$ ,  $C_1$ ,  $\lambda_1$  and  $\lambda_2$  are the model material constants. In the modified JC model, the coupled effects of work hardening, strain rate hardening and thermal softening are considered.

#### 3.3.1 Determination of constants $A_1$ , $B_1$ , $B_2$

The model constants such as  $A_1$ ,  $B_1$  and  $B_2$  are fitted by the flow stress data at the reference temperature, 1223 K, and the reference strain rate condition,  $1.0\text{s}^{-1}$ . Under reference conditions, the modified JC model, Eq. (3.1), can be expressed as:

$$\sigma = (A_1 + B_1\varepsilon + B_2\varepsilon^2), \quad (3.2)$$

As displayed in Figure 3.1, the strain hardening exhibits nonlinear relationship with increasing strain values. By substituting the corresponding flow stress data into Eq. (3.2), the material parameters such as  $A_1$ ,  $B_1$  and  $B_2$ , can be estimated from the second order polynomial equation coefficients considering only main effects of strain.

The material constants,  $A_1$ ,  $B_1$  and  $B_2$  are determined as 64.36 MPa, 499.9 MPa and  $-940.3$  MPa, respectively, from the coefficients of fitted polynomial equation.

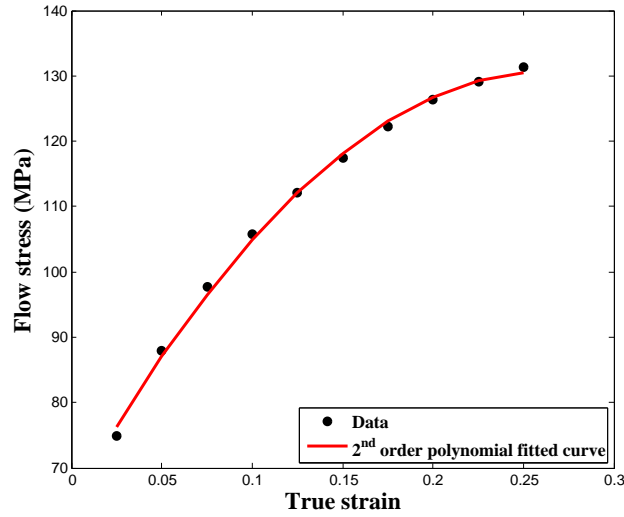


FIGURE 3.1: Relationship between  $\sigma$  and  $\epsilon$  at reference conditions.

### 3.3.2 Determination of constant $C_1$

Using the reference deformation temperature condition, 1223 K, and neglecting the influence of thermal softening effect, Eq. (3.1), can be rewritten as:

$$\sigma = (A_1 + B_1\epsilon + B_2\epsilon^2)(1 + C_1 \ln\dot{\epsilon}^*)$$

$$\frac{\sigma}{(A_1 + B_1\epsilon + B_2\epsilon^2)} = (1 + C_1 \ln\dot{\epsilon}^*)$$

The relationship between stress,  $\frac{\sigma}{(A_1 + B_1\epsilon + B_2\epsilon^2)}$ , and the dimensionless strain rate,  $\ln\dot{\epsilon}^*$ , at the reference temperature, 1223 K, can be obtained by substituting the selected experimental flow stress data at the ten discrete strain values between 0.025 and 0.25. Then the model parameter value,  $C_1$ , is determined as 0.1061 from the slope of the fitted polynomial curve as shown in Figure 3.2.

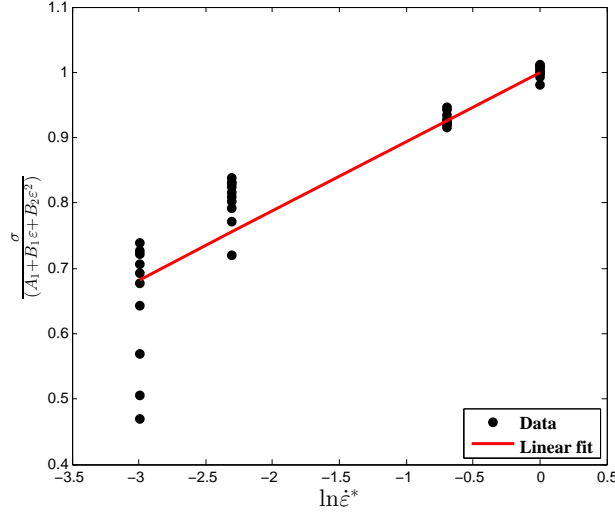


FIGURE 3.2: Relationship between  $\sigma / (A_1 + B_1 \varepsilon + B_2 \varepsilon^2)$  and  $\ln \dot{\varepsilon}^*$ .

### 3.3.3 Determination of constants $\lambda_1, \lambda_2$

For different deformation temperatures and strain rates, Eq. (3.1) can be rearranged as follows:

$$\frac{\sigma}{(A_1 + B_1 \varepsilon + B_2 \varepsilon^2)(1 + C_1 \ln \dot{\varepsilon}^*)} = \exp[(\lambda_1 + \lambda_2 \ln \dot{\varepsilon}^*)T^*] \quad (3.3)$$

Taking natural logarithm of Eq. (3.3), we can obtain the following equation:

$$\ln \left\{ \frac{\sigma}{(A_1 + B_1 \varepsilon + B_2 \varepsilon^2)(1 + C_1 \ln \dot{\varepsilon}^*)} \right\} = (\lambda_1 + \lambda_2 \ln \dot{\varepsilon}^*)T^* \quad (3.4)$$

In order to simplify Eq. (3.4), we are introducing the parameter,  $\lambda$ , is equal to  $(\lambda_1 + \lambda_2 \ln \dot{\varepsilon}^*)$ , and the new parameter can be gained from the relationship between  $\ln \left\{ \frac{\sigma}{(A_1 + B_1 \varepsilon + B_2 \varepsilon^2)(1 + C_1 \ln \dot{\varepsilon}^*)} \right\}$  and  $T^*$ . In this present derivation, we have four different strain rates, so the four different values of  $\lambda$  can be achieved from the slope of the linear fitting curves as displayed in Figure 3.4.

$$\lambda = \lambda_1 + \lambda_2 \ln \dot{\varepsilon}^*$$

Subsequently, the material model parameters,  $\lambda_1$  and  $\lambda_2$  can be achieved from the intercept and the slope of the linear relationship between the new parameter,  $\lambda$ , and the dimensionless strain rate,  $\ln\dot{\epsilon}$ , as shown in Figure 3.3. From the fitted curve, the material constants,  $\lambda_1$  and  $\lambda_2$  are determined as  $-0.00359$ ,  $8.73 \times 10^{-5}$ , respectively. Thus, the predicted constitutive equation of the modified JC model is established according to the estimated material constants as follows:

$$\hat{\sigma}_{\text{pred}} = (64.36 + 499.9\epsilon - 940.3\epsilon^2) \left( 1 + 0.1061 \ln \left( \frac{\dot{\epsilon}}{1.0} \right) \right) \exp \left[ \left( -0.00359 + 8.73 \times 10^{-5} \ln \left( \frac{\dot{\epsilon}}{1.0} \right) \right) (T - 1223) \right].$$

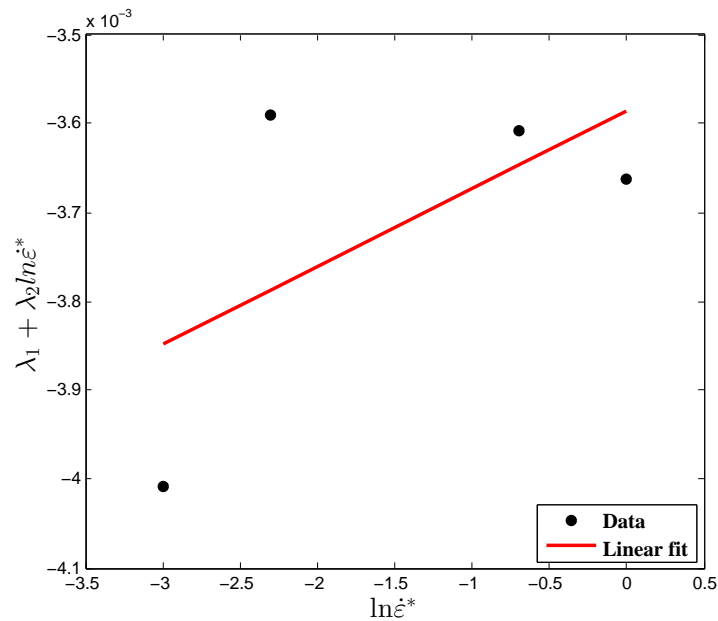


FIGURE 3.3: Relationship between  $\lambda$  and  $\ln\dot{\epsilon}$ .

### 3.4 Modified Zerilli-Armstrong Model

The modified ZA model for predicting the material flow behavior can be expressed as (Zhang et al., 2009; Mirzaie, Mirzadeha, and Cabrerab, 2016; Zhan et al., 2014;

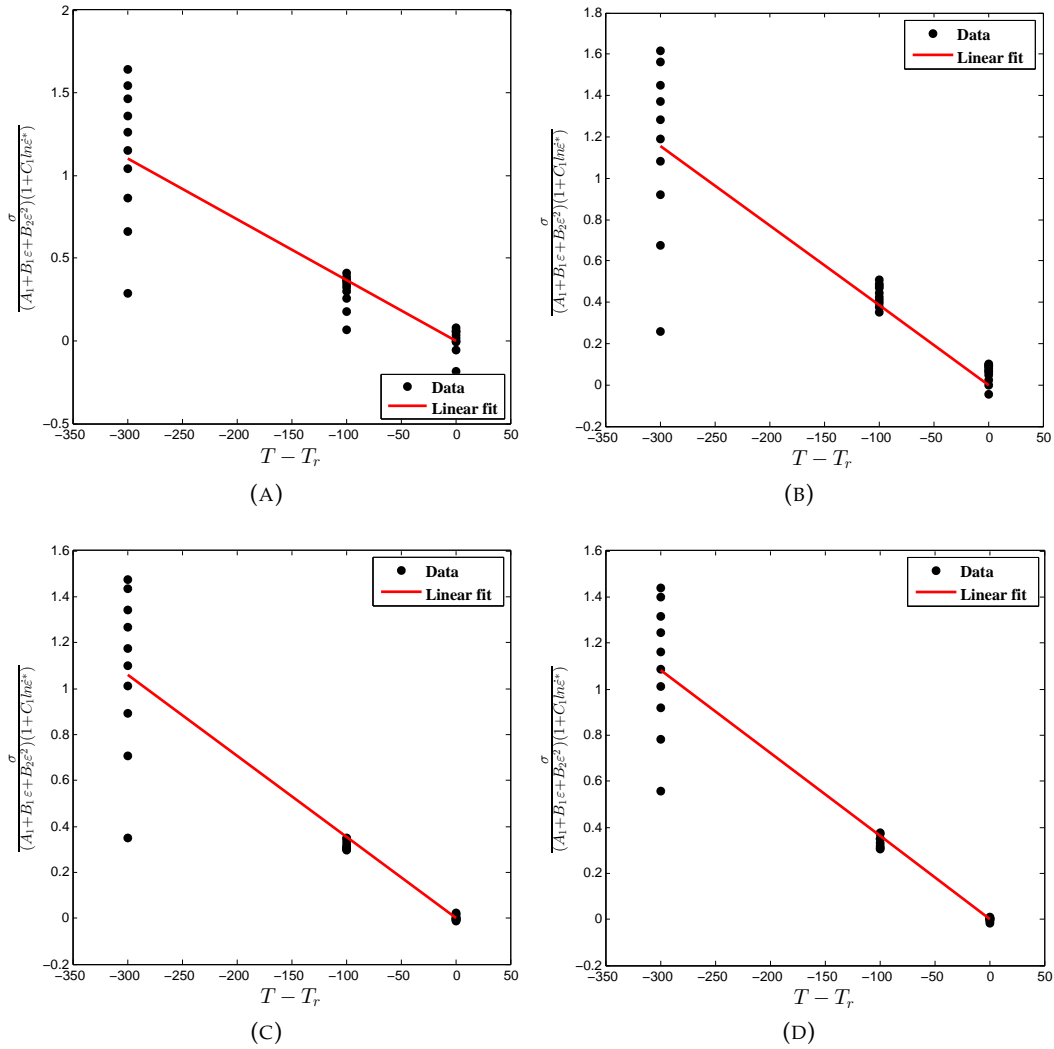


FIGURE 3.4:  $\ln \left\{ \sigma / (A_1 + B_1 \epsilon + B_2 \epsilon^2)(1 + C_1 \ln \dot{\epsilon}^*) \right\}$  and  $T^*$ . (a)  $\dot{\epsilon} = 0.05 \text{ s}^{-1}$ ; (b)  $\dot{\epsilon} = 0.1 \text{ s}^{-1}$ ; (c)  $\dot{\epsilon} = 0.5 \text{ s}^{-1}$ ; (d)  $\dot{\epsilon} = 1.0 \text{ s}^{-1}$ .

Samantaray, Mandal, and Bhaduri, 2009):

$$\sigma = (C_1 + C_2 \epsilon^n) \exp[-(C_3 + C_4 \epsilon) T^* + (C_5 + C_6 T^*) \ln \dot{\epsilon}^*], \quad (3.5)$$

$$\dot{\epsilon}^* = \frac{\dot{\epsilon}}{\dot{\epsilon}_{\text{ref}}}$$

$$T^* = T - T_{\text{ref}}$$



where  $\sigma$  is the equivalent flow stress,  $\varepsilon$ ,  $\dot{\varepsilon}$  and  $\dot{\varepsilon}_{\text{ref}}$  are the equivalent plastic strain, the strain rate and the reference strain rate, respectively.  $T$  and  $T_{\text{ref}}$  are, respectively, the current working temperature and reference temperature. In Eq. (3.5),  $C_1$ ,  $C_2$ ,  $n$ ,  $C_3$ ,  $C_4$ ,  $C_5$  and  $C_6$  are the material parameters. The step by step procedures to estimate the material model parameters are illustrated and explained below. Here, the material constant,  $C_1$ , is determined as 74.843 MPa from the yield stress of stress-strain data at the reference deformation temperature and strain rate conditions.

#### 3.4.1 Determination of constants $C_2$ and $n$

At the reference strain rate,  $1.0 \text{ s}^{-1}$ , Eq. (3.5) can be rearranged into Eq. (3.6) as follows:

$$\sigma = (C_1 + C_2\varepsilon^n)\exp[-(C_3 + C_4\varepsilon)T^*], \quad (3.6)$$

Then taking the natural logarithm of Eq. (3.6), we can obtain the following equation:

$$\ln\sigma = \ln(C_1 + C_2\varepsilon^n) - (C_3 + C_4\varepsilon)T^*,$$

$$I_1 = \ln(C_1 + C_2\varepsilon^n), \quad (3.7)$$

$$s_1 = -C_3 + C_4\varepsilon, \quad (3.8)$$

By substituting the associated flow stress-strain data from the experiment at the reference strain rate,  $1.0 \text{ s}^{-1}$ , the values of  $S_1$  and  $I_1$  can be determined from the slope and the intercept of the linear fitted curve between  $\ln\sigma$  and  $T^*$  as shown in Figure 3.5. The calculation procedure for determining the values of  $S_1$  and  $I_1$  is repeated for the strain values between 0.05 and 0.25 at the interval of 0.025 and eventually, the ten sets of  $S_1$  and  $I_1$  are determined from the linear curve fitting.

Further, Eq. (3.9) is gained by taking the natural logarithm of Eq. (3.7) as follows:

$$\ln(\exp(I_1) - C_1) = \ln C_2 + n \ln \varepsilon \quad (3.9)$$

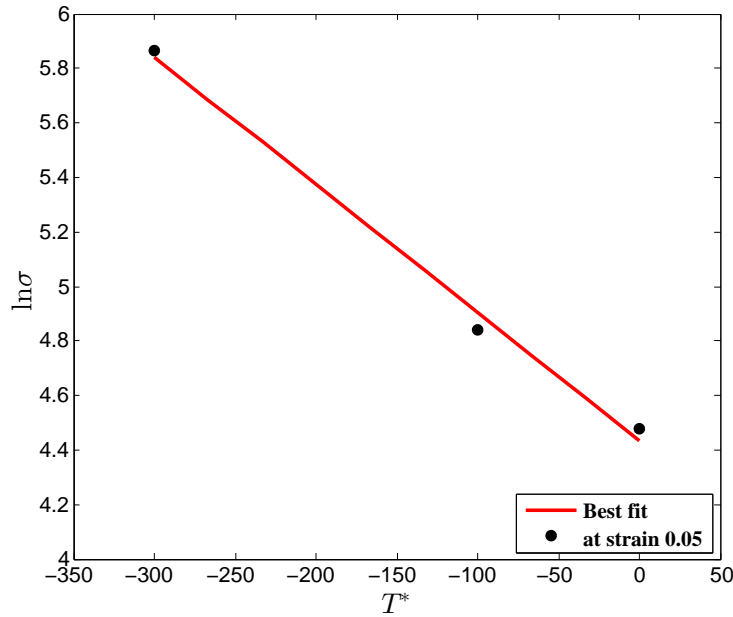


FIGURE 3.5: Relationship between  $\ln \sigma$  and  $T^*$ .

At reference strain rate,  $1.0 \text{ s}^{-1}$ , considering entire deformation temperatures, substituting the values of  $C_1$  and  $I_1$ , the linear relationship between  $\ln(\exp(I_1) - C_1)$  and  $\ln \varepsilon$  can be gained as illustrated in Figure 3.6. Thus, the material model parameters,  $C_2$  and  $n$  are estimated as 387.998 MPa and 1.218 from the slope and the intercept of the fitted constitutive equation.

### 3.4.2 Determination of constants $C_3$ and $C_4$

In a similar way as we calculated the material constants,  $C_2$  and  $n$ , at reference strain rate,  $1.0 \text{ s}^{-1}$ , substituting associated  $S_1$  values to the discrete strain values, the material constants,  $C_3$  and  $C_4$ , Eq. (3.8), are obtained as 0.005 421 and  $-0.0128$ ,

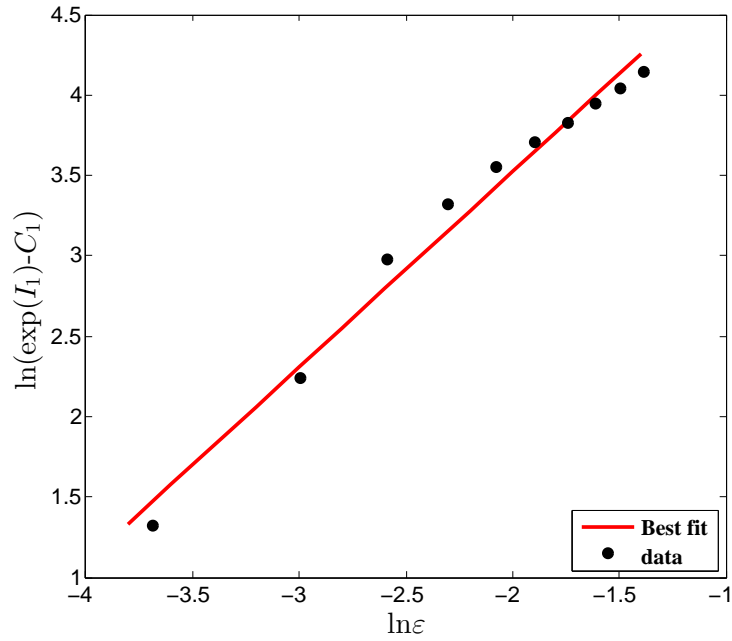


FIGURE 3.6: Relationship between  $\ln(\exp(I_1) - C_1)$  and  $\ln \epsilon$ .

respectively, from the slope and the intercept of the linear relationship between  $\epsilon$  and  $S_1$  as shown in Figure 3.7.

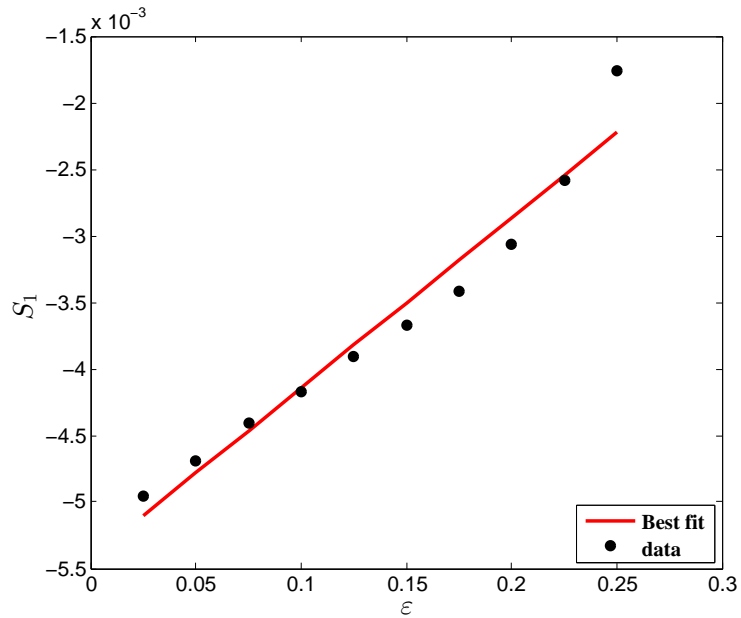


FIGURE 3.7: Relationship between  $S_1$  and  $\epsilon$ .

### 3.4.3 Determination of constants $C_5$ and $C_6$

Taking the natural logarithm of Eq. (3.5), Eq. (3.10) can be derived as expressed below:

$$\ln\sigma = \ln(C_1 + C_2\varepsilon^n) - (C_3 + C_4\varepsilon)T^* + (C_5 + C_6T^*)\ln\dot{\varepsilon}^*, \quad (3.10)$$

$$S_2 = C_5 + C_6T^* \quad (3.11)$$

For three deformation temperatures (923 K, 1123 K, 1223 K), the relationship between  $\ln\sigma$  and  $\ln\dot{\varepsilon}^*$  can be achieved as shown in Figure 3.8. Subsequently, the value of  $S_2$  are obtained from the slope of the fitted curve, Figure 3.8, at a specific strain value. For three different temperatures, three different values of  $S_2$  are obtained at one specified strain, for example  $\varepsilon=0.175$ , and repeat the same procedure for other nine strain values. Thereafter, the material constants,  $C_5$  and  $C_6$ , Eq. (3.11), can be captured from the slope and the intercept of the fitted curve between  $T^*$  and  $S_2$  as depicted in Figure 3.10.

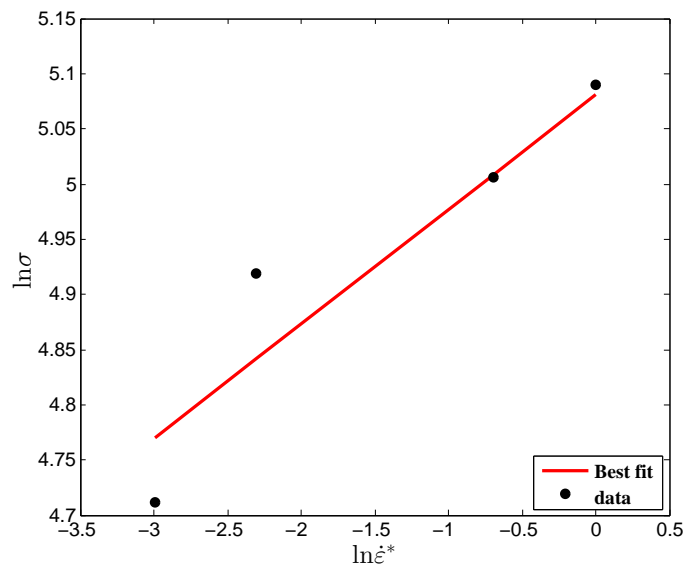


FIGURE 3.8: Relationship between  $\ln\sigma$  and  $\ln\dot{\varepsilon}^*$  at  $\varepsilon=0.15$  and  $T=1123$  K.

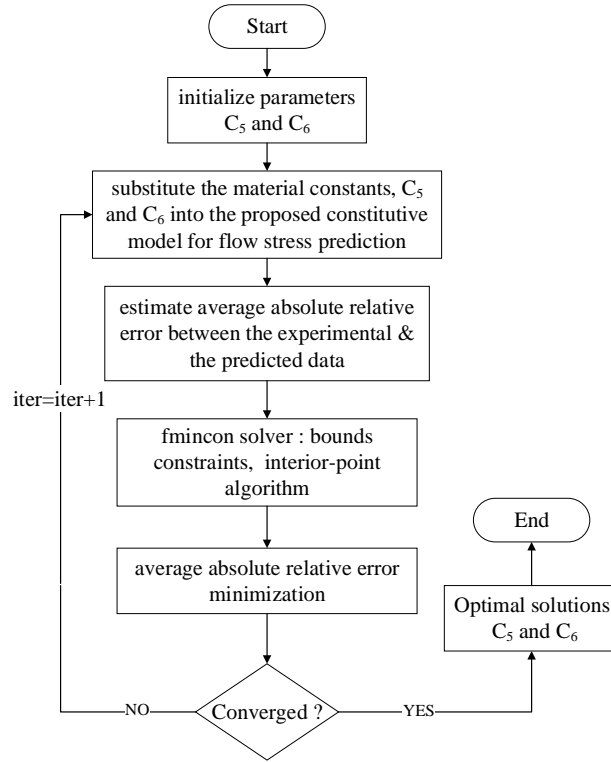


FIGURE 3.9: Flow chart of optimization procedure.

Ten sets of material constants such as  $C_5$  and  $C_6$  are determined at different true strains. A bounds constrained optimization procedure (Figure 3.9) is employed to find the optimum solution of the material constants,  $C_5$ ,  $C_6$  and the optimization formulation employed in this present work is expressed below:

$$\left\{ \begin{array}{l}
 \text{Minimize:} \\
 \quad x \\
 \quad \text{AARE} = \frac{1}{n} \sum_{i=1}^n \left| \frac{\sigma_{\text{exp}}^i - \sigma_{\text{pred}}^i}{\sigma_{\text{exp}}^i} \right| \times 100\%, \\
 \quad \text{where, } \sigma_{\text{pred}} = (C_1 + C_2 \varepsilon^n) \exp[-(C_3 + C_4 \varepsilon) T^* + (x(1) + x(2) T^*) \ln \varepsilon^*] \\
 \text{subjected to} \quad \left\{ \begin{array}{l}
 C_{5\text{min}} \leq x(1) \leq C_{5\text{max}} \\
 C_{6\text{min}} \leq x(2) \leq C_{6\text{max}}
 \end{array} \right.
 \end{array} \right.$$

For this purpose, the nonlinear programming solver, `fmincon`, is used with the IP algorithm to minimize the prediction error between measured and estimated flow stress data. For this optimization problem, the IP algorithm is used because the goal is to find the minimum of an objective function in the presence of only bounds constraints. The obtained results showed that the minimum prediction error can be achieved as 9.91%, when the material constants,  $C_5$  and  $C_6$ , are 0.1246 and 0.0001, respectively. The estimated model constants of the modified ZA model are summarized in Table 3.1.

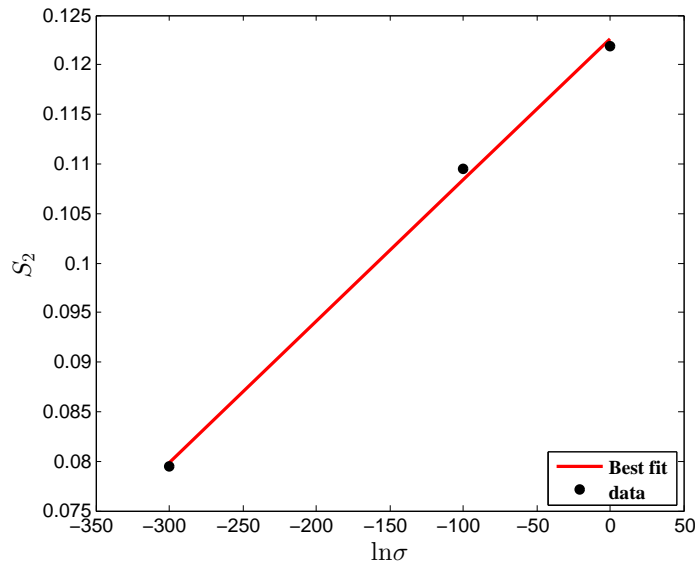


FIGURE 3.10: Relationship between  $S_2$  and  $\ln \sigma$  at  $\epsilon=0.175$ .

### 3.5 Discussion

The flow stress values for the deformation temperatures, (923 – 1223 K), and the strain rates, (0.05 – 1.0 s<sup>-1</sup>), are calculated with the help of computed material constants of the modified JC and the modified ZA models. Thereafter, the estimated flow stress values are compared with the measured flow stress values to check the predictability of the proposed flow stress models as displayed in Figs. 3.11 and 3.12.

TABLE 3.1: Parameters of AISI-1045 steel for the modified ZA model.

Parameter	$C_1$ (MPa)	$C_2$ (MPa)	$n$	$C_3$	$C_4$	$C_5$	$C_6$
Value	74.843	387.998	1.218	0.005421	-0.0128	0.1246	0.0001

To perform the model validation, two standard statistical measurements are used. The first metric:  $R^2$ , a statistical measure, is employed to explain the strength of linear relationship between the two variables, in this work, the two variables are the measured and the estimated observations. It is represented as a value between zero and one. If the estimated statistical measure is close to one, the model explains the better predictability between the two variables or vice versa. The model can be expressed as follows (Kyunghoon et al., 2017; Mohanraj, Beom-Soo, and Kyunghoon, 2015):

$$R^2 = 1 - \frac{\sum_{i=1}^n (\sigma_{\text{exp}}^i - \hat{\sigma}_{\text{pred}}^i)^2}{\sum_{i=1}^n (\sigma_{\text{exp}}^i - \bar{\sigma}_{\text{exp}})^2},$$

where  $\sigma_{\text{exp}}$ ,  $\sigma_{\text{pred}}$ ,  $\hat{\sigma}$  and  $n$  the experimental flow stress, the predicted flow stress, the mean values of the experimental flow stress and the total number of data points, respectively. The second metric: AARE is utilized for measuring the predictability of the flow stress model through term by term comparison of the relative error (Kyunghoon et al., 2017; Mohanraj, Beom-Soo, and Kyunghoon, 2015; Murugesan and Jung, 2019a).

$$\text{AARE} = \frac{1}{n} \sum_{i=1}^n \left| \frac{\sigma_{\text{exp}}^i - \sigma_{\text{pred}}^i}{\sigma_{\text{exp}}^i} \right| \times 100\%,$$

where  $\sigma_{\text{exp}}$ ,  $\sigma_{\text{pred}}$ ,  $\hat{\sigma}$  and  $n$  the experimental flow stress, the estimated flow stress, the mean value of measured data and the total number of data points, respectively. In this research, each test conditions are investigated by estimating the values of  $R^2$  and AARE value for each case than the conventional method, in which the entire



data set used to compute the statistical parameters as mentioned in Tables. 3.2 and 3.3. In this way, the prediction strength of the proposed JC model can be discussed in detail. From Figs. 3.11 and 3.12, overall, it is identified that the modified ZA model displayed a better relationship with the measured data in most of the test conditions than the modified JC model. This statement again proved using the numerical values which outlined in Tables. 3.2 and 3.3.

TABLE 3.2: Statistical measurements of modified JC model.

Conditions	$R^2$	overall- $R^2$	AARE (%)	overall-AARE (%)
923 K	0.0062		31.7267	
1123 K	0.9009	0.7096	6.0907	14.391
1223 K	0.8901		5.3562	

TABLE 3.3: Statistical measurements of modified ZA model.

Conditions	$R^2$	overall- $R^2$	AARE (%)	overall-AARE (%)
923 K	0.6804		13.0424	
1123 K	0.8454	0.9364	6.8803	9.9141
1223 K	0.7706		9.8195	

In Figure 3.11a, the predicted flow curves and experimental flow curves show the large deviation at the deformation temperature, 923 K, for the entire set of strain rates. Using the flow stress-strain data, the relationship plot is obtained as depicted in Figure 3.11d. From Figure 3.11d, it has been noticed that the deviation of flow stress values, at the right top corner, is found to have a flower pattern behavior. This flower pattern explains that the modified JC model constants are having a negative influence on the tracking the flow behavior accurately. Furthermore, it is important to mention here that the main reason for having this prediction error owing to the plastic instability occurred during the tensile test. In addition, the same prediction error is evident from Figs. 3.11b and 3.11c for the deformation temperatures, 1123 K and 1223 K, at strain rate,  $0.05 \text{ s}^{-1}$ , for the tested conditions, and this leads to the

highest prediction error as listed in Table 3.2. However, it is evident that the modified JC model can represent the material flow behavior more accurately at the elevated temperatures (1123 K and 1223 K) and lower strain rates ( $0.05 \text{ s}^{-1}$  and  $0.1 \text{ s}^{-1}$ ) as shown in Figs. 3.11b and 3.11c. In addition, the estimated statistical measures, AARE, and  $R^2$ , as outlined in Table 3.2, are utilized to demonstrate the proposed model prediction accuracy in terms of each tested conditions. As a result, the calculated values of statistical measures implies that the modified JC model is not an accurate model to perfectly describe the material flow behavior at the lower temperatures and the higher strain rates. However, the deviations are quite acceptable in the higher strain rates as it depicts the reasonable overall metrics in Table 3.2.

TABLE 3.4: Statistical parameters estimation from random experiments at deformation temperature 1023 K.

Conditions	Models	$R^2$	AARE (%)
$0.05 \text{ s}^{-1}$	modified JC model	0.8681	9.61
$1.0 \text{ s}^{-1}$		0.6743	
$0.05 \text{ s}^{-1}$	modified ZA model	0.8778	4.39
$1.0 \text{ s}^{-1}$		0.7656	

Likewise, using the modified ZA model parameters summarized in Table 3.1, the flow stress values are predicted for the various experimental conditions. From Figs. 3.12b and 3.12c, at deformation temperatures, 1123 K and 1223 K, most of the flow stress data fall very close to the experimental data where as the considerable deviation is noticed in Figure 3.12a for the deformation temperature, 923 K. Consequently, the correlation plot obtained from the developed flow stress model is depicted in Figure 3.12d and corresponding value of the statistical parameters,  $R^2$ , and AARE are estimated as 0.936 and 9.914%, respectively. Figure 3.12d and the numerical values are evident that a good correlation between measured and estimated flow stress-strain data is obtained for an entire processing conditions. Further, the AARE of the modified ZA model, 9.914%, is smaller than the modified JC model,

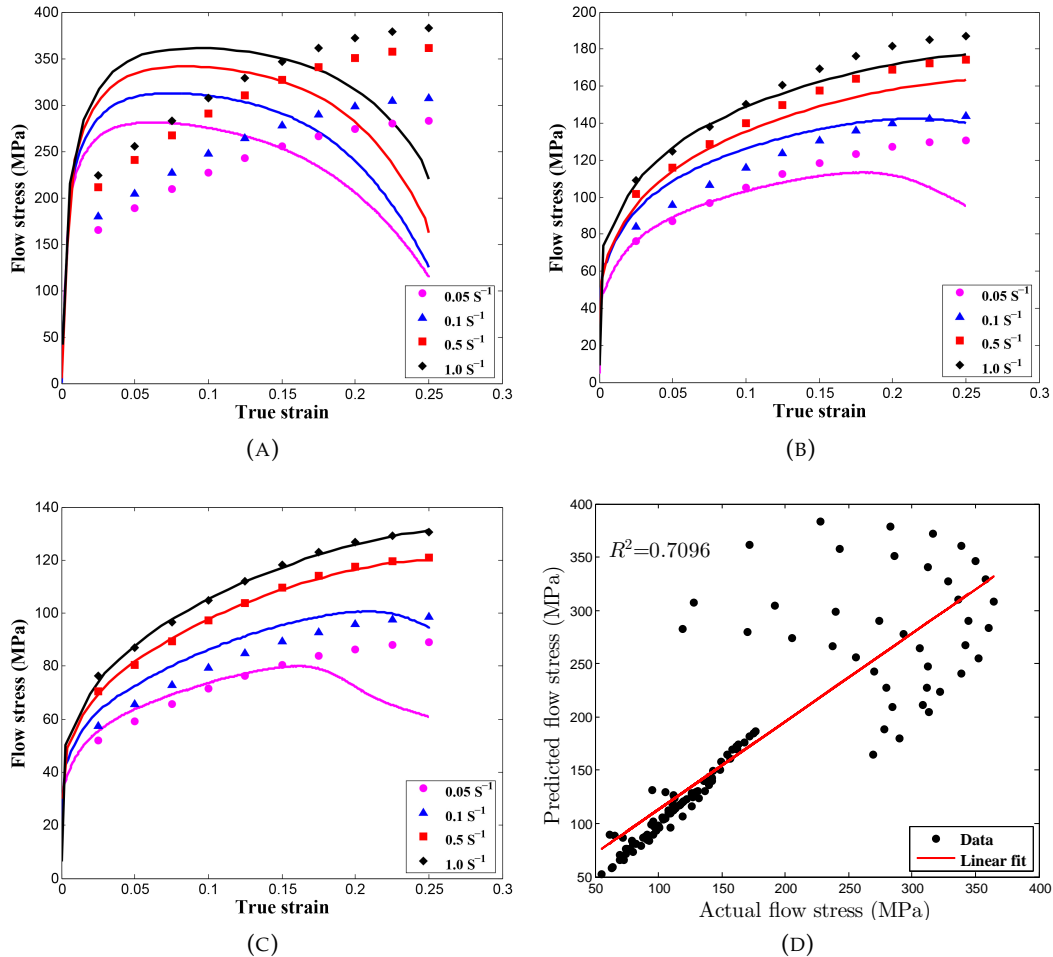


FIGURE 3.11: Comparison plot using modified JC model. (a) 923 K ; (b) 1123 K ; (c) 1223 K ; (d) correlation plot.

14.391%, and this shows that the modified ZA model have considerable capability to predict the flow behavior throughout the entire deformation temperature and strain rate conditions. In addition, the random experiments are conducted at deformation temperature, 1023 K under strain rates of 0.05 s<sup>-1</sup> and 1.0 s<sup>-1</sup> to verify the proposed models adequacies. The computed model parameters, Table 3.4, of the modified JC and the modified ZA models are indicates that the modified ZA can predict the material behavior more accurately than modified JC model as the AARE of the modified ZA model, 4.39%, is smaller than the modified JC model, 9.61%.

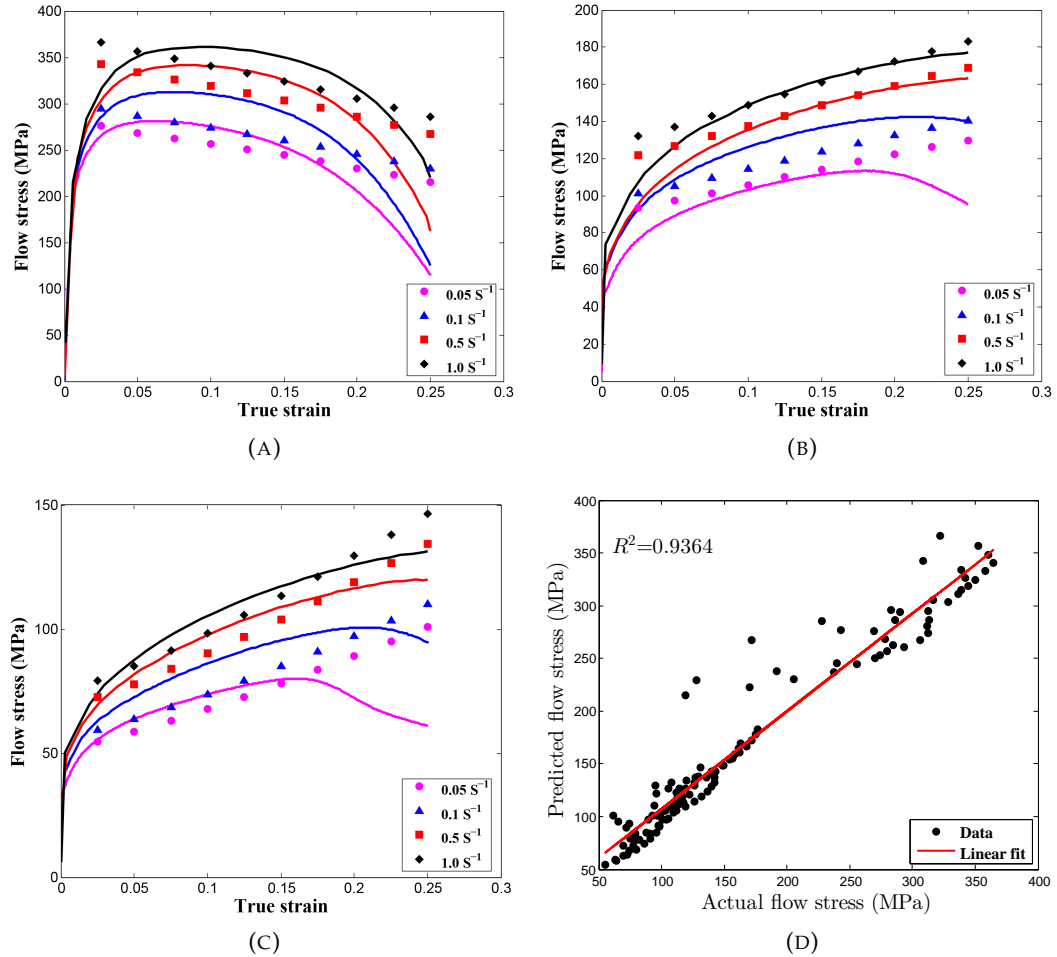


FIGURE 3.12: Comparison plot using modified ZA model. (a) 923 K ; (b) 1123 K ; (c) 1223 K ; (d) correlation plot.

$$\text{Error} = \frac{|(9.9141 - 14.391)|}{9.9141} \times 100 = 45.15\%, \quad (3.12)$$

Overall, it can be easily concluded, from the comparison depicted in Figs. 3.11 and 3.12 and the numerical values summarized in Tables. 3.2 and 3.3, that the modified ZA model is comparatively more prominent and shows better agreement between measured and estimated data than the modified JC model at the entire processing conditions. In addition, the modified ZA model involves seven material

constants, which is almost close to the number of model constants involved in the modified JC model. But, the computational time required for computing the material constants of the modified ZA model is little bit longer than the other model, because the computation of material constants,  $C_5$  and  $C_6$  takes a few steps of optimization procedures. Furthermore, the model prediction error percentage, Eq. (3.12), between the modified JC model and ZA model is determined as 45.15%. The error percentage proves that the little longer computational time results in better outcome of flow stress prediction.

### 3.6 Conclusions

Two flow stress models have been proposed to verify the predictability of the modified JC and the modified ZA models to represent the material flow behavior of AISI-1045 steel in a wide range of deformation temperatures (923 – 1223 K) and strain rates ( $0.05 - 1.0 \text{ s}^{-1}$ ). The precise experiment is carried out using two different sets of specimens, and the true stress-strain data for the material model parameters estimation are computed from the averaged flow stress data. The modified JC model is lacking ability to provide a good tracking of material flow behavior of AISI-1045 steel at the higher strain rates and lower temperatures. The main reason of this inadequacy is due to the improper estimation of exponent term, thermal softening, in the modified JC constitutive equation. The modified ZA model is adequate as the predictions are well agreed with the experimental data and indicates the acceptable statistical measures, in terms of average absolute relative error and the coefficient of determination. But, this model needs more computational time to estimate the material parameters, even though the number of materials are quite same with the modified JC model. However, the modified ZA model could predict the deformation behavior much more accurately than the modified JC model. Random experiments

are performed to verify the predictability of the proposed flow stress models, and it can be used to identify and eliminate the experimental error such as noise, change in environmental conditions and voltage fluctuations. The detailed step by step procedures for computing the material model parameters are presented here, and this proposed model can be utilized to develop the numerical model to replicate the real system behavior.

## Chapter 4

# Arrhenius-Type Constitutive and Artificial Neural Network Models

### 4.1 Summary

In this chapter, the Arrhenius-type constitutive equation and the artificial neural network (ANN) model with a back-propagation (BP) algorithm are used to formulate the flow stress models. Besides, the Zener-Hollomon parameter is altered, employing incorporating the effect of strain rate and strain on the flow stress. The empirical model approach is employed to estimate the material model constants from the constitutive equation. Besides, for the ANN-BP model training and testing purpose, the test data are normalized to effectively run the model; after solving, the obtained results are again converted to achieve the actual data. The population metrics such as  $R^2$ , and AARE is employed to confirm the model predictability. The computed results are discussed using numerical and graphical verification's. From the constitutive equation graphical comparison, the flow stress-strain data achieved from the proposed constitutive model are in good agreement with the actual data. The model accuracy is found to be improved as the prediction error range from 3.678% to 2.984%. Besides, from the ANN-BP model predicted results, the  $R^2$  and the AARE are determined as 0.999 and 1.335%, respectively. For improving the model

predictability, the constrained nonlinear function based optimization procedures is adopted to obtain the best candidate selections of weights and biases. By evaluating each test conditions, it is found that the average absolute relative error based on the optimized ANN-BP model varied from 0.728% to 1.775%. Overall, the trained ANN-BP models are proved to be much more efficient and accurate by means of flow stress prediction against the experimental data for all the tested conditions. These results outcome proves that an ANN-BP model is more accurate for the flow stress prediction than that of the conventional flow stress models.

## 4.2 Introduction

During the metal forming process, metals and alloys undergo an inhomogeneous deformation by cause of hot operating conditions. For this reason, understanding the metals deformation behavior is necessary for determining the working parameters that affect the mechanical properties for providing the well-defined material processing data to the industry (Li et al., 2018; Li et al., 2016; Liang and Zhang, 2018; Lei et al., 2019). The constitutive equations are often utilized in a form that is suitable to use in FE commercial tools. They used to represent the material flow behavior and helps to obtain a better prediction (Cai et al., 2011; Slooff et al., 2007; Bobbili, Madhu, and Gogia, 2016; GAN et al., 2014). Moreover, the constitutive equations are categorized as follows: physical, phenomenological, and statistical models (MA et al., 2011; Ren and Chen, 2013; Chai, Guo, and Yu, 2012; Rokni et al., 2014). In our previous work (Murugesan and Jung, 2019a; Murugesan and Jung, 2019b), a detailed discussion on AISI 1045 steel material behavior in hot processing conditions was carried out using JC, modified JC, and modified ZA models. The results showed that the modified ZA model was more significant in representing the material deformation behavior compared with the test data than that of others.



However, the flow stress model predictability can be improvised by training other available conventional models. For this purpose, in this present investigation, the strain compensated Arrhenius-type constitutive model was adopted to represent the material's ductility behavior in hot operating conditions. In the past, there has been information published on constitutive equations to consistently describe the material's behavior at various loading conditions Mirzadeh and Najafizadeh, 2010; Yang et al., 2015; Quan et al., 2013; Sun et al., 2011. Besides, many researchers have discussed the advantage of utilizing the constitutive equations by comparing the outcome of available flow stress models, and they reported that the proposed models could be able to precisely characterize the material behavior because the parameters are determined statistically from the experimental data (Abbasi-Bani et al., 2014; He et al., 2013; Han et al., 2013; Li et al., 2016). However, there are only limited reports on the improvement of the strain compensated Arrhenius-type constitutive model, including strain and strain rate effects, into the Zener-Hollomon (Z) parameter to describe the material behavior accurately (Mandal et al., 2009; Krishnan et al., 2011).

In recent years, the ANN model has been employed as the model uses mathematical formulations to construct a brain nervous system operation based on relationships exist between inputs and outputs. Moreover, a countable number of research articles were published with respect to this topic for the application of flow stress prediction (Zhu et al., 2011; GUO, LI, and ZHANG, 2013; Bobbili, Madhu, and Gogia, 2014; Xiao et al., 2012; Li et al., 2012). Ji et al. (Ji et al., 2011) and Peng et al. (Peng et al., 2013) studied about developing constitutive relationship at elevated temperatures and strain rates test conditions using an Arrhenius-type constitutive (AC) and ANN models in Aermet100 steel and as-cast Ti60 titanium alloy materials, respectively. They drew the conclusion that the back-propagation (BP) ANN model can accurately predict the actual data. The flow stress estimation in a wide range of test conditions

associating phase transformations in as-cast Ti-6Al-2Zr-1Mo-1V alloy was investigated by Quan et al. (Quan et al., 2013). They pointed out that the ANN model can forecast material flow behavior including the metallurgical phenomenon, and also stated that the model has a capability to capture complex behavior even outside of the test conditions. Ashtiani et al. (Ashtiani and Shahsavari, 2016) and Stendal et al. (Stendal et al., 2019) employed both phenomenological and ANN models to predict high-temperature deformation behavior in AlCuMgPb alloy and titanium aluminide alloy (TNM-B1) materials. They identified that the well trained ANN model can be able to make accurate predictions than the tested phenomenological equations. Han et al. (Han et al., 2013) proposed a model from an AC and an ANN models for as-cast 904L austenitic stainless steel to predict the material behavior and results proved that the optimized ANN model has ability to capture the compressive behavior at high deformation temperatures. From literature survey, recent studies outcome indicates the importance of ANN model to characterize the material flow behavior at hot working conditions. Although there is rapidly growing literature on an ANN model, there are only limited articles to discuss improving an ANN model accuracy. Huang et al. (Huang, Jia, and Zhang, 2018) proposed a modified ANN-BP based on genetic algorithm (GA) to predict the material behavior in aluminum alloy. They outlined that an ANN-GA model displayed a more efficient and accurate prediction.

Therefore, this present research work aims to establish and devise the suitable flow stress model over a wide range of testing conditions to describe the material flow behavior. The test conditions, such as deformation temperatures and strain rates are 650–950 °C and 0.05–1.0 s<sup>-1</sup>, respectively. For this purpose, the real test measurements were used to fit the model equations by both compensations of strain ( $\epsilon$ ) and strain rate ( $\dot{\epsilon}$ ). Furthermore, the predictability of proposed models was validated against the experimental observations and also discussed statistically by

both numerical and graphical validation.

### 4.3 Strain Compensated Constitutive Equation

#### 4.3.1 Arrhenius-Type Constitutive Equation

The Zener-Holloman  $Z$  parameter can be used to express the influence of strain rate ( $\dot{\epsilon}$ ), and deformation temperature ( $T$ ), on the material plastic deformation as follows (Cai et al., 2011; Kyunghoon et al., 2017):

$$Z = \dot{\epsilon} \exp[Q/(RT)], \quad (4.1)$$

In Equation (4.1), the variables,  $Q$  and  $R$ , are the deformation activation energy and the universal gas constant ( $8.314 \text{ J mol}^{-1} \text{ K}^{-1}$ ), respectively.

At steady-state, the flow stress levels used to select the peak flow stress to estimate  $\alpha\sigma$  values to choose the proper  $Z$  equation. There are three levels of  $Z$  equation as follows (Ren and Chen, 2013; Kyunghoon et al., 2017)

$$Z = \begin{cases} A_1 \sigma^{n_1} & \text{if } \alpha\sigma < 0.8 \\ A_2 \exp(\beta\sigma) & \text{if } \alpha\sigma > 1.2 \\ A[\sinh(\alpha\sigma)]^n & \text{for all } \sigma, \end{cases} \quad (4.2)$$

where  $A_1$ ,  $n_1$ ,  $A_2$ ,  $\beta$ ,  $A$ ,  $n$  and  $\alpha$  are the model constants.  $\alpha$  is the stress multiplier,  $\alpha = \beta/n_1$ . Firstly, by replacing the  $Z$  parameter in Equation (4.2) substituting Equation (4.1), and then performing the log transformations gives (Chai, Guo, and

Yu, 2012; Mirzadeh and Najafizadeh, 2010; Kyunghoon et al., 2017; Ren et al., 2013)

$$\ln \dot{\epsilon} = \ln A_1 + n_1 \ln \sigma - [Q/(RT)], \quad (4.3)$$

$$\ln \dot{\epsilon} = \beta \sigma + \ln A_2 - [Q/(RT)], \quad (4.4)$$

$$\ln \dot{\epsilon} = n \ln[\sinh(\alpha\sigma)] + \ln A - [Q/(RT)]. \quad (4.5)$$

Considering constant deformation temperature,  $T$ , from Equations (4.3)–(4.5), by taking partial derivatives, the material model constants,  $n_1$ ,  $\beta$  and  $n$ , can be estimated as follows (Chai, Guo, and Yu, 2012; Kyunghoon et al., 2017)

$$n_1 = \left. \frac{\partial \ln \dot{\epsilon}}{\partial \ln \sigma} \right|_T, \quad \beta = \left. \frac{\partial \ln \dot{\epsilon}}{\partial \sigma} \right|_T, \quad n = \left. \frac{\partial \ln \dot{\epsilon}}{\partial \ln[\sinh(\alpha\sigma)]} \right|_T.$$

To estimate the model constants,  $\alpha$  and  $n$ , for example, the stress values associated with the plastic strain value of 0.02, was chosen at tested conditions. By substituting the corresponding values to Equations (4.3) and (4.4) and performing the linear regression analysis,  $\beta$ ,  $n_1$ , and  $n$  were determined from the correlation plots of  $\ln \dot{\epsilon}$  and  $\sigma$ ,  $\ln \dot{\epsilon}$  and  $\sigma$  and  $\ln \dot{\epsilon}$  and  $\ln(\sinh(\alpha\sigma))$ , respectively, as illustrated in Figures 4.1a,b and 4.2a.

Similarly, considering a specific strain-rate ( $\dot{\epsilon}$ ), by performing a partial derivative of Equation (4.5), the model parameter,  $Q$ , Equation (4.6), can be estimated as follows (Kyunghoon et al., 2017)

$$Q = nR \left. \frac{\partial \ln[\sinh(\alpha\sigma)]}{\partial(1/T)} \right|_{\dot{\epsilon}}. \quad (4.6)$$

$$\text{slope} = \left. \frac{\partial \ln[\sinh(\alpha\sigma)]}{\partial(1/T)} \right|_{\dot{\epsilon}}.$$

As depicted in Figure 4.2b, at strain value 0.02, flow stress data at entire deformation temperatures and a specific strain rate were incorporated into Equation (4.5),

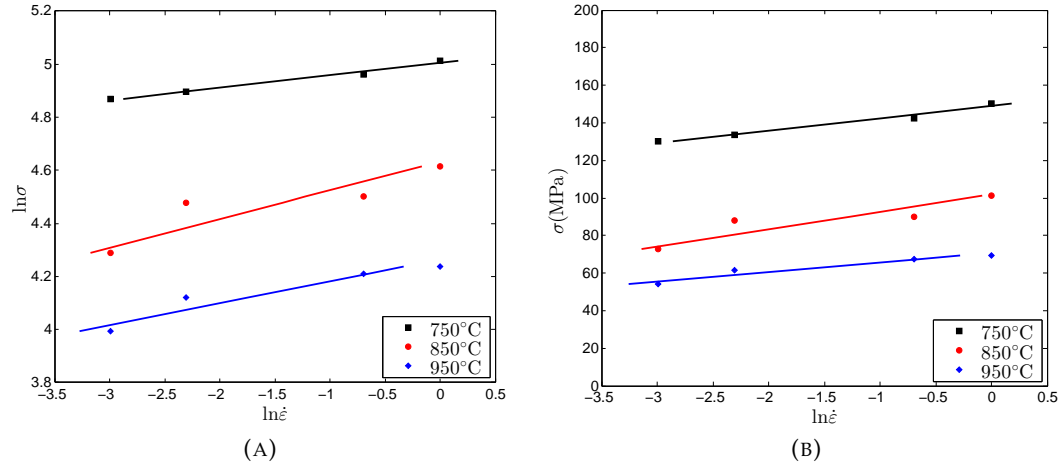


FIGURE 4.1: Relationship plots of  $\sigma$  and  $\dot{\epsilon}$  at  $\epsilon = 0.02$  (a)  $\ln \dot{\epsilon}$  and  $\ln \sigma$ ; (b)  $\ln \dot{\epsilon}$  and  $\sigma$ .

and the material constant,  $Q$ , was estimated by averaging four different strain rates outcome from the correlation plot ( $10^3/T$  and  $\ln(\sinh(\alpha\sigma))$ ).

For the evaluation of material constant,  $\ln A$ , Equation (4.1) is substituted into Equation (4.2) and performing the log-transform in both sides gives (Kyunghoon et al., 2017; Zhang et al., 2019)

$$\ln Z = \ln \dot{\epsilon} + [Q/(RT)] = \ln A + n \ln[\sinh(\alpha\sigma)]. \quad (4.7)$$

Similarly, considering entire test conditions with their corresponding stress data at plastic strain 0.02 and replacing the model constants in Equation (4.7) by estimated values of  $\alpha$ ,  $n$  and  $Q$ , the material constant,  $\ln A$ , was determined as 67.4369, from the intercept of Figure 4.3. In general, the experimental data used to fit Equation (4.7) to find the material constant,  $\ln A$ , and by repeating the same procedures, the material constants can be achieved at other selected strain samples.

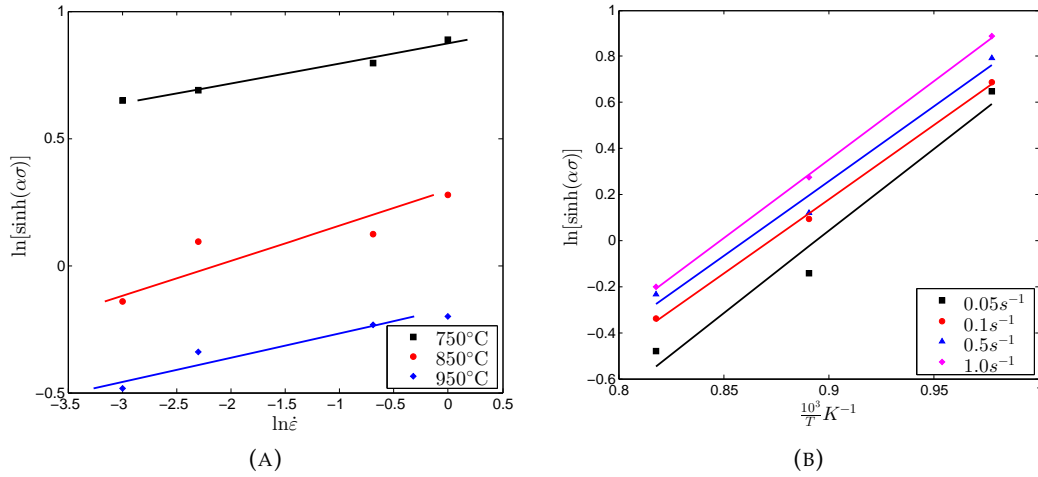


FIGURE 4.2: Relationship plot of  $\sigma$  and  $\dot{\epsilon}$  at  $\epsilon = 0.02$  (a)  $\ln\dot{\epsilon}$  and  $\ln(\sinh(\alpha\sigma))$ ; (b)  $10^3/T$  and  $\ln(\sinh(\alpha\sigma))$ .

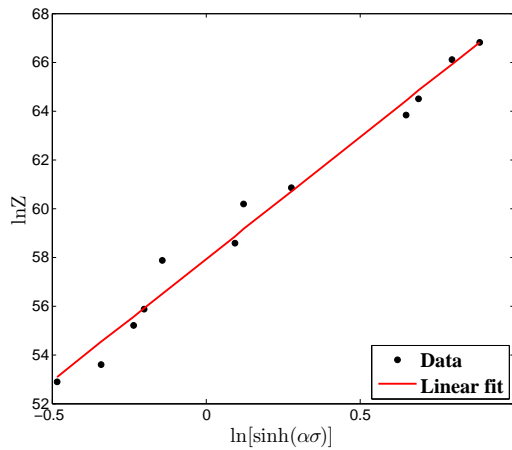


FIGURE 4.3: Correlation plot of stress and strain rate at  $\epsilon = 0.02$ .

### 4.3.2 Strain Compensation

The material constants such as  $\alpha$ ,  $n$ ,  $Q$ ,  $\ln A$  were assessed at selected plastic strains varying from 0.02 to 0.25. The material constants were fitted through 6th order regression function, and the computed model coefficients are tabulated in Table 4.1. Once the materials constants such as  $Q$ ,  $\ln A$ ,  $\alpha$ , and  $n$  are estimated by considering strain compensation, the flow-stress ( $\sigma$ ) at specific strain ( $\epsilon$ ) can be evaluated as

shown below:

$$\sigma = \sigma(\varepsilon, \dot{\varepsilon}, T; Q(\varepsilon), \ln A(\varepsilon), \alpha(\varepsilon), n(\varepsilon))$$

$$\sigma = \frac{1}{\alpha(\varepsilon)} \operatorname{arcsinh} \left\{ \exp \left[ \frac{\ln \dot{\varepsilon} - \ln A(\varepsilon) + Q(\varepsilon)/(RT)}{n(\varepsilon)} \right] \right\}. \quad (4.8)$$

TABLE 4.1: Estimated coefficients of fitted empirical models.

Coefficients	$\alpha/\text{MPa}^{-1}$	$n$	$Q/\text{kJmol}^{-1}$	$\ln A/\text{s}^{-1}$
$\beta_0$	0.0142	9.484	582.9	58.62
$\beta_1$	-0.2474	79.16	116.6	91.64
$\beta_2$	4.557	-2961	$-6.386 \times 10^4$	-8930
$\beta_3$	-46.23	$3.434 \times 10^4$	$7.02 \times 10^5$	$1.003 \times 10^5$
$\beta_4$	254.2	$-1.859 \times 10^5$	$-3.202 \times 10^6$	$-4.97 \times 10^5$
$\beta_5$	-711.9	$4.66 \times 10^5$	$5.877 \times 10^6$	$1.101 \times 10^6$
$\beta_6$	797.0	$-4.311 \times 10^5$	$-2.439 \times 10^6$	$-8.318 \times 10^5$

### 4.3.3 Constitutive Model Verification

Statistical measurements, such as  $R^2$ , root mean square error (RMSE), and an AARE, are utilized to verify the developed constitutive equations prediction capability at individual strains for an entire test conditions. To confirm the model capability, the graphical validation with systematic comparison was also adopted in this investigation. In this research, to discuss in detail about the prediction strength, an each experimental conditions were examined individually by computing statistical parameters such as  $R^2$  and AARE as summarized in Table 4.2.

As outlined in Table 4.2, the computed numerical numbers such as  $R^2$ , 0.982, and AARE, 3.678%, proves that the proposed constitutive equation is significantly appropriate to represent the material behavior at elevated temperatures; also it is much more suitable for future flow stress prediction at unknown strains. However,

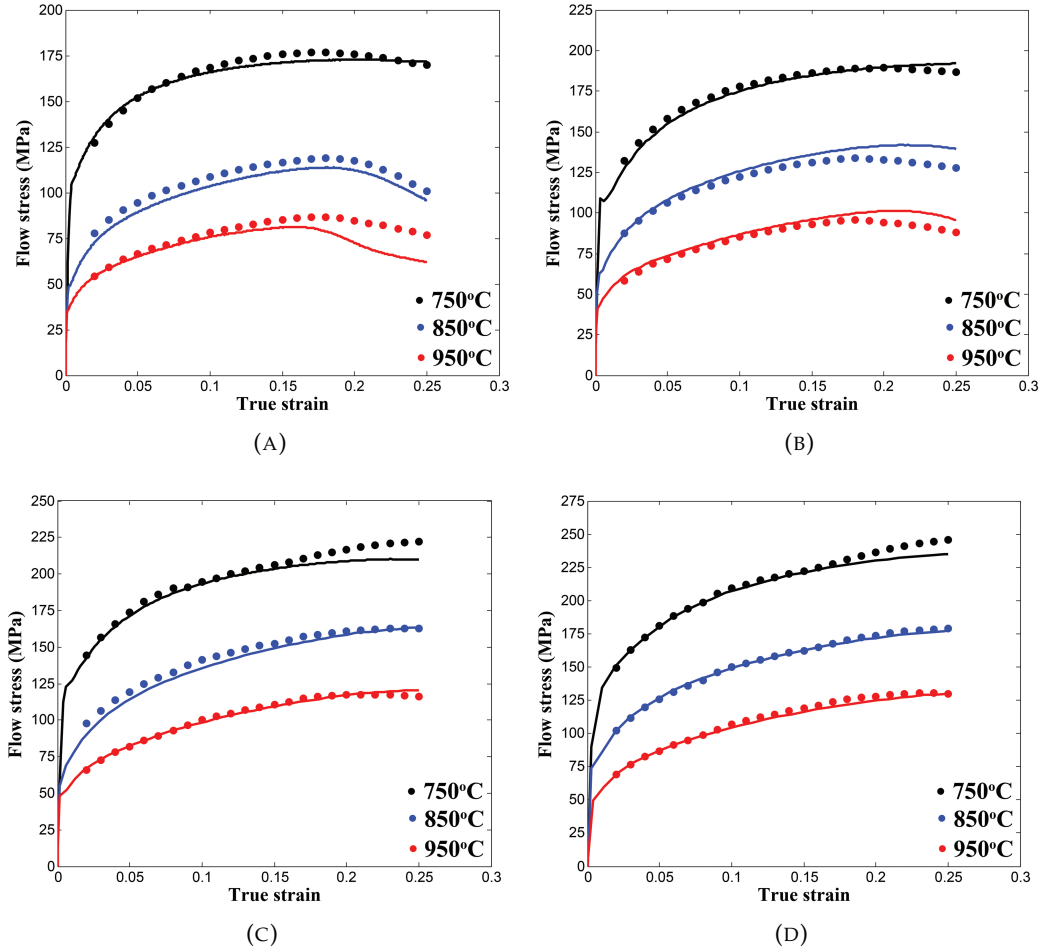


FIGURE 4.4: Comparison plot (a)  $0.05 \text{ s}^{-1}$ ; (b)  $0.1 \text{ s}^{-1}$ ; (c)  $0.5 \text{ s}^{-1}$ ; (d)  $1.0 \text{ s}^{-1}$ .

TABLE 4.2: Estimated statistical values of the conventional Arrhenius-type constitutive model.

Counts	Test Conditions	$R^2$	Adj. $R^2$	Overall- $R^2$	AARE (%)	Overall-AARE (%)
24 samples	1023 K	0.9516	0.9511	0.9817	2.9204	3.6781
	0.05–1.0 $\text{s}^{-1}$ 1123 K	0.9406	0.9400		4.2528	
	1223 K	0.9427	0.9421		3.8609	

from prediction error (AARE), it is identified that there are some difference among the actual test and estimated data in test conditions, 850 °C and 950 °C ( $0.05 \text{ s}^{-1}$  and  $0.1 \text{ s}^{-1}$ ). The modified  $Z'$  parameter with the multiplication factor  $\dot{\epsilon}^{1/3}$  is (Krishnan



TABLE 4.3: Estimated statistical values of the modified Arrhenius-type constitutive model.

Counts	Test Conditions	$R^2$	Adj. $R^2$	Overall- $R^2$	AARE (%)	Overall-AARE (%)	
24 samples	1023 K	0.9720	0.9717	0.9894	2.0045	2.9840	
	0.05–1.0 s <sup>-1</sup>	1123 K	0.9708		0.9705		3.1223
	1223 K	0.9448	0.9443		3.8251		

et al., 2011)

$$Z' = \dot{\epsilon}^{4/3} \exp(Q/RT), \quad (4.9)$$

Using Equation (4.9), out of these combinations,  $\dot{\epsilon}^{9/10}$  was found to have a small prediction error, AARE, as 2.9840%, against experimental data. Table 4.3 displays that the prediction capability was found to be adequate by strain rate compensation in the constitutive equation. Overall, the estimated prediction error proves that the modified equation provides a better correlation than that of the conventional constitutive equation.

## 4.4 Artificial Neural Network Model

### 4.4.1 Proposing Flow Stress Model using ANN-BP Algorithm

A multi-layer feed forward ANN model with supervised learning procedure, BP algorithm for training, was employed to construct the functional relationship among input and output variables for predicting flow stress at hot working conditions as shown in Figure 4.5. As can be seen in Figure 4.5, there were three input variables: strain ( $\epsilon$ ), strain rate ( $\dot{\epsilon}$ ), and deformation temperature ( $T$ ), and one output variable, stress ( $\sigma$ ), in the neural network design. Before the network training process, entire input and output variables are normalized in order to obtain a usable form for the

network using Eq. (4.10).

$$X_N = \frac{X - 0.95X_{\min}}{1.05X_{\max} - 0.95X_{\min}} \quad (4.10)$$

where  $X$  is the measured experimental data,  $X_{\min}$  and  $X_{\max}$  are the minimum and maximum values of chosen actual data such as stress ( $\sigma$ ), strain ( $\epsilon$ ), strain rate ( $\dot{\epsilon}$ ), and deformation temperature ( $T$ ), respectively, and  $X_N$  is the normalized data. The experimental values are normalized between more than 0 and less than 0.95, because in the end points, the transfer functions showed a slow learning rate behavior while training the network model (Razavi et al., 2011).

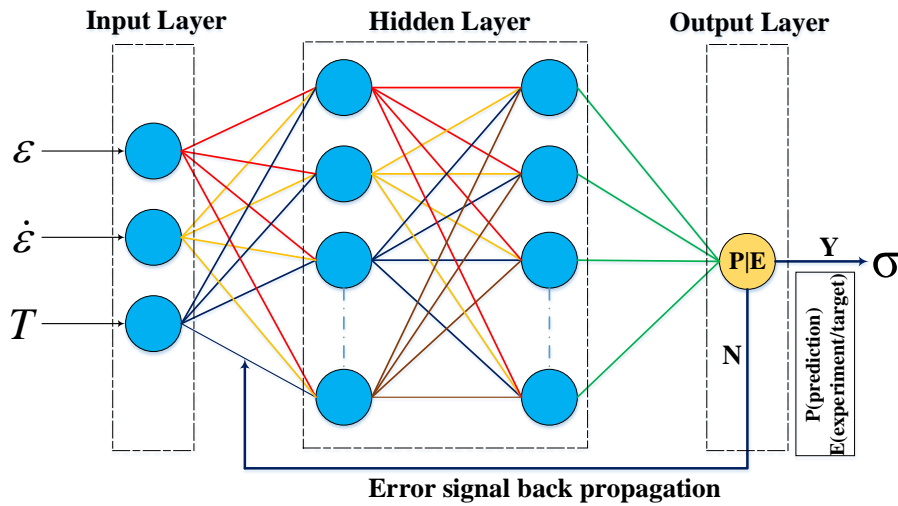


FIGURE 4.5: Back-propagation artificial neural network (BP-ANN) architecture for flow stress prediction (supervised learning).

For choosing transfer function in the hidden layer, two most widely used functions such as tan-sigmoid (Eq. (4.11)) and log-sigmoid (Eq. (4.12)), are adopted. In addition, among the available training functions, trainbr (Bayesian regularization) and trainlm (Levenberg-Marquardt) functions were picked based on their capability to learn to map inputs to outputs within given data-set. For the output layer, the transfer function was directly selected as purelin (linear function) because

TABLE 4.4: Network model instructions used for constructing flow stress model.

Number of samples	384 data (268 (Training) + 58 (validation) + 58 (Testing))
Input layer	three variables
Hidden layer functions	LOGSIG and TANSIG
Number of neurons	two $\leq$ HNs $\leq$ 30
Output layer	one variable
Output layer function	Purelin
network type	multi-layer feed-forward
net algorithm	back-propagation
Training functions	Trainbr and Trainlm
Learning function	LEARNGDM
Performance function	MSE

the problem assumed to be linear in the output layer as the model output was proportional to the total weighted inputs.

$$\text{tansigmoid function : } a = \frac{2}{1 + \exp(-2n)} - 1 \quad (4.11)$$

$$\text{logsigmoid function : } a = \frac{1}{1 + \exp(-n)} \quad (4.12)$$

It is obvious that more number of neurons lead to higher accuracy, but however, after 18 neurons (trainbr), error sums are fluctuating in a random manner. This fluctuation conveys that in order to control over-fitting with unknown points, the size of neurons should be limited to acceptable margin. Therefore, considering the network model complexity, the error differences are inspected closely from 4 to 30 neurons and identified that the predicted results are reasonably accurate when the network contains eight neurons in the hidden layer.

Moreover, the network model performance also depends on learning parameters, such as the number of training epochs and the performance goal, etc. But in this work, the number of epochs, the learning rate, and the error threshold were fixed

to a certain level based on the literature survey as 1000, 0.05 and  $1 \times 10^{-06}$ , respectively. The mean square error (MSE) quantity between actual and predicted data was recorded during network model training and using minimized or converged MSE value, the best models were obtained for both activation functions. Now the trained ANN-BP model should be verified to make a confirmation that the model implementation was done correctly. The evaluation techniques presented in this research work is significantly sufficient to confirm the model capability, because the prediction outcomes are always tested against experimental observations. For quantification purpose, three kinds of statistical parameters such as  $R^2$ , AARE, and RMSE are utilized (Mohanraj, Beom-Soo, and Kyunghoon, 2015). The population parameters are computed for each test conditions and summarized in Table 4.5. It is clearly seen that both transfer functions in the hidden layer displayed a significantly better outcome. For tansig activation function,  $R^2$  and AARE were estimated as 0.9980 and 1.3348%, respectively, and whereas for logsig activation function,  $R^2$  and AARE were determined as 0.9991 and 1.8059%, respectively. But, in test conditions, 850 °C and 950 °C, the prediction error was found to be higher, but it was significantly acceptable as the error value was close to 2.2%. These results confirm that the ANN-BP model can provide accurate representation of material flow behavior under hot deformation conditions. Besides, the plastic-instability phenomenon also tended to be captured more effectively than that of available traditional flow stress models (Murugesan and Jung, 2019a; Murugesan and Jung, 2019b).

#### 4.4.2 Optimization Procedures for Obtaining the Best ANN-BP Model

In the neural network model, the training process is carried out using an iterative process, which means in each step the model is updated with small weights and biases, for finding an optimum set of weights and biases to improve the model performance. A general approach for solving the neural network problem is to

TABLE 4.5: Computed statistical parameters from an ANN-BP model.

ANN transfer function	Test Conditions	$R^2$	Overall- $R^2$	AARE (%)	Overall-AARE (%)	
TANSIG	0.05–1.0 s <sup>-1</sup>	923 K	0.9918	0.9980	1.6397	1.8059
		1023 K	0.9990		1.4028	
		1123 K	0.9995		2.1722	
		1223 K	0.9998		2.0092	
LOGSIG	0.05–1.0 s <sup>-1</sup>	923 K	0.9971	0.9991	0.8637	1.3348
		1023 K	0.9996		0.8927	
		1123 K	0.9997		1.4321	
		1223 K	0.9998		2.1507	

restart the training process multiple times with different random initial weights and biases, and allow the searching algorithm to find distinct candidates for the best trained ANN-BP model. This process is usually called multiple restarts. In this research work, the multiple restarts process was modeled by employing hybrid optimization procedures for training a network model in terms of adjusting weights and biases to predict the flow stress of medium carbon steel material under hot deformations as shown in Figure 4.6. The nonlinear programming function, `fmincon`, was utilized considering the IP algorithm to minimize AARE between an ANN-BP model and the desired flow stress data; the bounds constrained optimization procedures exploited in this work is also depicted in Figure 4.7. The IP algorithm was selected due to its advantage in finding the minimum of a function within the presence of bounds constraints. Moreover, the benefits of exploiting this `fmincon` function rather than GA is that the computational time to solve the problem can be minimized without compromising the accuracy of results eventually (Chuan, Lei, and Jianguo, 2014). In general, it is difficult to mention whether using wide range of bounds are valid or not at the first place. Therefore, at start of the optimization process, the problem was tested with a small range of bounds and then increased a little wider for allowing the process to be sampled extensively before selecting a valid candidate for a better solution. The general form of optimization procedures

are expressed below:

$$\begin{cases}
 \text{Minimize:} \\
 x \\
 \text{AARE} = \frac{1}{n} \sum_{i=1}^n \left| \frac{\sigma_{\text{exp}}^i - \sigma_{\text{ANN}}^i}{\sigma_{\text{exp}}^i} \right| \times 100\%, \\
 \text{where, } \sigma_{\text{ANN}} \text{ from best ANN-BP model} \\
 \text{subjected to} \\
 \begin{cases}
 \text{IW}_{\text{lb}} \leq x(1) \leq \text{IW}_{\text{ub}} \\
 \text{LW}_{\text{lb}} \leq x(2) \leq \text{LW}_{\text{ub}} \\
 \text{b1}_{\text{lb}} \leq x(3) \leq \text{b1}_{\text{ub}} \\
 \text{b2}_{\text{lb}} \leq x(4) \leq \text{b2}_{\text{ub}}
 \end{cases}
 \end{cases}$$

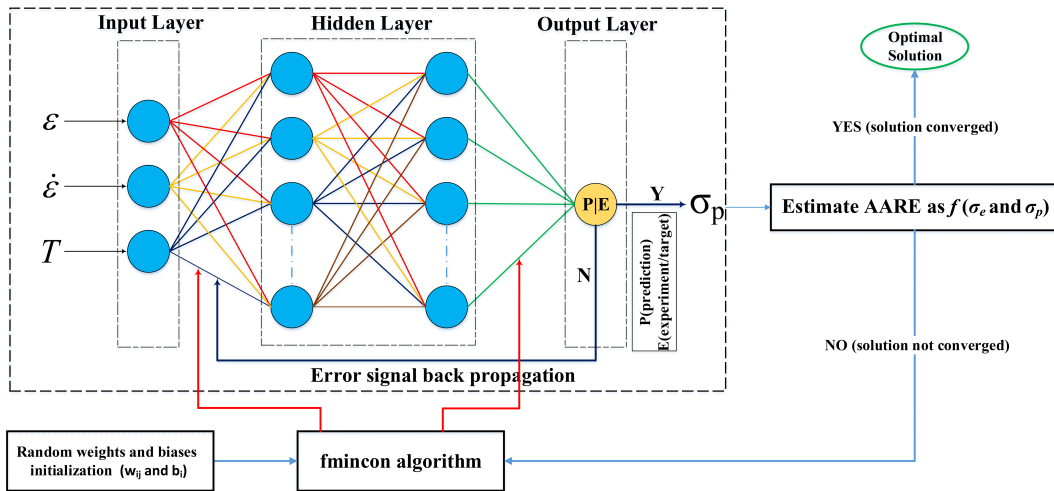


FIGURE 4.6: BP-ANN model with an OP for flow stress prediction.

The best candidate solutions for tansigmoid function in the hidden layer are obtained when the iterations and the function counts are 14 and 183, respectively, whereas for logsigmoid function, the numbers are computed as 5 and 71, respectively. The optimum solutions of AARE with transfer functions, tansig, and logsig, are achieved as 1.123% and 1.502%, respectively. The optimal results computed from

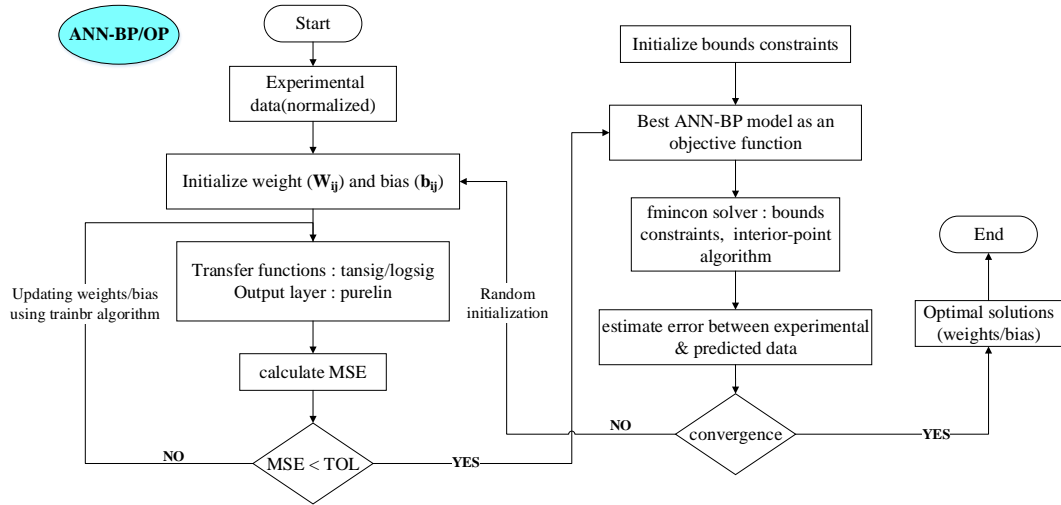


FIGURE 4.7: Flow chart of optimization procedures.

the proposed ANN-BP/OP model are tabulated in Table 4.6. Tables 4.5 and 4.6 are strong evidence that the prediction error obtained from the optimized network model varies from 0.728% to 1.775%, whereas for the basic network model, errors are ranging from 0.8637% to 2.172%, which states that the optimized ANN-BP model can correlate the material flow behavior more effectively than the conventional network model. In addition, there was no considerable differences between tansigmoid and logsigmoid functions with regard to the prediction error, but somehow, the optimum network model with tansigmoid function looks a little significant as far as reduction in the prediction error is concerned.

TABLE 4.6: Statistical parameters from an optimized ANN-BP model.

ANN transfer function	Test Conditions	$R^2$	Overall- $R^2$	AARE (%)	Overall-AARE (%)
TANSIG	923 K	0.9940	0.9989	1.1582	1.1229
	1023 K	0.9997		0.7282	
	1123 K	0.9998		1.0089	
	1223 K	0.9999		1.5963	
LOGSIG	923 K	0.9960	0.9988	1.0972	1.5017
	1023 K	0.9992		1.3804	
	1123 K	0.9996		1.7752	
	1223 K	0.9999		1.7541	

As can be seen in Figure 4.8, most of the predicted data points from the optimized ANN-BP model were close to the experimental measurements and this finding confirms the capability of the optimized flow stress model compared to the conventional network model. The correlation between experimental observations and the predicted is interesting because the computed data points almost followed the same trend line along the desired values as illustrated in Figure 4.8. Moreover, Figure 4.9a shows that the proposed model displayed a better correlation with respect to the measured data along with a better correlation coefficient  $R^2$  value at 0.9989. In addition, the statistical measurements,  $R^2$  and AARE, were estimated for each test condition using the proposed model as summarized in Table 4.6 and likewise, it displays the excellent prediction ability of the proposed network model. Figure 4.9b,c displays the random distribution of residuals with respect to zero error line; also, from the histogram plot (inset images), the distribution of residuals was noticed to be random and the probability distribution was found to be normal inside the working space. Furthermore, Figure 4.9c conveys that even after the optimization process, the residual plot showed a fairly random pattern, which indicates that the proposed model provided a modest fit to the desired data. In addition, in order to clearly depict the model performance, the prediction error comparison using an ANN-BP and an ANN-BP/OP was modeled at different deformation temperatures and strain rates as shown in Figure 4.10a.

According to our findings, the developed ANN models can be effectively applied to predict the material deformation behavior of medium carbon steel. Also the prediction error variations occurred in the traditional flow stress models (Murugesan and Jung, 2019a; Murugesan and Jung, 2019b), as shown in Figure 4.10b, that introduced by the plastic instability phenomenon can be eliminated. Overall, the presented discussion implies that the proposed ANN-BP model has more impact to deal with a nonlinear experimental data than that of the conventional flow stress



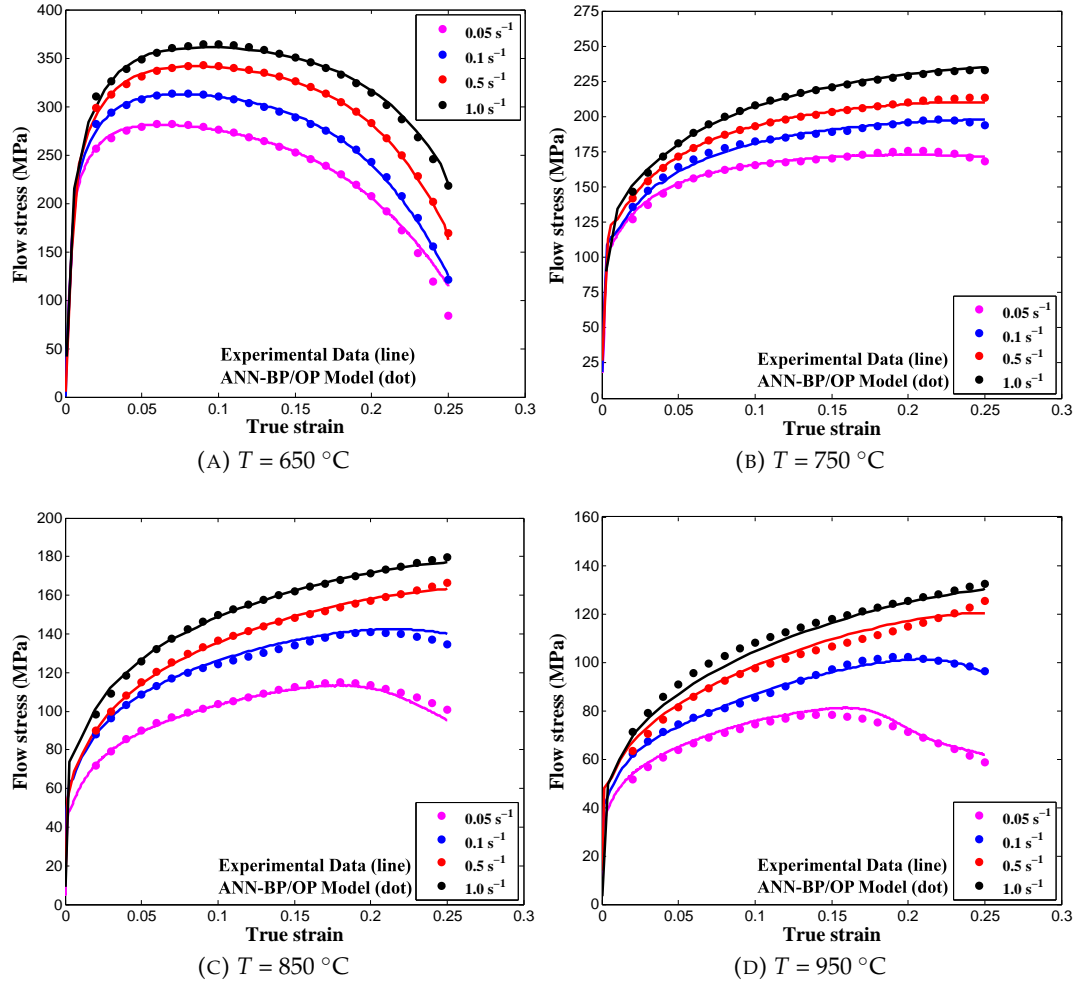


FIGURE 4.8: Comparison between experimental and predicted flow stress data using BP-ANN/OP model with TANSIG.

models in order to approximate the constitutive relationship of medium carbon steel at hot working conditions.

## 4.5 Conclusions

The Arrhenius-type constitutive equation was developed by considering both influence of strain and strain rate effects on the material constants. A sixth-order

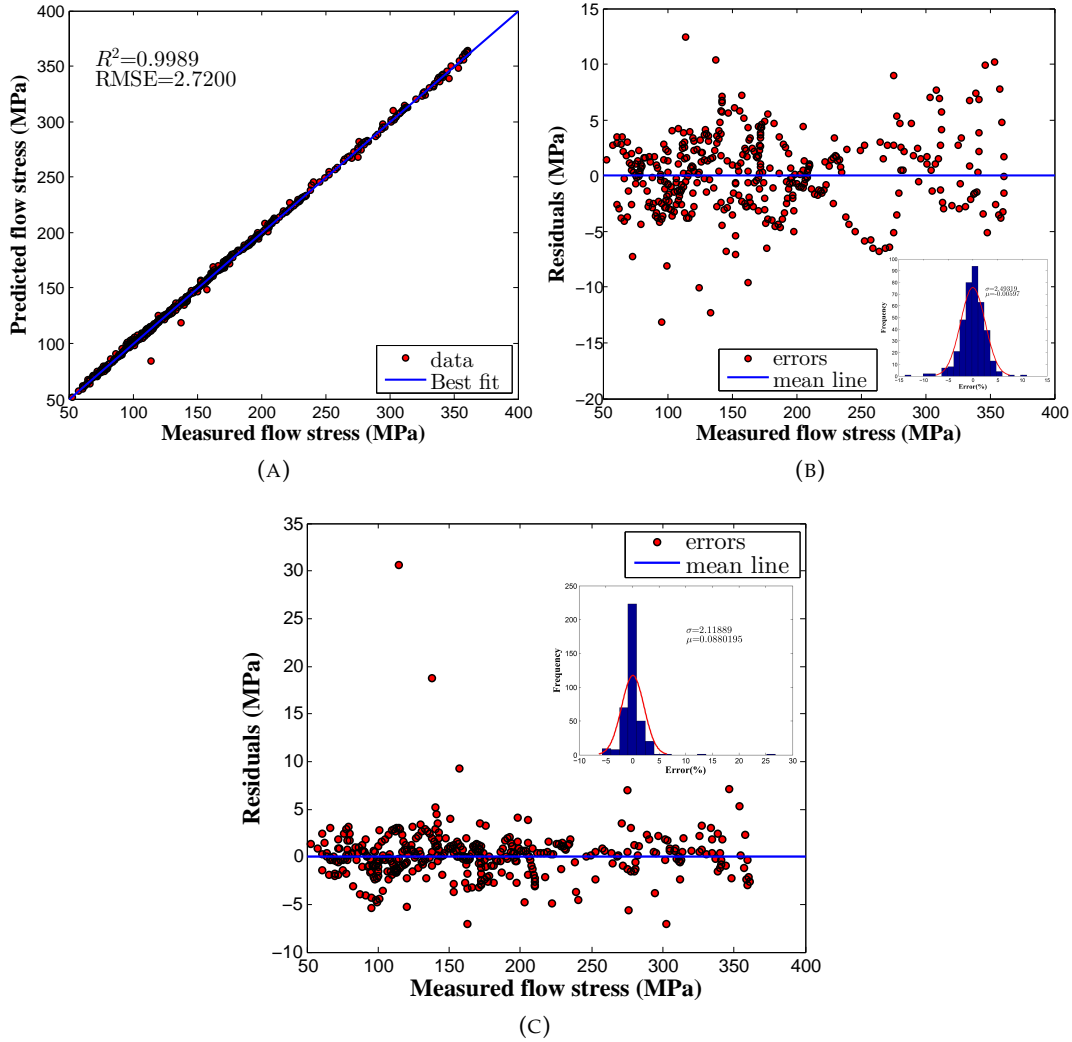


FIGURE 4.9: (a) Correlation plot; (b) Residual plot of an ANN-BP model; (c) Residual plot of an optimized ANN-BP model. (inset histogram plots).

regression function was adopted to fit the material constants, and the model adequacies were explained with the help of both numerical and graphical validations. Comparison with experimental results proved that the material flow behavior could be more precisely captured by the modified constitutive equation than the traditional constitutive model. In addition, the conventional constitutive model adequacy was quantified using the statistical parameters and the numerical numbers of  $R^2$  and

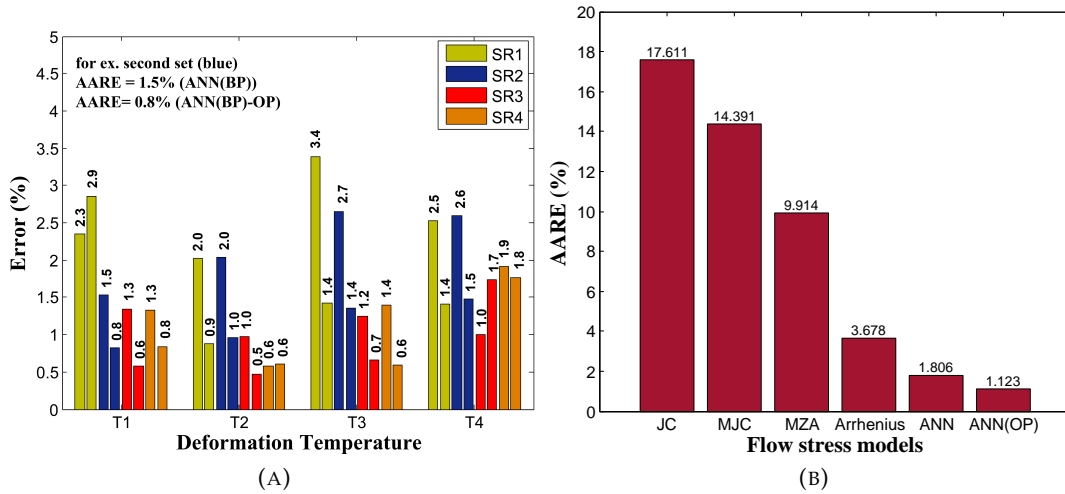


FIGURE 4.10: Graphical validation. (a) BP-ANN and BP-ANN/OP models comparison at various strain rates; (b) Prediction error comparison for proposed models.

AARE were computed as 0.9817 and 3.6781%, respectively, whereas for the modified constitutive model, the numerical numbers computed as 0.9894 and 2.9840%, respectively. Similarly, without optimization procedures the model was developed and the predicted results from the proposed network model displayed a good agreement with the experimental measurements. Subsequently, a hybrid algorithm was utilized for obtaining the best trained ANN-BP model to predict the flow stress of medium carbon steel material. From obtained results, it was found that an optimized BP-ANN with tansigmoid activation function displayed the much more accurate prediction capability to describe the material hot deformation behavior throughout the entire tested conditions. Moreover, the statistical measurements such as  $R^2$  and AARE, were calculated as 0.9989 and 1.1229%, respectively. Moreover, there were no mathematical model assumptions and physical insight needed to develop an ANN-BP model and these kind of procedures make it more effective to predict the material behavior than the conventional constitutive equations.

## Chapter 5

# SPIF Process Optimization using Response Surface Methodology

### 5.1 Summary

In this chapter, we experimentally investigate the forming process to determine the influence of process parameters and their contribution to enhancing the formability without causing a fracture by combining the design of experiments (DOE), grey relational analysis (GRA), and ANOVA. The DOE procedure, a central composite design with a face-centered option, is devised for AA3003-H18 Al alloy sheet for modeling the real-time experiments. The RSM approach is adopted to optimize the forming parameters and recognize the optimal test conditions. The statistically developed model is found to have agree with the test measurements. The prediction model's capability in  $R^2$  is computed as 0.8931, indicating that the fitted regression model adequately aligns with the estimated grey relational grade (GRG) data. Other statistical parameters, such as root mean square error (RMSE) and average absolute relative error (AARE), are estimated as 0.0196 and 2.78%, respectively, proving the proposed regression model's overall closeness to the measured data. In addition, the prediction error range is identified as  $-0.05$  to  $0.05$ , which is significantly lower and the residual data are distributed normally in the design space with variance

and mean of 3.3748 and  $-0.1232$ , respectively. ANOVA is performed to understand the adequacy of the proposed model and the influence of the input factors on the response variable. The model parameters, including step size, feed rate, interaction effect of tool radius and step size, favorably influence the response variable. The model terms  $X_2$  (0.020 and 11.30),  $X_3$  (0.018 and 12.16), and  $X_1X_2$  (0.026 and 9.72) are significant in terms of  $p$ -value and F-value, respectively.

## 5.2 Introduction

Aluminum alloys continue to be widely used in industrial applications such as automobile components, aircraft structures, and ship panels because of their excellent mechanical properties (Grażyna et al., 2020; Wu et al., 2021). Nowadays, manufacturing procedures need to be optimized to reduce the production cost and time without compromising the product quality. Comparing to conventional metal forming methods (Min et al., 2018), the ISF does not require any external die to produce the desired components as the new parts can be manufactured using the predefined contour tool path. This process uses the designed tool path to create a step-by-step deformation on the sheet metal part using the punch tool. However, the dimensional accuracy of the manufactured product from the SPIF process mainly depends on the working parameters such as punch tool radius, vertical step size, lubrication, spindle speed, and material selection and design parameters like geometry shape, sheet thickness, and wall angle (Ren et al., 2019; Wei et al., 2019; Maqbool and Bambach, 2018; Chang and Chen, 2020; Fiorentino, Giardini, and Ceretti, 2015; Said et al., 2016). The forming force also has a significant impact in the ISF process because excessive forming force can tear the sheet material due to thinning behavior, and the moderate forming force cannot deform the sheet metal to the desired shape (Bansal et al., 2017; Chang, Li, and Chen, 2019; Saidi et al., 2015).

So, choosing the proper forming punch tool is critical for preventing fractures and producing flawless parts (Ai et al., 2017; Davarpanah et al., 2015; Raju, Haloi, and Narayanan, 2017).

In this work, process parameters, such as forming tool radius, step size, and feed rate, were selected to investigate the formability of AA3003-H18 Al alloy sheets to obtain optimum forming conditions to identify the important parameters that influence the forming process by applying the design of experiments (DOE) statistical approach and grey relational analysis (GRA). The lubricant, a combination of oil and grease, was chosen over other lubricants for the tests based on the measured average surface roughness from incrementally formed parts produced using various lubricants. Real-time experiments were conducted using the experimental design developed from the central composite design with a face-centered option. Response surface methodology (RSM) was adopted for developing a grey relational grade (GRG) prediction model against the forming parameters, and statistical analysis of variance (ANOVA) was used to identify the influence of the process parameters on the response variable. The proposed prediction model was reviewed using graphical and numerical validations.

### 5.3 Experimental Procedures

This section discusses the procedures used to carry out the SPIF process experiments in detail. The computer numerical control (CNC) machine used in this research work was custom-made to conduct the forming process and to investigate and understand the deformation mechanism behind the ISF process. Figure 5.1 shows the detailed experimental set-up of the SPIF process; as illustrated, it consisted of a few essential tools such as a position sensor, a specifically shaped forming tool, blank holder, die systems, holding screws, and a thermometer. The material

sheet dimensions were chosen based on the working area of the customized design, and the chosen rectangular area of the aluminum sheet was  $240 \times 280 \text{ mm}^2$  with a thickness of 0.5 mm. The forming tool was manufactured from the high-speed steel (HSS) material due to its material properties such as high hardness, wear resistance, and heat resistance. The typical chemical composition of the selected commercial aluminum alloy (AA3003) material are summarized in Table 5.1.

TABLE 5.1: Chemical composition of AA3003-H18 material.

Composition	Al	Si	Fe	Cu	Mn	Zn
wt %	96.8–99.0	0.6	0.7	0.05–0.20	1.0–1.5	0.10

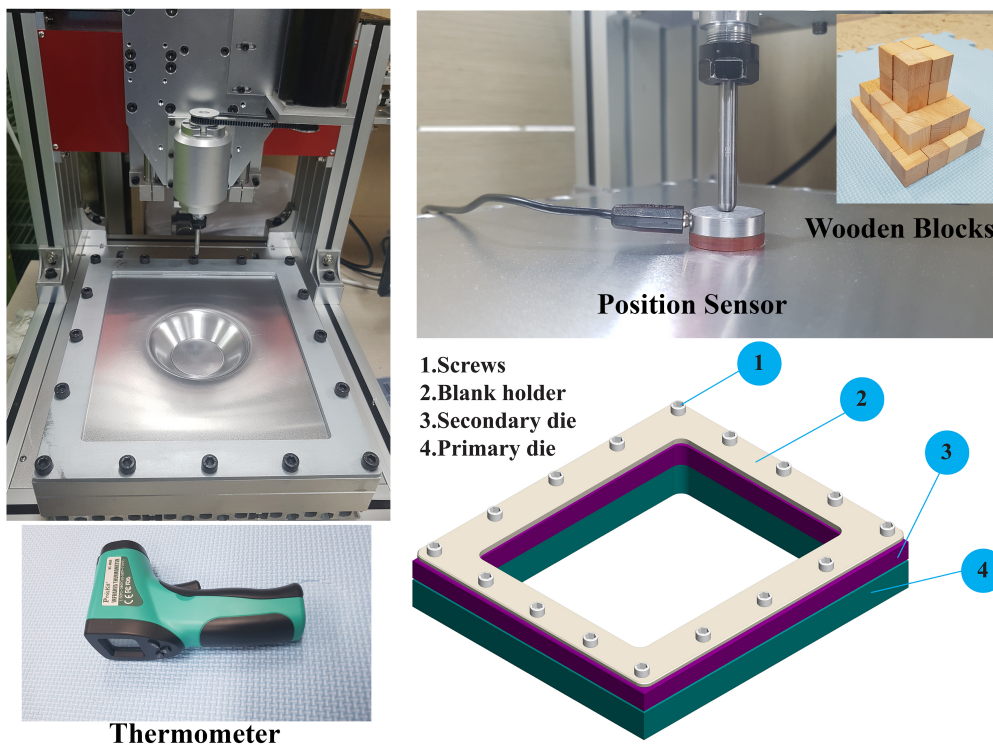


FIGURE 5.1: Experimental procedures of the single-point incremental forming process.

## 5.4 Design of Experiments

The design of experiments (DOE) is well-suited for evaluating the input variables that significantly influence the response variables outcome in the design space. This tool is robust as it can be exploited in any experimental situation to weigh and examine the factors that control other working parameters. For determining the important missing interaction terms that increase the possibility of capturing the desired output, the input factors can be altered and investigated simultaneously using the DOE approach (Mohanraj, Beom-Soo, and Kyunghoon, 2015). The detailed procedures to conduct the DOE process are illustrated in Figure 5.2a, and the main steps are classified as planning, conducting, analyzing, and interpreting the outcome of the real experiments. In this research, the real-time SPIF experiments were conducted using the modified CNC vertical milling machine. For conducting the experiments, the experimental design was applied using statistical software Minitab 18, and the experimental design was a 3-factor, 3-level factorial experiment, which are referred to as low, medium, and high levels. The forming parameters, including tool radius, step size, and feed rate, were customized according to the capability of the designed CNC machine, and Table 5.2 outlines the control forming parameters chosen for the experiments and their design spaces with various levels.

TABLE 5.2: Design spaces of forming parameters and their levels.

Variables		Levels		
		Low	Center	High
		-1	0	+1
Tool radius (mm)	$x_1$	2.0	2.5	3.0
Step size (mm)	$x_2$	0.2	0.5	0.8
Feed rate (mm/min)	$x_3$	1000	2000	3000



As per the central composite design (CCD) considering the face-centered option (Figure 5.2b), the 20 sets of the experimental runs were obtained as factorial points (1–8), star points (9–14), and center points (15–20), as summarized in Tables 5.3 and 5.4. Because of the 6 similar center points concerning the central composite face-centered (CCF) design, the responses were averaged from the repetition of the SPIF experiments without altering any test conditions. After each experiment (Figure 5.2c), the tested material surface roughness ( $R_a$ ) was measured from three different locations (Udroiu, Braga, and Nedelcu, 2019), and the average value of the surface roughness was taken, as summarized in Tables 5.3 and 5.4. The measurement procedures were repeated for the other output responses including thickness, forming time, angle, and height, and we obtained fifteen sets of test results, as documented in Tables 5.3 and 5.4.

The procedures used to measure the thickness in the formed part using a micrometer screw gauge are presented in Figure 5.3. To determine the shape error in terms of free bending and edge waviness, the incrementally produced parts were approximately cut down the middle; then, the prepared samples were checked for fractures and used for 3D scanning to obtain the cross-section coordinates and to estimate the shape error. For the 3D scanning process, the cut-down samples were prepared with a minimum of 12 reference point targets using 3D scan mark dot stickers. Here, the ATOS 3D Scanner was used for the three-dimensional measurements of the formed parts, as shown in Figure 5.4. The main advantage of this scanner is that it does not need any physical probes to manually touch multiple coordinates. The scanning process was repeated multiple times to improve the model accuracy, and the scanned model was stored in a computer-aided design (CAD) file.

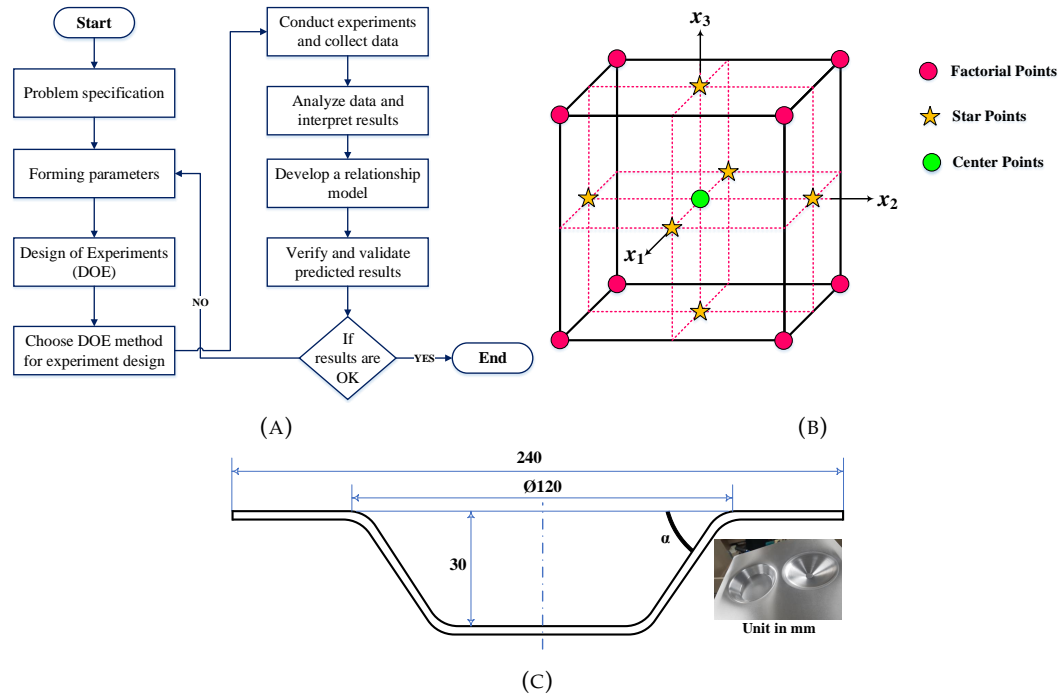


FIGURE 5.2: (a) Flow chart of experimental design process; (b) CCF design; (c) truncated conical geometry.

## 5.5 Grey Relational Analysis

Grey relational analysis (GRA) is employed to determine the best combination of input parameters by converting a multi-objective problem into a single-objective problem to achieve the most reliable response for the chosen output parameters. This method is widely implemented to evaluate and assess the performance of a selected complex problem or a problem with multiple output responses. For obtaining accurate solutions, a particular set of sequences, as outlined in the algorithm table 1, has to be performed using the test data acquired from the real-time experiments for the chosen response variables. Firstly, the experimental observations were normalized using operation 1 for the chosen response variables, as summarized in Table 5.5, called grey relational generations. The sheet thickness, the formed angle,

TABLE 5.3: CCF experimental design and experimental results of 30° cone angle

Wall Angle ( $\theta$ ), Time ( $t$ ), Height ( $h$ ), and Roughness ( $Ra$ )								
Run	$x_1$	$x_2$	$x_3$	Thickness (mm)	$\theta$ (°)	$t$ (min.s)	$h$ (mm)	$Ra$ ( $\mu\text{m}$ )
1	2.0	0.2	1000	0.475	28.8	32.45	27.8	0.755
2	3.0	0.2	1000	0.460	29.0	32.30	28.0	1.690
3	2.0	0.8	1000	0.475	31.1	9.05	25.5	2.080
4	3.0	0.8	1000	0.485	30.0	9.01	28.6	1.070
5	2.0	0.2	3000	0.470	29.8	11.05	27.4	0.820
6	3.0	0.2	3000	0.460	29.2	11.00	29.6	1.290
7	2.0	0.8	3000	0.485	28.9	3.11	29.0	1.395
8	3.0	0.8	3000	0.470	29.0	3.10	27.3	0.880
9	2.0	0.5	2000	0.455	29.7	7.01	27.0	0.788
10	3.0	0.5	2000	0.470	29.8	6.58	27.6	1.190
11	2.5	0.2	2000	0.455	29.8	16.27	28.2	0.880
12	2.5	0.8	2000	0.480	29.8	4.39	26.5	1.500
13	2.5	0.5	1000	0.475	31.0	13.45	28.9	0.930
14	2.5	0.5	3000	0.475	30.0	4.45	28.5	1.140
15 ~ 20	2.5	0.5	2000	0.470	31.5	7.00	27.5	0.990

and height were assumed to be the-higher-the-better among the selected variables. In contrast, the machining time and surface roughness were considered to better the smaller the values. The deviation sequence, which is the absolute value of the difference between  $x_{0j}(k)$  and  $x_{ij}(k)$ , was calculated (Table 5.6) using operation 2. Considering the distinguishing coefficient,  $\zeta$ , as 0.5, the grey relational coefficient was estimated using operation 3, as tabulated in Table 5.7. Before performing operations 4 and 5, the weight estimation was required for the selected responses; the Shannon entropy method, widely adopted in the decision-making process, was used for the estimation process (Pradhan, 2012; Wang, Zhu, and Wang, 2016; Kuo, Yang, and Huang, 2008; Song and Shepperd, 2011; Sankar and Umamaheswarrao,

TABLE 5.4: CCF experimental design and experimental results of 60° cone angle

Wall Angle ( $\theta$ ), Time ( $t$ ), Height ( $h$ ), and Roughness ( $Ra$ )								
Run	$x_1$	$x_2$	$x_3$	Thickness (mm)	$\theta$ (°)	$t$ (min.s)	$h$ (mm)	$Ra$ ( $\mu\text{m}$ )
1	2.0	0.2	1000	0.290	59.0	48.36	28.9	0.516
2	3.0	0.2	1000	0.295	57.7	48.04	28.6	1.090
3	2.0	0.8	1000	0.280	61.8	13.14	27.6	1.610
4	3.0	0.8	1000	0.295	58.2	13.06	29.6	1.310
5	2.0	0.2	3000	0.270	58.7	16.22	28.2	0.498
6	3.0	0.2	3000	0.270	60.0	16.11	29.7	1.463
7	2.0	0.8	3000	0.275	59.5	4.34	27.4	1.860
8	3.0	0.8	3000	0.320	61.5	4.32	27.8	1.060
9	2.0	0.5	2000	0.300	59.5	10.13	28.0	0.507
10	3.0	0.5	2000	0.320	57.2	10.07	28.7	1.010
11	2.5	0.2	2000	0.250	59.6	24.17	29.4	0.488
12	2.5	0.8	2000	0.315	59.2	6.42	25.9	1.410
13	2.5	0.5	1000	0.280	59.0	20.06	29.4	1.647
14	2.5	0.5	3000	0.270	62.0	6.52	29.8	1.230
15 ~ 20	2.5	0.5	2000	0.270	58.7	10.10	29.0	1.320

2016; Panda, Sahoo, and Rout, 2016; Su et al., 2020).

$$p_{ij} = \frac{x_{ij}}{\sum_{i=1}^m x_{ij}} \rightarrow E_{ij} = -k \sum_{i=1}^m p_{ij} \ln p_{ij} \quad \text{in which } k = 1/\ln(m) \quad (5.1)$$

$$w_j = \frac{1 - E_j}{\sum_{j=1}^n (1 - E_j)} \rightarrow w_j^* = \frac{s_j w_j}{\sum_{j=1}^n s_j w_j} \quad (5.2)$$

At first, the response variables normalized to achieve the design outcomes ( $p_{ij}$ ) and then the entropy measures computation of the design outcomes ( $E_{ij}$ ) were estimated using Eq. (5.1). Likely from Eq. (5.2), the standard form of entropy weight estimation ( $w_j^*$ ) was established by combining the subjective ( $s_j$ ) and objective weights ( $w_j$ ); the parameters weights were determined to be  $w_1=w_2=w_3=w_4=w_5=0.2$ , which means an equal weight for each response. Then, the grey relational grade

(GRG) was computed using the weights estimated from the Shannon entropy weighting method and operations, 4 and 5, as summarized in Table 5.8. The optimal combination was determined from the higher GRG rank, which was experimental run 14, as listed in Table 5.8.

---

**Algorithm 1:** Procedures used for grey relational analysis (GRA) (Pradhan, 2012; Wang, Zhu, and Wang, 2016; Kuo, Yang, and Huang, 2008; Song and Shepperd, 2011; Sankar and Umamaheswarrao, 2016; Panda, Sahoo, and Rout, 2016; Su et al., 2020).

---

- 1 Normalization: If the likelihood is the-smaller-the-better (SB) or the-higher-the-better (HB),

$$\text{SB: } x_{ij}(k) = \frac{\max x_{ij}(k) - x_{ij}(k)}{\max x_{ij}(k) - \min x_{ij}(k)}$$

$$\text{HB: } x_{ij}(k) = \frac{x_{ij}(k) - \min x_{ij}(k)}{\max x_{ij}(k) - \min x_{ij}(k)}$$

- 2 Evaluation of  $\Delta_{ij}$ :  $\Delta_{ij} = |x_{0j}(k) - x_{ij}(k)|$
- 3 Grey relational coefficient calculation:

$$\gamma(x_{0j}, x_{ij}) = \frac{\Delta_{\min} + \zeta \Delta_{\max}}{\Delta_{ij}(k) + \zeta \Delta_{\max}} \longleftarrow \Delta_{ij} = |x_{0j}(k) - x_{ij}(k)|,$$

where  $\gamma(x_{0j}, x_{ij})$  is the grey relational coefficient between  $x_{ij}$  and  $x_{0j}$ .  $\Delta_{\max}$  is the maximum value of  $\Delta_{ij}$ , and  $\Delta_{\min}$  is the minimum value of  $\Delta_{ij}$ .  $\zeta$  is the distinguishing coefficient ( $0 \leq \zeta \leq 1$ ), and assumed to be 0.5.

- 4 From the grey relational coefficient, the grey relational grade (GRG) is determined as follows:

$$\gamma_i = \frac{1}{n} \sum_{j=1}^n \gamma(x_{0j}, x_{ij}).$$

- 5 Considering the weighting method in real-time applications, the GRG can be rewritten as:

$$\gamma_i = \frac{1}{n} \sum_{k=1}^n w_k \gamma(x_{0j}, x_{ij}),$$

where  $w_k$  is the weighting factor for  $k$ . In the present investigation, the weighting value  $w_k$  for the response each parameter was estimated from the Shannon entropy weighting method.

- 6 Rank according to the values of the GRG in decreasing order.
-

TABLE 5.5: Grey relational generation values.

Run	Wall Angle (30°)				
	$y_1$ (mm)	$y_2$ (°)	$y_3$ (min.s)	$y_4$ (mm)	$y_5$ ( $\mu\text{m}$ )
	HB	HB	SB	HB	SB
1	0.667	0.000	0.000	0.561	1.000
2	0.167	0.074	0.005	0.610	0.294
3	0.667	0.852	0.797	0.000	0.000
4	1.000	0.444	0.799	0.756	0.762
5	0.500	0.370	0.729	0.463	0.951
6	0.167	0.148	0.731	1.000	0.596
7	1.000	0.037	1.000	0.854	0.517
8	0.500	0.074	1.000	0.432	0.906
9	0.000	0.333	0.867	0.366	0.975
10	0.500	0.370	0.881	0.512	0.672
11	0.000	0.370	0.551	0.659	0.906
12	0.833	0.370	0.956	0.244	0.438
13	0.667	0.815	0.647	0.829	0.868
14	0.667	0.444	0.954	0.732	0.709
15	0.500	1.000	0.867	0.488	0.823

TABLE 5.6: Evaluation of deviation sequence.

Run	Wall Angle (30°)				
	$y_1$ (mm)	$y_2$ (°)	$y_3$ (min.s)	$y_4$ (mm)	$y_5$ ( $\mu\text{m}$ )
	HB	HB	SB	HB	SB
1	0.333	1.000	1.000	0.439	0.000
2	0.833	0.926	0.995	0.390	0.706
3	0.333	0.148	0.203	1.000	1.000
4	0.000	0.556	0.201	0.244	0.238
5	0.500	0.630	0.271	0.537	0.049
6	0.833	0.852	0.269	0.000	0.404
7	0.000	0.963	0.000	0.146	0.483
8	0.500	0.926	0.000	0.568	0.094
9	1.000	0.667	0.133	0.634	0.025
10	0.500	0.630	0.119	0.488	0.328
11	1.000	0.630	0.449	0.341	0.094
12	0.167	0.630	0.044	0.756	0.562
13	0.333	0.185	0.353	0.171	0.132
14	0.333	0.556	0.046	0.268	0.291
15	0.500	0.000	0.133	0.512	0.177

TABLE 5.7: Estimated values of grey relational coefficient.

Run	Wall Angle (30°)				
	$y_1$ (mm)	$y_2$ (°)	$y_3$ (min.s)	$y_4$ (mm)	$y_5$ ( $\mu\text{m}$ )
	HB	HB	SB	HB	SB
1	0.600	0.333	0.333	0.532	1.000
2	0.375	0.351	0.334	0.562	0.415
3	0.600	0.771	0.712	0.333	0.333
4	1.000	0.474	0.713	0.672	0.678
5	0.500	0.443	0.649	0.482	0.911
6	0.375	0.370	0.650	1.000	0.553
7	1.000	0.342	0.999	0.774	0.509
8	0.500	0.351	1.000	0.468	0.841
9	0.333	0.429	0.790	0.441	0.953
10	0.500	0.443	0.808	0.506	0.604
11	0.333	0.443	0.527	0.594	0.841
12	0.750	0.443	0.919	0.398	0.471
13	0.600	0.730	0.586	0.745	0.791
14	0.600	0.474	0.916	0.651	0.632
15	0.500	1.000	0.790	0.494	0.738

TABLE 5.8: Computed values of the grey relational grade (GRG) and rank.

Run	1	2	3	4	5	6	7	8	9	10
GRG	0.576	0.446	0.570	0.658	0.600	0.592	0.633	0.703	0.636	0.619
Rank	13	15	14	3	9	12	5	2	4	7
Run	11	12	13	14	15					
GRG	0.593	0.599	0.615	0.707	0.631					
Rank	11	10	8	1	6					

## 5.6 Response Surface Methodology

Response surface methodology (RSM) is a statistical tool that is useful for developing and analyzing the relationship between the independent and the dependent parameters of the individually designed problem. This method uses an appropriate selection of the DOE method to construct a suitable empirical mathematical model through the appropriate fitting of the real-time test data and discussion of the interaction effects of the input variables against the output variables. The second-order

polynomial model, which contains both linear and non-linear terms along with interaction terms, used for proposing the mathematical model with 3 regressor variables,  $k$ , can be expressed as (Mohanraj, Beom-Soo, and Kyunghoon, 2015; Kyunghoon et al., 2017):

$$y_i = a_0 + a_1x_{i1} + a_2x_{i2} + a_3x_{i3} + a_4x_{i1}^2 + a_5x_{i2}^2 + a_6x_{i3}^2 + a_7x_{i1}x_{i2} + a_8x_{i2}x_{i3} + a_9x_{i3}x_{i1} + \epsilon, \quad (5.3)$$

where  $i=1, 2, \dots, n$ . Assuming  $x_{i4} = x_{i1}^2$ ,  $x_{i5} = x_{i2}^2$ ,  $x_{i6} = x_{i3}^2$ ,  $x_{i7} = x_{i1}x_{i2}$ ,  $x_{i8} = x_{i2}x_{i3}$ , and  $x_{i9} = x_{i3}x_{i1}$ , Eq. (5.3) can be rewritten in a simplified form as (Mohanraj, Beom-Soo, and Kyunghoon, 2015; Kyunghoon et al., 2017):

$$y_i = a_0 + \sum_{i=1}^n \sum_{j=1}^p a_j x_{ij} + \epsilon. \quad (5.4)$$

In Eq. (5.4),  $a_0$  and  $a_j$  are the regression coefficients,  $n$  is the total number of test points, and  $p$ , ( $k \times 3$ ), is a limit calculated based on the number of independent variables ( $k$ ).

Eq. (5.4) can be expressed more conveniently using matrix notation:

$$y = Xa + \epsilon,$$

where  $y$  ( $n \times 1$ ),  $X$  ( $n \times p$ ),  $a$  ( $p \times 1$ ), and  $\epsilon$  ( $n \times 1$ ) are the response observations, the independent variables, the regression coefficients, and the noise measurements (Mohanraj, Beom-Soo, and Kyunghoon, 2015; Kyunghoon et al., 2017) in vector and matrix forms, respectively. Through error minimization between the test and predicted samples, the model regression coefficients can be estimated using the least-squares procedures. Therefore, the least-squares estimate of  $a$  is (Mohanraj,



Beom-Soo, and Kyunghoon, 2015; Kyunghoon et al., 2017):

$$\hat{a} = (X^T X)^{-1} X^T y.$$

Eventually, from the estimated model coefficients,  $\hat{a}$ , the responses,  $\hat{y}$ , at unknown samples can be calculated as (Mohanraj, Beom-Soo, and Kyunghoon, 2015; Kyunghoon et al., 2017):

$$\hat{y} = X\hat{a}.$$

## 5.7 Results and Discussion

This section discusses the surface finish of the incrementally formed parts, the influence of the process parameters on the response variable from ANOVA results and the shape error of the produced parts using 3D scanning process. At first, we aimed to form a part with a 60 mm outer radius, 30 mm forming height, and two forming angles (30° and 60°) using the SPIF process, as shown in Figure 5.3. For this investigation, the influences of the forming parameters, including tool radius, vertical step-size, and feed-rate, were considered, whereas other parameters like sheet thickness, tool shape, and lubricant remained constant. As an example, an incrementally formed part at the end of the forming process is depicted in Figure 5.3; the magnified views are provided to show the part's surface finish. The magnified pictures show that the forming tool's contour path can be noticed with the 30° truncated cone shape compared to the 60° cone shape. Edge waviness is noticed on the formed sheet at the fixture location, which occurred due to material flexibility and sheet fluctuations during the continuous incremental forming process. In detail, the fluctuations occurred during the forming process because the incremental forming process intends to form a material sheet gradually and locally by applying the punch force at a specified location; as the process continues based on the predefined tool path,

the fluctuations tend to occur throughout the entire process. However, close to the support, as highlighted in Figure 5.3, this edge waviness was not witnessed due to the strong bending at that location.

The desired 3D CAD models were compared against the scanned models to check for the presence of deviations, as depicted in Figure 5.4. As shown in Figure 5.4a,b, the formed parts tended to have an extra backward bending at the fixture location in both forming angle cases. Apart from the test results, the 3D scanned contour shows that deviations were identified as 10.94 mm for 60° and 12.34 mm for 30° truncated conical geometries. The slightest error may have occurred in the scanned model data due to the reference point alignment during model comparison. However, the data were cross-verified by manual measurement, and the computed shape deviation was confirmed to be close to the manual estimation. For evaluating the accuracy of the formed part, the finite element model was modeled, and the mechanical properties achieved from the tensile test were incorporated into the material card, MAT18, which can consider the power law of plasticity for describing the material's plastic behavior. The FEM accuracy was controlled with a reasonable number of elements in the blank material and was considered to be deformable; the forming tool was meshed with coarse elements and considered to be rigid. Due to the lubrication selection, a combination of oil and grease, the friction coefficient was assumed to be almost close to zero. To reduce the computation time, the blank sheet mesh was considered to be a shell element with five integration points, whereas the punch tool was also assumed to be a shell element with the same number of integration points. As shown in Figure 5.4a,b, the cross-section coordinates were compared among the CAD data, test data, and numerical simulation data. We confirmed that the models had free edge bending close to the start of the forming location, as magnified in the comparison plots, due to lack of extra support at the location and the material adaptability to punch force. The free bending can be

observed in detail in the scanned contours (Figure 5.4a,b, red color regions close to initial forming location). The same procedures were followed for the other tested samples, and the data of final thickness, forming height, forming angle, and average surface roughness were collected for performing the statistical analysis to build a regression model of grey relational grade.

$$\begin{aligned} \text{GRG} = & 0.6399 + 0.0004 x_1 + 0.0356 x_2 + 0.0369 x_3 - 0.0146 x_1^2 - 0.0463 x_2^2 \\ & + 0.0190 x_3^2 + 0.0369 x_1 x_2 + 0.0129 x_2 x_3 - 0.0078 x_3 x_1 \quad (5.5) \end{aligned}$$

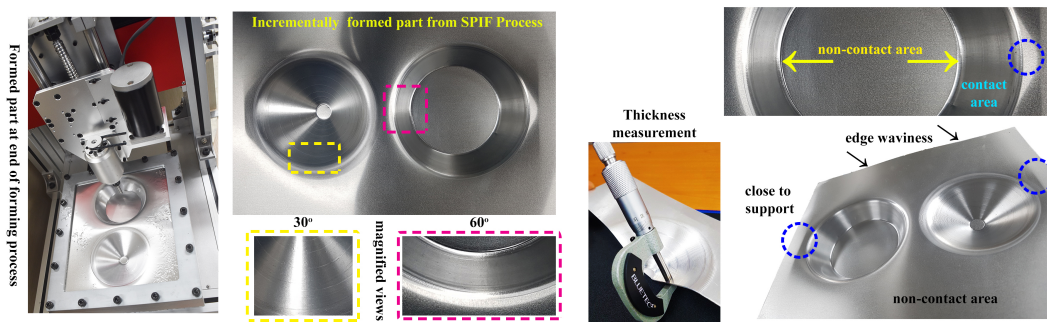


FIGURE 5.3: Incrementally formed truncated conical shape parts and thickness measurement.

The multilinear regression model with linear, square, and interaction effects was chosen for developing the prediction model of GRG values using Table 5.8. The obtained prediction model with the model coefficients is presented in Eq. (5.5). The achieved regression model was further numerically validated. Statistical metrics for verification were assessed and are compiled in Table 5.9. The prediction model's capability in  $R^2$  was computed as 0.8931, indicating that the fitted regression model adequately aligned with the estimated GRG data. An  $R^2$  value of 0.8931 indicated that the input parameter's variance explained 89.31% of the response variable's variance. As shown in Table 5.9, the adjusted- $R^2$  values were quite close to  $R^2$ , but slightly less, typically occurring as the number of input factors increases. Other statistical parameters, such

as RMSE and AARE, were estimated as 0.0196 and 2.78%, respectively, proving the overall closeness of the proposed regression model to the measured data. Apart from the numerical metrics, graphical verification was performed, as shown in Figure 5.5a,b. The relationship plot (Figure 5.5a) provides visual information about how the predicted data were distributed around the best fit line; we clearly observed that the predicted samples laid very close to the fitted regression line. The residual plot was constructed based on the differences between the measured and predicted data, as illustrated in Figure 5.5b. Figure 5.5b shows that the residual population followed the random pattern, which proved the usefulness of the proposed empirical model; the residual data fell close to the zero error line, except for a few outliers. However, the error range was identified to be between  $-0.05$  and  $0.05$ , which is significantly lower. The histogram plot of the residuals was constructed (Figure 5.5b, inset image) and we found that the residual data were distributed normally in the design space with variance and mean of 3.3748 and  $-0.1232$ , respectively.

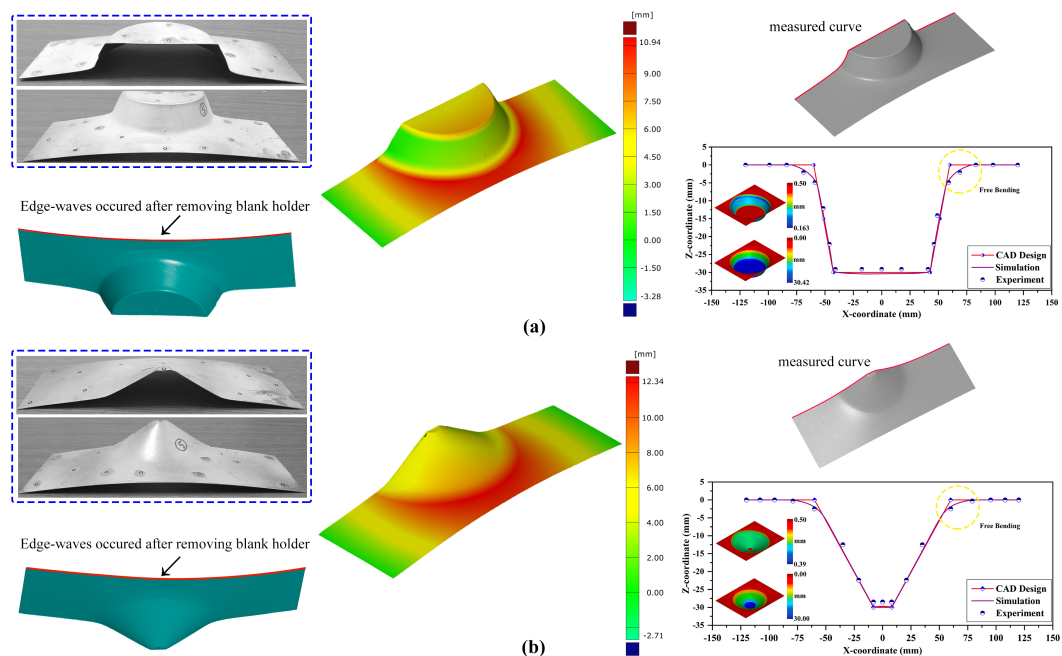


FIGURE 5.4: Estimated shape error using the ATOS 3D scanner. (a)  $60^\circ$ ; (b)  $30^\circ$ .

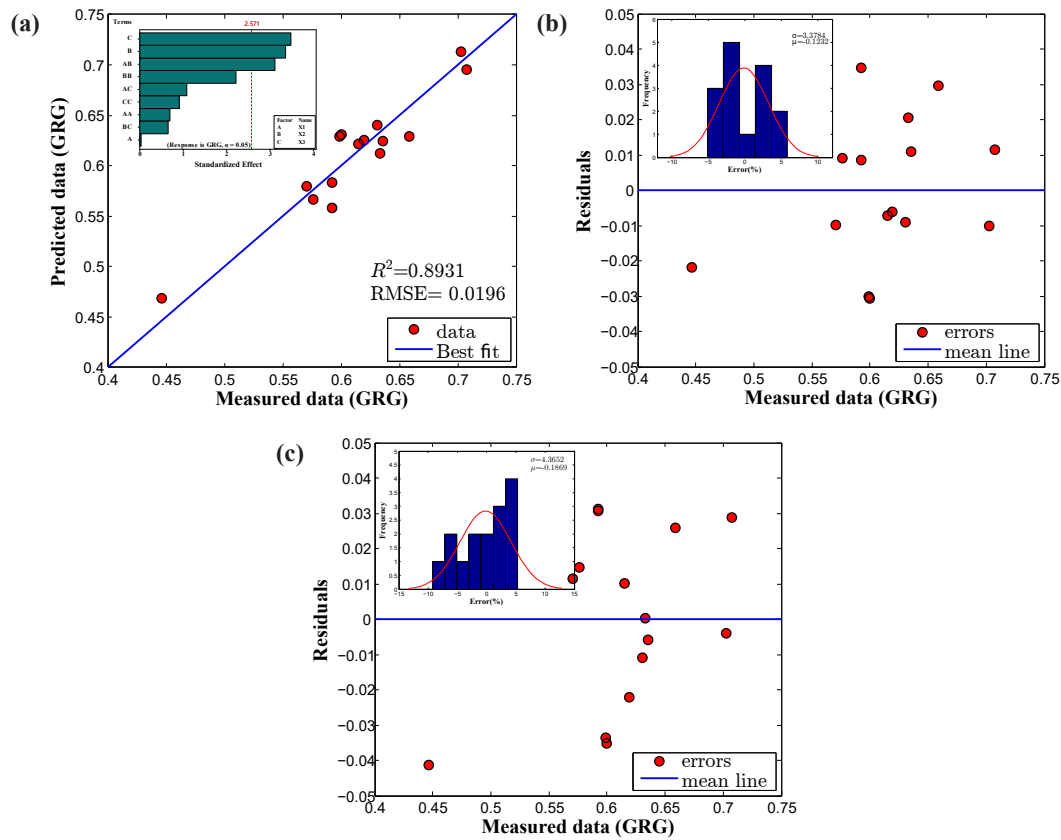


FIGURE 5.5: Full model. (a) correlation plot; (b) residual plot; (c) residual plot of reduced model.

Analysis of variance (ANOVA) results for the proposed prediction model are listed in Table 5.9. The proposed model F-value was found to be 4.64 (GRG), indicating that the developed model is statistically significant overall in terms of the process parameters: feed rate, vertical step-size, and tool radius. A  $p$ -value less than 0.05 indicates the importance of the forming parameters that influence the response variable (the grey relational grade.) The model terms  $X_2$  (0.020),  $X_3$  (0.018), and  $X_1X_2$  (0.026) were found to be significant as they had  $p$ -values less than 0.05, while the other terms were found to be insignificant. Besides the  $p$ -value, another statistical parameter, the F-value, was found to be 11.30 ( $X_2$ ), 12.16 ( $X_3$ ), and 9.72 ( $X_1X_2$ ), showing the importance of the computed model terms. The proposed model contributed

TABLE 5.9: Analysis of Variance (ANOVA) table for GRG values.

Source	DF	Adj SS	Adj MS	F-value	p-value	Contribution (%)
Model	9	0.0468	0.0052	4.64	0.053	<b>89.299</b>
Linear Terms	3	0.0263	0.0088	7.82	0.025	50.212
X1	1	0.0000	0.0000	0.00	0.972	0.004
X2	1	0.0127	0.0127	11.30	<b>0.020</b>	24.188
X3	1	0.0136	0.0136	12.16	<b>0.018</b>	26.022
Square Terms	3	0.0078	0.0026	2.31	0.194	14.826
X1 × X1	1	0.0006	0.0006	0.49	0.515	1.049
X2 × X2	1	0.0055	0.0055	4.91	0.078	10.501
X3 × X3	1	0.0009	0.0009	0.83	0.405	1.769
Interaction Terms	3	0.0127	0.0042	3.78	0.093	24.259
X1 × X2	1	0.0109	0.0109	9.72	<b>0.026</b>	20.800
X1 × X3	1	0.0013	0.0013	1.18	0.327	2.524
X2 × X3	1	0.0005	0.0005	0.44	0.538	0.937
Error	5	0.0056	0.0011			<b>10.701</b>
Total	14	0.0524				
S=0.0335		R <sup>2</sup> =89.30%		Adj.R <sup>2</sup> =70.04%		

89.29% to capturing the response variable in the design space, while the model error was computed to be 10.7%. In detail, the model terms  $X_2$ ,  $X_3$ ,  $X_2X_2$ , and  $X_1X_2$  contributed 24.18%, 26.02%, 10.50%, and 20.80%, respectively, more than the other model terms.

To examine the influence of the input parameters on the response, the average response of each level input factor is calculated and plotted using the line graph. If the estimated data points form a horizontal line, then there is no main effect. Conversely, if the plotted data points represent positive or negative deflection to the horizontal line, then the main effect is presented in the regression model (Bharath, Manjunatha, and Santhosh, 2019). To investigate the main effect of the input factors on the grey relational grade, the graphical illustration of the proposed regression model, i.e., 2D line plot, was used, as shown in Figure 5.6a, and the

computed GRG values are presented in Table 5.10. Figure 5.6a depicts that the model terms  $X_1$  (tool radius) and  $X_2$  (step-size) provided a combination of positive and negative responses on the output variable. In detail, the GRG value increased with the tool radius,  $X_1$ , up to 2.5 mm, and then decreased to 3.0 mm; similarly, it increased linearly with the step size,  $X_2$ , up to 0.5 mm, and then dropped to 0.8 mm. However, the model term  $X_3$  (feed rate) showed an entirely positive response and was identified as the most significant parameter, whereas the model term  $X_2$  (step size) was chosen as the second most important parameter that influenced the response. Table 5.10 provides the ranking information about the input parameter's influences on the response.

TABLE 5.10: Main effects of considered parameters on mean GRG values.

$X_1$	GRG	Rank	$X_2$	GRG	Rank	$X_3$	GRG	Rank
2.0	0.6030		0.2	0.5615		1000	0.5732	
2.5	0.6290	3	0.5	0.6416	2	2000	0.6155	1
3.0	0.6038		0.8	0.6327		3000	0.6417	

TABLE 5.11: Interaction effects of the selected parameters on mean GRG values.

$X_1X_2$	0.2	0.5	0.8	$X_2X_3$	1000	2000	3000	$X_3X_1$	2.0	2.5	3.0
2.0	0.5881	0.5927	0.5193	0.2	0.5112	0.6149	0.6144	1000	0.5732	0.6149	0.5525
2.5	0.6356	0.651	0.6194	0.5	0.5927	0.6286	0.599	2000	0.6356	0.6075	0.6194
3.0	0.6017	0.599	0.6806	0.8	0.5961	0.7074	0.6679	3000	0.6166	0.7074	0.6474

The interaction plots are used here to represent how the relationship between one process parameter and a response variable, the mean GRG value, depends on the second process parameter value. The computed GRG values are summarized in Table 5.11. For example, Figure 5.6b displays the mean GRG for the levels of one process parameter on the  $x$ -axis and a separate line for each level of another process parameter. The plotted lines in Figure 5.6b were evaluated in detail to explain and

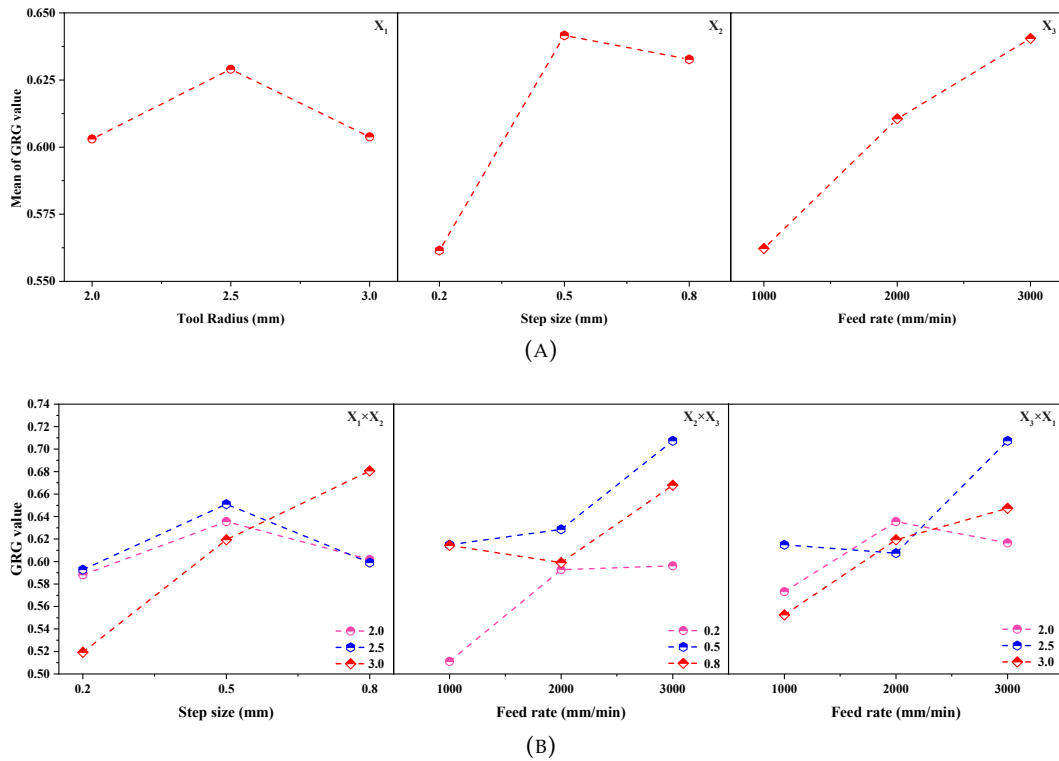


FIGURE 5.6: Process parameters vs. GRG values: (a) main effects; (b) interaction effects.

understand how the interactions affect the relationship between the input factors and the response (mean GRG value). The plotted lines can be interpreted using two options: parallel lines, which mean there is no interaction between input factors and response; and nonparallel lines, in which an interaction occurs among the input factors and response. For example, if more nonparallel lines are identified, then the interaction strength is more significant. In this interaction plot (Figure 5.6b), the lines are not parallel for the model terms  $X_1$  and  $X_2$ . This interaction effect indicated that the relationship between step size and mean GRG value depended on the tool radius value. For example, if a step-size of 0.8 mm is considered, a tool radius of 3.0 mm is associated with the highest mean GRG value. Conversely, in Figure 5.6b, the lines are almost parallel for the model terms  $X_2$ ,  $X_3$ , and  $X_3X_1$ , indicating no relationship among them on the response variable. As the interaction effects were significant in



the model term  $X_1 X_2$ , the main effects cannot be interpreted without acknowledging the interaction effects of the  $X_1$  and  $X_2$  factors. Even though the plots represent the interaction effect, other statistical parameters in the ANOVA test have to be evaluated to confirm the effect's statistical significance. From the ANOVA results in Table 5.9, the developed regression model's F-value, and  $p$ -value of interaction term  $X_1 \times X_2$  are 9.72 (GRG) and 0.026 (GRG) ( $<0.05$ ), respectively, showing that the interaction effect of  $X_1 \times X_2$  on the mean GRG value is statistically significant.

$$\text{GRG} = 0.6416 + 0.03561 x_2 + 0.03693 x_3 - 0.0445 x_2^2 + 0.0369 x_1 x_2 \quad (5.6)$$

TABLE 5.12: Analysis of Variance (ANOVA) table for GRG values.

Source	DF	Adj SS	Adj MS	F-value	P-value	Contribution (%)
Model	4	0.0438	0.0110	12.76	0.001	<b>83.615</b>
Linear	2	0.0263	0.0132	15.32	0.001	<b>50.210</b>
X2	1	0.0127	0.0127	14.76	0.003	24.188
X3	1	0.0136	0.0136	15.88	0.003	26.022
Square	1	0.0066	0.0066	7.69	0.020	<b>12.605</b>
X2*X2	1	0.0066	0.0066	7.69	0.020	12.605
2-Way Interaction	1	0.0109	0.0109	12.69	0.005	<b>20.800</b>
X1*X2	1	0.0109	0.0109	12.69	0.005	20.800
Error	10	0.0086	0.0009			<b>16.385</b>
Total	14	0.0524				
S=0.02931		$R^2=83.62\%$		Adj. $R^2=77.06\%$		

Model reduction is one of the regression model strategies that allow the user to simplify a developed regression model by omitting insignificant model terms using ANOVA results. The advantage of model reduction is that terms reduction can make the model easier to working with; notably, sometimes, omitting insignificant terms can decrease model accuracy. In this work, Eq. (5.5) was reduced by manually eliminating insignificant model terms ( $p$ -value  $> 0.05$ ), and the remaining model terms ( $p$ -value  $<$

0.05 and 0.10 (Kumari and Gupta, 2018)) were used to build a new regression model. The reduced model is presented in Eq. (5.6). From Eq. (5.6) and Table 5.12, the model terms are perceived to be statistically significant based on each coefficient's  $p$ -value; however, the statistical parameters  $R^2$ , adjusted- $R^2$ , and RMSE showed trivial results in terms of model prediction. Besides, the proposed model was observed to be insignificant through graphical verification, such as residual and histogram plots, as the residuals were distributed randomly with too many outliers, as shown in Figure 5.5c. Eventually, the response optimizer tool was used to identify the combination of input factor settings that optimize the response (GRG value). From the optimizer, the optimal solution of the response variable, a GRG value of 0.7081, was identified using the optimum forming parameters: 3.0 mm tool radius, 0.745 mm vertical step size, and 3000 mm min<sup>-1</sup> feed rate.

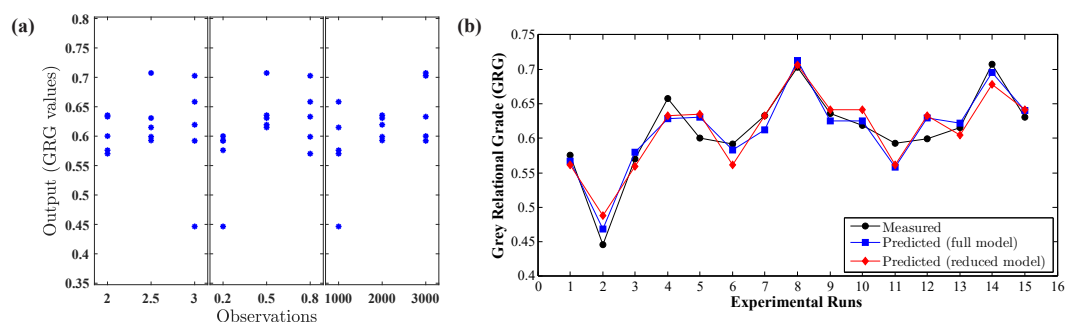


FIGURE 5.7: (a) Scatter plot of observed data; (b) Measured vs. predicted data of GRG value.

From Figure 5.7a, the sample's distribution shows that these observations were obtained from a three-level design and shows linearity. However, it reveals that the deviations occurred in the model prediction for the tested input points due to the presence of outliers; the data deviations at each level follow vertical data distribution. To represent the proposed regression model's usefulness, the measured data, GRG values, were compared against the predicted data between the full and reduced empirical models, as shown in Figure 5.7b. The observation revealed that

the predicted data fell close to the measured data (GRG values) for most observations. The reduced regression model displayed a considerable deviation in the prediction response. Overall, the statistical approach exhibited here can be used to predict the GRG values or any selected single objective for the preferred material to produce parts with better formability, surface finish, and faster machining time by thoroughly reviewing the process parameters.

## 5.8 Conclusions

we experimentally investigated the SPIF process to explore the influence of the process parameters and their contribution to improving the formability without causing a fracture by combining DOE, GRA, and ANOVA. The effect of forming process parameters in the grey relational grade was investigated using response surface methodology, adopting a central composite design with a face-centered option to model the real-time experiments. Overall, the proposed regression models were verified using numerical and graphical validations. The statistically proposed regression model was found to agree with the experimental measurements, having a higher correlation coefficient and lower prediction error. The prediction model's capability in  $R^2$  was computed as 0.8931, indicating that the fitted regression model adequately aligned with the estimated GRG data. Other statistical parameters, RMSE and AARE, were estimated as 0.0196 and 2.78%, respectively, proving the proposed regression model's overall fit with the measured data. In addition, the prediction error range was identified as being between  $-0.05$  and  $0.05$ , which is significantly lower, and the residual data were recognized as having randomness in the residuals population and the normal distribution in the design space, with variance and mean of 3.3748 and  $-0.1232$ , respectively. ANOVA was performed to understand the adequacy of the proposed model and the influence of the input factors on the

response variable. The model parameters (step size, feed rate, interaction effect of tool radius and step size) were found to favorably influence the response variable. The model terms  $X_2$  (0.020 and 11.30),  $X_3$  (0.018 and 12.16), and  $X_1X_2$  (0.026 and 9.72) were found to be significant in terms of  $p$ -value and F-value, respectively. The statistical approach presented here can be used as a guideline to understand the forming process; it will also be useful for performing the SPIF process to improve product formability for any selected material.

## Chapter 6

# Taguchi Method in Optimization of Surface Roughness

### 6.1 Summary

This chapter focuses on the influence of four forming parameters, namely, step size, spindle speed, forming tool radius, and feed rate, on the surface roughness in the SPIF process. The design of experiment method is applied to finding out the most important parameters which influence the material formability of the forming process. The optimum of forming parameters are identified using the Taguchi method. The ANOVA results prove that the vertical step has the most significant influence on the surface roughness, followed by the feed rate and the forming tool radius. The optimum level setting was received at 3.0 mm of forming tool radius (level 3), 3000 rpm of spindle speed (level 1), 0.10 mm of vertical step size (level 1), and 2000 mm/min of feed rate (level 4). Besides, confirmation experiment results showed a good agreement between the predicted and the actual data with a model error of about 1.8%. In addition, FESEM analysis is employed to examine the surface morphology of the formed parts during forming stages, including fractured and unfractured parts.

## 6.2 Introduction

Taguchi's robust design method is extensively used in the manufacturing field because of its contribution to reducing the number of experiments for obtaining the mathematical optimization models (Salehi, Saadatmand, and Mohandesi, 2012; Sivaiah and Chakradhar, 2019; Singh and Misra, 2019). Generally, the method known as the experiment's factorial design is widely used to identify all possible combinations for a given set of input factors. Since the significant factors involved in the industry is usually more and resulted in a large number of tests in the factorial designs. Because of this backlash, the investigation is limited, with few input factors for reducing the experiments. However, in this case, most of the information involved in the experimental process is not achieved. Nevertheless, later using partial fractional factorial designs are used to obtain the most information. However, it has no general guidelines for investigating the results obtained by conducting the tests. Later, this problem is sorted out by Taguchi by outlining a particular set of guidelines for factorial experiments that can be used in many real-time applications. Taguchi introduced a unique set of arrays called orthogonal arrays for producing the minimum number of experiments to get the complete information of all the working parameters that influence the performance of a selected process. This array can produce the minimum number of tests to be performed that fall in the level combinations of each input design parameter (Tondy and Tigga, 2019; Oraon, Mandal, and Sharma, 2020; Ganesh et al., 2021).

In the present work, the DOE method was used to investigate the influence of forming parameters on the surface roughness in the SPIF Process. For that purpose, the Taguchi method with L16 orthogonal array is utilized to investigate the effect of each forming parameter such as tool radius, vertical step size, spindle speed, and feed rate for optimum surface roughness. Besides, the FESEM analysis is adopted to examine the formed parts to understand the material deformation.

### 6.3 Experimental Design using Taguchi method

The literature survey identifies that the forming parameters such as step size, spindle speed, forming tool radius, and feed rate significantly influence the process and play a significant role in material formability. The variable hyperbolic cone geometry is expected to be incrementally formed with a curvature radius of 56 mm and a forming depth of 37 mm. Besides, the inner and outer radius of variable hyperbolic cone shape is 20 mm and 50 mm, respectively. The dimension of the sheet blank is  $280 \times 320 \text{ mm}^2$  with a thickness of 0.50 mm. A schematic representation of the SPIF process experimental set-up is illustrated in Figure 6.1. The four-level settings forming parameters (step size (0.10 mm–0.25 mm), spindle speed (3000 rpm–6000 rpm), forming tool radius (2.5 mm–3.0 mm), and feed rate ( $500 \text{ mm min}^{-1}$ – $2000 \text{ mm min}^{-1}$ ) are used for this study.

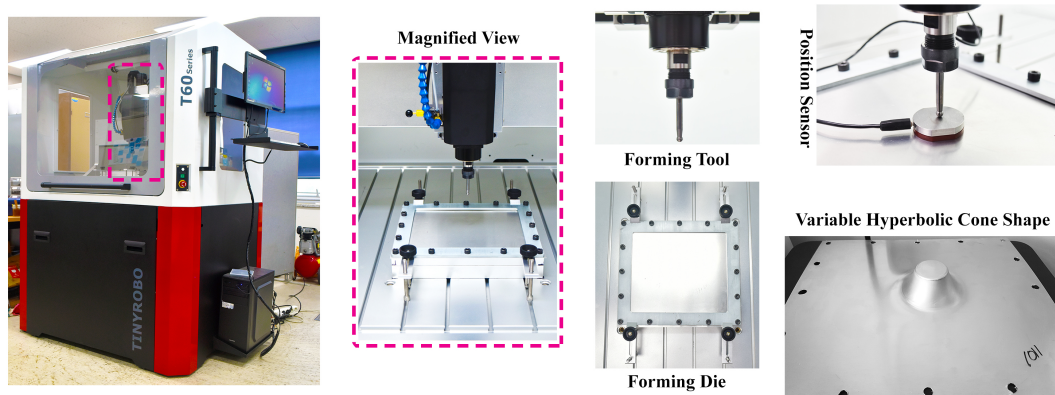


FIGURE 6.1: Experimental set-up of single-point incremental forming process.

Using this information, from available Taguchi designs, L16 orthogonal array is selected, and the independent variables are assigned to corresponding columns are tabulated in Table 6.1. For optimizing the SPIF process parameters, the surface roughness was examined. For assessing the influence of forming parameters on the response, the means and signal to noise (S/N) ratios for each control factor can

be measured. In this study, the S/N ratio was decided according to the smaller-the-better criterion to minimize the response. The S/N ratio is calculated using the smaller-the-better criterion as expressed below:

$$S/N \text{ ratio} = -10 \times \log \frac{1}{n} \sum (Y^2) \quad (6.1)$$

where,  $Y$  and  $n$  are responses for the given factor level combination and number of responses in the factor level combination, respectively.

TABLE 6.1: Experimental Design from Taguchi L16 Orthogonal Array.

Runs	TR (mm)	SS (rpm)	VS (mm)	FR (mm/min)	Roughness ( $\mu\text{m}$ )	S/N ratio
1	R2.5	3000	0.10	500	0.450	6.936
2	R2.5	4000	0.15	1000	0.533	5.465
3	R2.5	5000	0.20	1500	0.503	5.969
4	R2.5	6000	0.25	2000	0.538	5.384
5	R3.0	3000	0.15	1500	0.397	8.024
6	R3.0	4000	0.10	2000	0.323	9.816
7	R3.0	5000	0.25	500	0.847	1.442
8	R3.0	6000	0.20	1000	0.740	2.615
9	T3.0	3000	0.20	2000	0.405	7.851
10	T3.0	4000	0.25	1500	0.598	4.466
11	T3.0	5000	0.10	1000	0.453	6.878
12	T3.0	6000	0.15	500	0.517	5.730
13	T2.5	3000	0.25	1000	0.957	0.382
14	T2.5	4000	0.20	500	0.842	1.494
15	T2.5	5000	0.15	2000	0.510	5.849
16	T2.5	6000	0.10	1500	0.395	8.068

TR: Tool Radius, SS: Spindle Speed, VS: Vertical Step-size, FR: Feed Rate

Figure 6.2 depicts the effect of forming parameters on the surface roughness. From Figure 6.2, it is observed that surface roughness decreases with a reduction in the vertical step size. This is because of the smooth close movement between the forming tool and the sheet blank during the forming process. Similarly, the lower surface roughness is identified at a rise in the feed rate; as the feed rate is higher, the



forming tool motion is quick with respect to the sheet blank, and it does not stay too long at one place. Likewise, the minimum surface roughness is occurred when the forming radius is higher; as the forming tool radius is higher, the contact area between the tool and the blank is more eminent and causes the smooth material deformation.

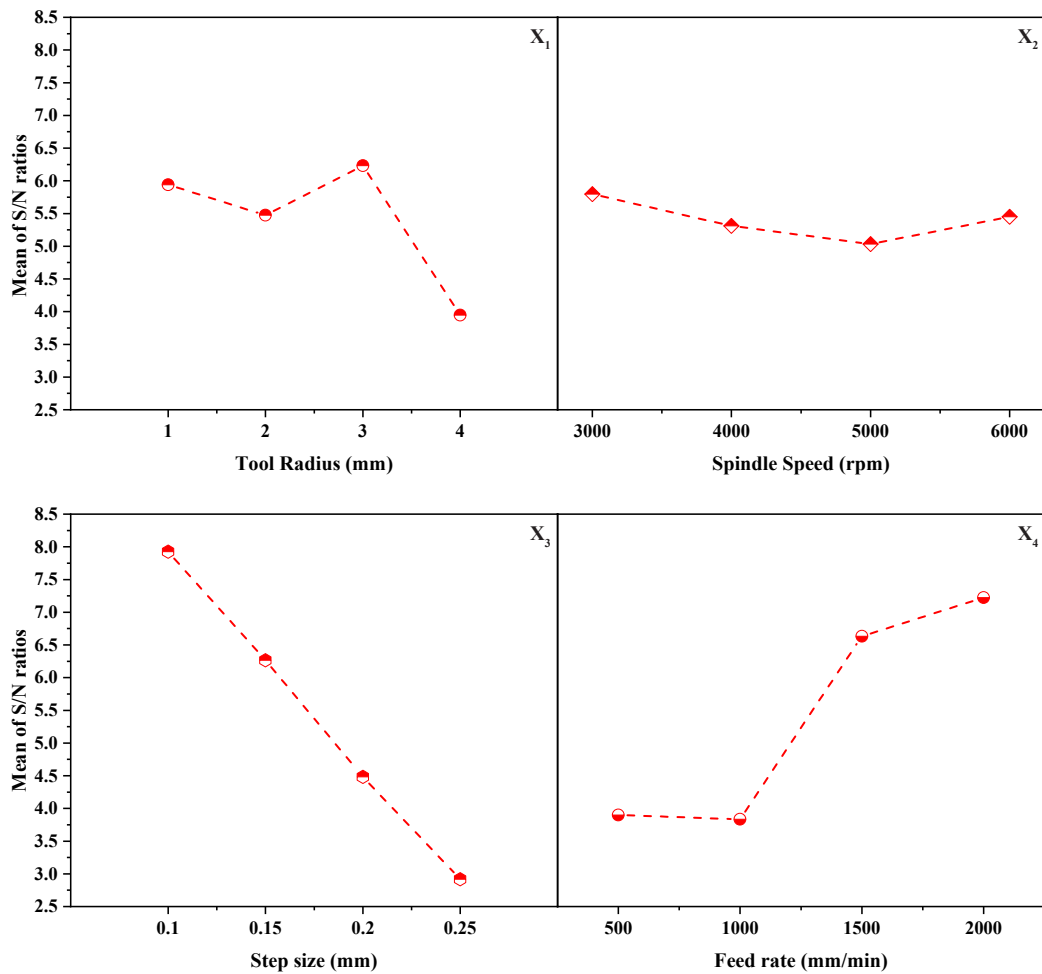


FIGURE 6.2: Main Effects Plot of S/N ratios.

The accomplished average surface roughness values are transformed into mean and S/N ratio. The test results and estimated mean and S/N ratio values are listed in Table 6.1. The computed mean response and S/N ratio of surface roughness for

each forming parameter for all levels are tabulated in Table 6.2. Response table of means and signal to noise ratios support recognizing the best combination of input factor level settings that collectively optimize a selected response. According to the highest values of the S/N ratio and mean levels (Table 6.2), it can be concluded that minimum surface roughness could be accomplished when the vertical step size is smaller, the feed rate is high, and the punch tool radius is high. The optimum level setting was received at 3.0 mm of forming tool radius (level 3), 3000 rpm of spindle speed (level 1), 0.10 mm of vertical step size (level 1), and 2000 mm/min of feed rate (level 4).

TABLE 6.2: Main effects of process parameters (means and S/N ratio) for surface roughness

Levels	Mean				S/N Ratio			
	A	B	C	D	A	B	C	D
1	0.5060	0.5523	0.4053	0.6640	5.939	5.798	7.924	3.901
2	0.5767	0.5740	0.4893	0.6708	5.474	5.310	6.267	3.835
3	0.4933	0.5783	0.6225	0.4733	6.231	5.034	4.482	6.632
4	0.6760	0.5475	0.7350	0.4440	3.948	5.449	2.919	7.225
Delta	0.1827	0.0308	0.3297	0.2268	2.283	0.764	5.006	3.390
Rank	3	4	1	2	3	4	1	2

TABLE 6.3: Analysis of variance for means (surface roughness)

Source	DF	Adj SS	Adj MS	F-Value	P-Value	
A	3	0.084288	0.028096	33.42	0.008	significant
B	3	0.002837	0.000946	1.13	0.463	non-significant
C	3	0.253794	0.084598	100.63	0.002	significant
D	3	0.176108	0.058703	69.83	0.003	significant
Error	3	0.002522	0.000841			
Total	15	0.519550				

After the optimum condition was observed, the optimum representation of the surface roughness under the optimum conditions was determined. As a result, the

TABLE 6.4: Analysis of variance for S/N ratio (surface roughness)

Source	DF	Adj SS	Adj MS	F-Value	P-Value	
A	3	12.379	4.1263	10.69	0.041	significant
B	3	1.211	0.4036	1.05	0.486	non-significant
C	3	56.498	18.8326	48.78	0.005	significant
D	3	38.179	12.7264	32.96	0.009	significant
Error	3	1.158	0.3861			
Total	15	109.425				

optimum value of the surface roughness is calculated as follows:

$$\begin{aligned}
 T &= \sum_{i=1}^n \frac{y_i}{n} \\
 &= \sum_{i=1}^{16} \frac{y_i}{n} \\
 &= \frac{(y_1 + y_2 + \dots + y_{16})}{16} \\
 &= 0.563 \mu\text{m}
 \end{aligned}$$

$$\mu = T + (\bar{R}_{\text{TR3}} - T) + (\bar{R}_{\text{SS1}} - T) + (\bar{R}_{\text{VS1}} - T) + (\bar{R}_{\text{FR4}} - T)$$

$$\mu = 0.2058 \mu\text{m}$$

where  $\mu$  is the surface roughness;  $T$  is the overall mean of surface roughness; TR3 is the average roughness at the third level of forming radius (3.0 mm); SS1 is the average roughness at the first level of spindle speed (3000 rpm); VS1 is the average roughness at the first level of vertical step-size (0.10 mm); FR4 is the average roughness at the fourth level of feed rate (2000 mm/min).

The last step in the DOE procedure is to perform confirmation tests for the optimal parameters identified. As described earlier, the optimum configuration was concluded to be TR3, SS1, VS1, and FR4. The optimal level settings are used to conduct the SPIF experiments, and the average surface roughness was determined to be  $0.202 \mu\text{m}$ . From the comparison, it is clear that there is a good agreement between

the predicted and actual data with the model error of about 1.8%. The primary objective of the ANOVA is to recognize the influence of specific process factors on the response. ANOVA results clearly identify the influence of each forming factor on the surface roughness. The ANOVA statistics for both mean and S/N ratio is computed and summarized in Table 6.3 and Table 6.4. The results such as P-test and F-test indicate that the vertical step size significantly influences surface roughness followed by feed rate, forming tool radius. Besides, the spindle speed is identified to have no significant impact on the surface roughness.

## 6.4 Microstructure Evaluation of AA5052-H32 material in SPIF Process

The FESEM (MIRA3 TESCAN, Secondary electron detector, Jeju National University, Jeju-si, South Korea) set-up was used to investigate the surface morphology. Stretching behavior occurs during the single-point incremental forming (SPIF) process, producing pyramid geometry, as shown in Figure 6.3a. Here, the stretching or elongation of the AA3003 material sheet during the SPIF process depended on the various working factors such as tool radius (3 mm), feed rate ( $1000 \text{ mm min}^{-1}$ ), forming depth (40 mm), spindle speed (5000 rpm), and step-size (0.25 mm). Figure 6.3a(iii) presents the desired pyramid-shaped product using AA3003 material, showing multiple regions; the flat (pristine and marked as 4), bending, and stretching locations (marked as 2 and 3, respectively) confirmed the variations in the punch tool path, friction, and material ductility.

During the initial state, the punch tool did not interact with the AA3003 sheet and the corresponding surface morphology was smooth: no stretched or elongated regions were observed, as shown in Figure 6.3b(i). A similar surface morphology was observed during the final stage of the SPIF process of creating pyramid geometry,

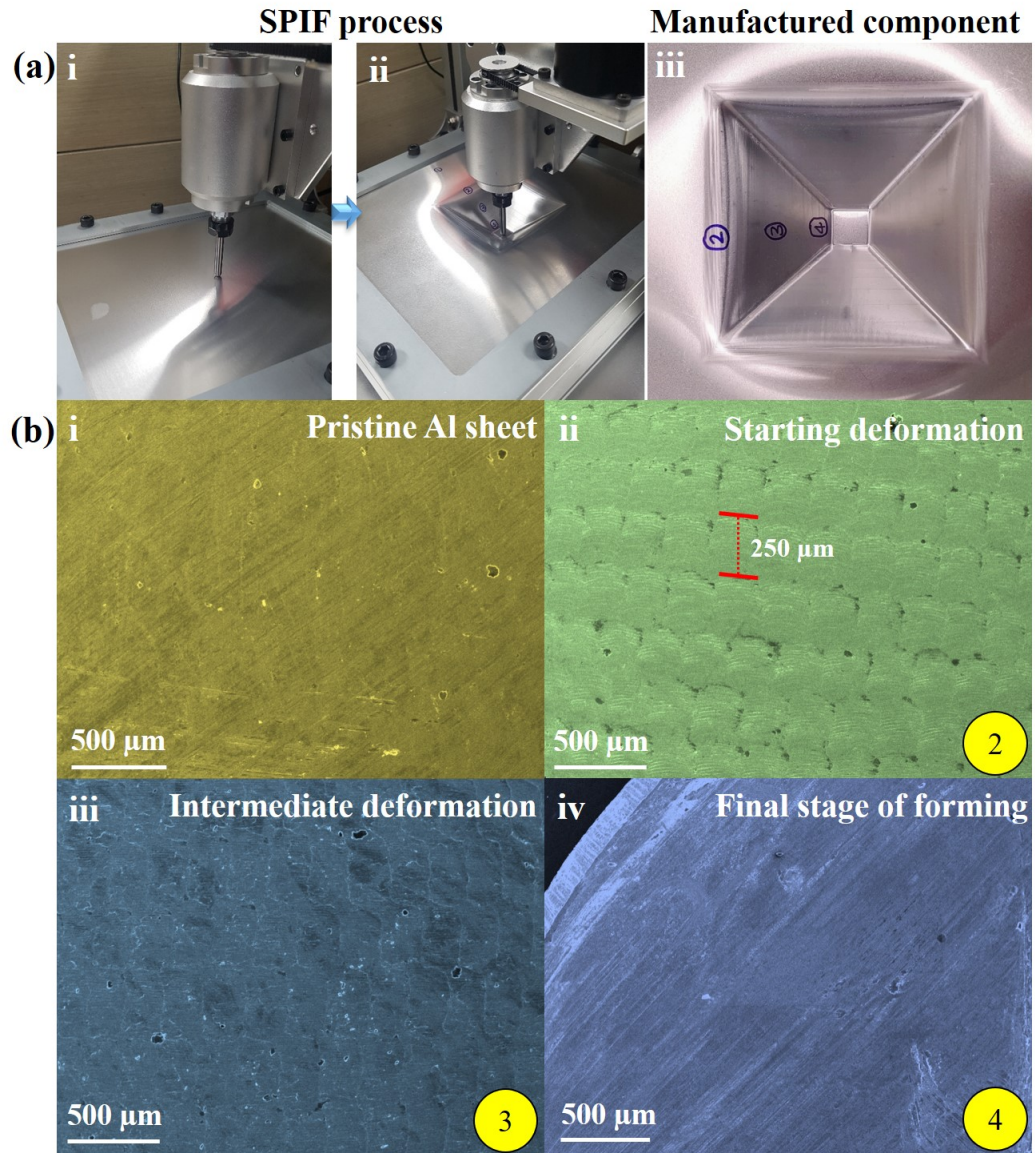
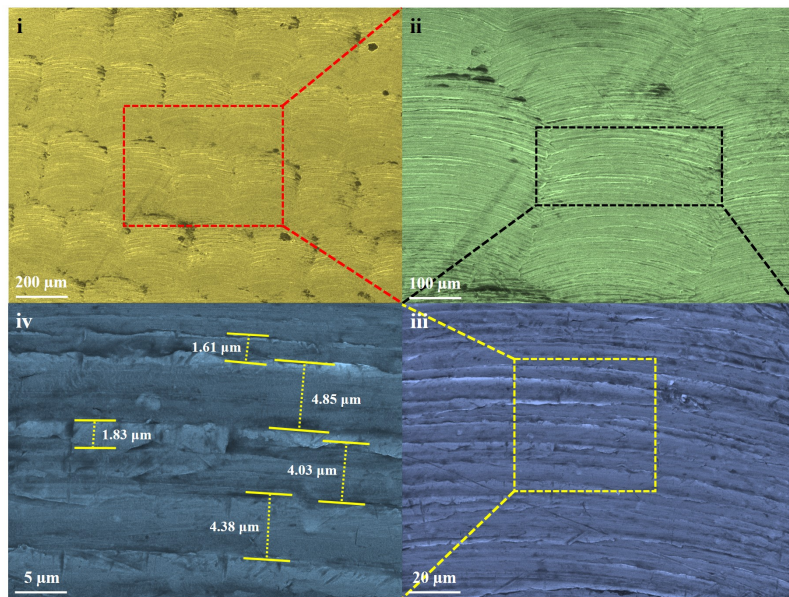


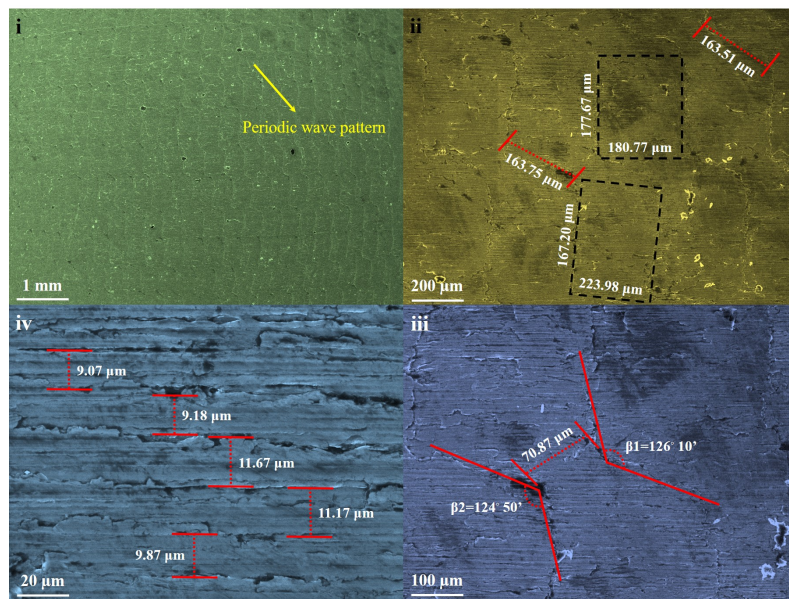
FIGURE 6.3: (a) SPIF process illustration and final part; (b) microstructure of aluminum alloy (AA3003) material at various forming stages, observation by FESEM at 500  $\mu\text{m}$  magnification.

as shown in Figure 6.3b(iv). However, in the case of regions 2 and 3, different types of periodic stretching regions formed on the AA3003 sheet due to the defined step-size (250  $\mu\text{m}$ ) of the punch tool movements in the SPIF process to create the pyramid shape, as shown in Figure 6.3b(ii,iii). Here, the magnification scale of all the FESEM





(A)



(B)

FIGURE 6.4: Microstructure observation of aluminum alloy (AA3003) material by FESEM at various magnifications at: (a) location 2; (b) location 3.

images is 500  $\mu\text{m}$  and regions 2 and 3 are interesting due to the differences in the nature of the stretching/bending (or thinning locations) of the AA3003 sheet.

Figure 6.4a(i–iv) shows that the initial stretching of the AA3003 sheet is similar to the woven shaped morphology with a uniform step size and periodic nature. In Figure 6.4a(ii), the marked location shows the formation of multiple stackings of aluminum strips, and the magnified images (Figure 6.4a(iii,iv)) depict the linear arrangement of the strips, having an average width of 4.42 and 1.72  $\mu\text{m}$ , respectively. Figure 6.4b(i–iv) shows that the surface morphology of the intermediate deformation of the pyramid sheet produced through the SPIF process is similar to the periodic wavy pattern shape constructed by the stackings of the multiple rectangular boxes, having a uniform area. The magnified image demonstrates the length, width, and order of the interfacial region between the rectangular box, as shown in Figure 6.4b(ii). The deformation of the aluminum sheet with respect to the angle ( $\approx 125^\circ$ ) and distance (70.87  $\mu\text{m}$ ) between the rectangular boxes similarly confirms the deformation process was homogeneous, as shown in Figure 6.4b(ii,iii). The rectangular box formed by the periodic arrangement of linear strips with an average width of 10.19  $\mu\text{m}$ , as shown in Figure 6.4b(iv). Here, there was more stretching (or thinning) of aluminum compared to the deformation of region 2 (Figure 6.4b(iv)). However, no failure conditions were experienced during the SPIF process of forming the pyramid geometry at the pre-defined forming depth and testing conditions.

## 6.5 Microstructure Evaluation of AA3003-H18 material in SPIF Process

The incrementally produced part's external surface (tool contact region) using a lubricant combining oil and grease was examined using FESEM pictures, as depicted in Figure 6.5a. Figure 6.5a, depicting the magnified SEM images at 20, 50, and 100  $\mu\text{m}$ , shows that the surface tended to have a uniform deformation during

the forming process; because of this observation, the smooth transition between the forming tool and the blank was presumed. Figure 6.5b,c illustrates the scanned surfaces of the formed samples at magnification levels of 10, 20, 50, and 100  $\mu\text{m}$ . Figure 6.5b shows the apparent association of forming paths due to the punch tool movement along the blank with the predefined vertical step size for 60° truncated conical shape geometry. As the magnification levels increased (Figure 6.5b), at 10 and 20  $\mu\text{m}$ , the insets show that a uniform region was observed to have irregular micro-cracks between the forming path lines. This response occurred due to the thinning that occurs during the forming process; if more thinning occurs, it might lead to a fracture in the test sample.

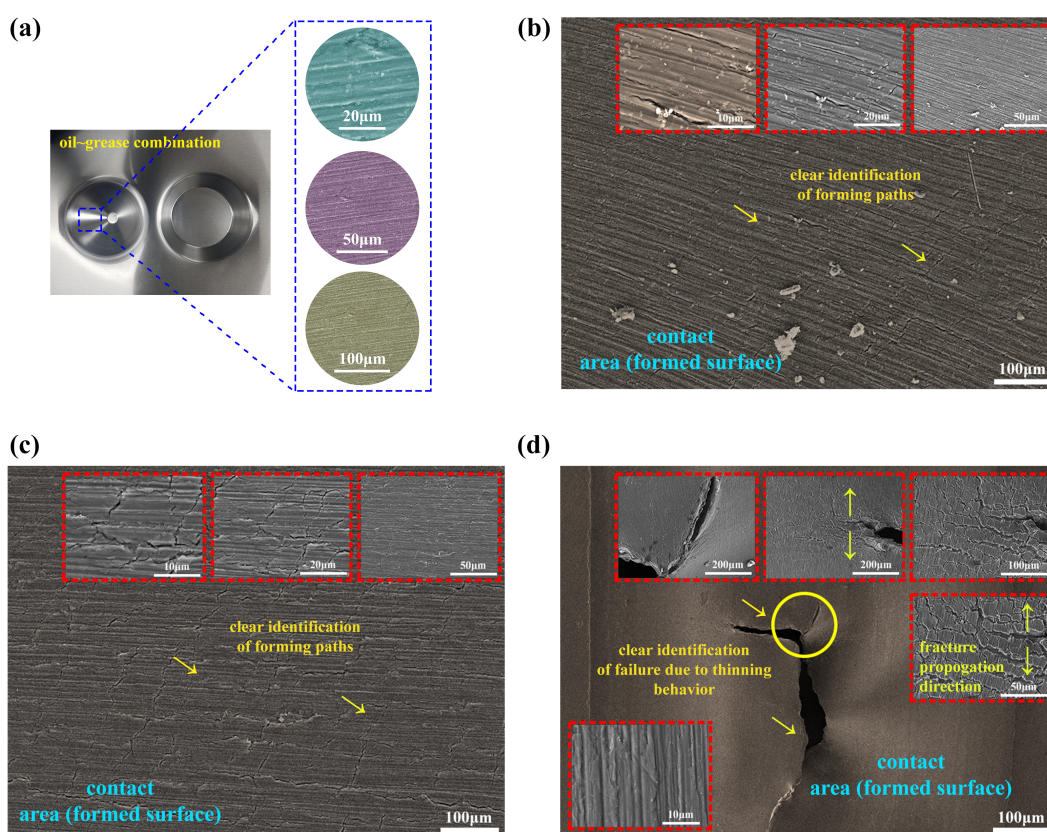


FIGURE 6.5: FESEM images at various magnifications: (a) surface from oil-grease lubricant used; (b) unfractured scanned surface from 60° part; (c) unfractured scanned surface from 30° part; (d) fractured surface.



Similarly, in Figure 6.5c, the same kind of consistent homogeneous deformation response is observed in the scanned surface at 100  $\mu\text{m}$  by identifying forming paths. However, the scanned surface tended to have more irregular micro-cracks all over the surface, and the vertical step size was usually responsible for these micro-cracks observations. The insets in Figure 6.5c depict the scanned surface's amplified images at 10 and 20  $\mu\text{m}$ ; from the inset images, micro-cracks can be seen more clearly. Notably, the formed part did not have any visual cracks; the cracks were only observed in FESEM photographs. However, the fractured sample from thinning failure occurrence was cut down for examining the outer (tool contact region) surface. The magnification of a fractured surface at the 100  $\mu\text{m}$  scale is depicted in Figure 6.5d. The SEM pictures of a fractured surface at higher magnifications in various regions are illustrated in Figure 6.5d (insets); the insets show that the fracture was predominantly ductile. As shown in the insets in Figure 6.5d at the 50 and 100  $\mu\text{m}$  scales, the damage concentrated due to nucleation, then slowly evolved as voids coalesced, and propagated into near regions as secondary voids coalescence. This continuous nucleation of tiny voids coalescence led to the fracture during the forming process. In conclusion, FESEM investigations are useful for understanding and observing the deformation mechanisms behind the SPIF process.

## 6.6 Conclusions

The SPIF experiments are carried out successfully using the Taguchi L16 orthogonal design. Then, the formed parts were measured for the surface roughness. The forming parameters were optimized to minimize the surface roughness in the SPIF process. At first, the signal-to-noise ratios according to the smaller-the-better are calculated to make a response table for obtaining the optimum level of process parameters. Minimum surface roughness was achieved when the vertical step size is

smaller, the feed rate is high, and the punch tool radius is high. The optimum level setting was received at 3.0 mm of forming tool radius (level 3), 3000 rpm of spindle speed (level 1), 0.10 mm of vertical step size (level 1), and 2000 mm/min of feed rate (level 4). The ANOVA results such as P-test and F-test showed that vertical step size, feed rate, and forming tool radius significantly influences surface roughness. On the other hand, the spindle speed was observed to have no significant impact on the surface roughness. The prediction from the Taguchi design showed a good agreement with the test data with a model error of about 1.8%. The micro-structural inspection showed that the thinning behavior tended to increase as forming depth reached its maximum; the deformation was also seen to be uniform and homogeneous under the predefined test conditions.

## Chapter 7

# Conclusions and Future Work

### 7.1 Conclusions

This chapter outlines the general thesis conclusions and possible future directions of this research work.

- In Chapter 1, The incremental forming methods, involving the fundamentals and modeling procedures, have been comprehensively studied. In addition, the importance of process parameters has been identified from the literature survey for proposing mathematical models. Afterward, a systematic approach for the lubrication selection is included. Moreover, the material properties at room temperatures have been computed systematically for conducting the metal forming simulations. Furthermore, the stress-strain data obtained from the hot tensile tests were used for proposing the constitutive models. Finally, the micro-structure evaluations were performed on the test samples to represent the material deformation behavior before and after the failure.
- In chapter 2, the Johnson-Cook material and damage models have been proposed for describing the material behavior at elevated temperatures (650–950 °C) and strain rates (0.05–1.0 s<sup>-1</sup>) for AISI 1045 medium carbon steel. The

model prediction error was minimized by employing the nonlinear programming solver *fmincon*-based optimization procedure. The proposed model was evaluated using the statistical metrics  $R^2$  (0.4836) and AARE (17.6112%). Overall, the computed results from the optimized JC model displayed more favorable agreement with the experimental measurements than those of the conventional method.

- In chapter 3, similarly, the flow stress models, namely, modified JC and modified ZA models, have been developed to confirm the model predictability for AISI-1045 steel at the same test conditions. The modified ZA model was identified to be significant in terms of the predictions compared with the modified JC model. Besides, the statistical measures were also indicated the model adequacy in terms of  $R^2$  (0.9364) and AARE (9.9141%). The inadequacy reason was due to the improper estimation of exponent term, thermal softening, in the modified JC model. However, the modified ZA model could predict the deformation behavior much more accurately than the modified JC model even against random experiments.
- In chapter 4, likewise, the flow stress models such as Arrhenius-type constitutive equation and ANN-BP model have been proposed for capturing the material behavior of AISI-1045 steel material. The prediction results comparison proved that the modified constitutive equation captured the material flow behavior more precisely with the numerical numbers estimated as 0.9894 ( $R^2$ ) and 2.9840% (AARE), respectively. Subsequently, the best trained ANN-BP model with tansigmoid activation function showed much more precise prediction on the material behavior throughout the entire experimented conditions. Furthermore, the statistical measures such as  $R^2$  and AARE, were determined as 0.9989 and 1.1229%, respectively. Overall, the ANN-BP model

outweighed all available constitutive models in terms of the material flow behavior prediction.

- In chapter 5, the SPIF process has been investigated to examine the impact of the forming parameters and their contribution for enhancing the material formability without causing a fracture by combining DOE, GRA, and ANOVA. The computed grey relational grade was examined using response surface methodology. The statistically proposed regression model was observed to agree with the experimental estimations, having a higher  $R^2$  (0.8931) with lower prediction error (2.78%). In addition, ANOVA was made to recognize the model adequacy and the influence of the input factors on the response. The process parameters (step size ( $X_2$  (0.020 and 11.30)), feed rate ( $X_3$  (0.018 and 12.16)), interaction effect of tool radius, and step size ( $X_1 X_2$  (0.026 and 9.72)) positively influenced the response variable. The statistical approach manifested here can be utilized as a guideline to explain the forming process; it will also help perform the SPIF process to enhance formability for any chosen material.
- In chapter 6, the SPIF experiments have been performed using the Taguchi L16 orthogonal design for variable hyperbolic cone geometry. The input factors were optimized to minimize the surface roughness of formed parts. Firstly, according to the smaller-the-better, the S/N ratios are estimated to make a response table for getting the optimum level of process parameters. Minimum surface roughness was accomplished when the vertical step-size is smaller, the feed-rate is high, and the forming tool radius is high. The optimum level setting was acquired at 3.0 mm of forming tool radius (level 3), 3000 rpm of spindle speed (level 1), 0.10 mm of vertical step size (level 1), and 2000 mm/min of feed rate (level 4). The ANOVA results such as P-test and F-test

revealed that vertical step-size, feed-rate, and tool radius significantly affect surface roughness. In contrast, the spindle speed was witnessed to have no significant influence on surface roughness. The Taguchi design results conferred better agreement with the experimental measurements with moderate model error ( $\approx 1.8\%$ ). Besides, the micro-structural evaluation revealed that the thinning behavior tended to increase as forming depth reached its maximum; the material deformation was also observed to be uniform and homogeneous.

## 7.2 Suggestions for the Future Work

Many experiments and numerical models have been left for the future due to a lack of experimental setup (i.e., finite element simulations with accurate data are usually very time-consuming, requiring even days to finish a single run). Future research concerns more profound investigation of failure mechanisms, new proposals to try different mathematical models for a specific outcome (i.e., thickness prediction), or simply curiosity to understand the ISF process under various forming conditions. There are some ideas that I would like to try near future. Thus, this dissertation work can be extended into the following new research directions.

- Toolpath Strategies: The toolpath strategy is the most critical process parameter that impacts the ISF process. So, to improve the surface finish, formability, thinning behavior, geometric accuracy, and processing time, the toolpath strategies could be optimized for obtaining the expected outcome.
- Forming Tool-design: The tool design could be modified to reduce the machining time. However, the possible design limits should be considered in order to control the accuracy. For example, if the fillet is smaller than the tool radius, there might be a fracture or improper forming in model accuracy.

- **Fracture Model:** The damage mechanism is reasonably necessary to identify the possible fracture locations and fracture limits. It could be interesting to systematize them for any selected materials.
- **Mathematical Model:** There are no standard mathematical equations for thickness prediction when various shapes are formed. It could be appealing if the equations are normalized for each shape using the surrogate modeling approach.
- **Mesh Convergence:** Finite element simulations could be modeled with a proper mesh settings for much more accurate numerical results. For that, instead of using one numerical model, a mesh convergence study has to be conducted.
- **Computational-time Reduction:** The main problem in modeling the incremental forming simulations is computation time. To solve the issues, the meshes elements have to be optimized based on forming regions (fine and coarse elements), symmetric mesh model, or the mass scaling approach, or adaptive meshing techniques, or consider only important forming regions.
- **Microstructure Investigation:** The preliminary results of the microstructure evaluation on the formed parts seem to be satisfactory. Further study is still required to understand the material behavior of any materials under different forming conditions.

# Bibliography

- Abbasi-Bani, A. et al. (2014). "A comparative study on the capability of Johnson–Cook and Arrhenius-type constitutive equations to describe the flow behavior of Mg–6Al–1Zn alloy". In: *Mechanics of Materials* 71, pp. 52–61. DOI: [10.1016/j.mechmat.2013.12.001](https://doi.org/10.1016/j.mechmat.2013.12.001).
- Ai, S. et al. (2017). "Evaluation of deformation stability and fracture mechanism in incremental sheet forming". In: *International Journal of Mechanical Sciences* 124-125, pp. 174–184. DOI: [10.1016/j.ijmecsci.2017.03.012](https://doi.org/10.1016/j.ijmecsci.2017.03.012).
- Ajay, C. Veera, C. Boopathi, and P. Kavim (2019). "Incremental sheet metal forming (ISMF): A literature review". In: DOI: [10.1063/1.5117955](https://doi.org/10.1063/1.5117955).
- Akbari, Z., H. Mirzadeh, and J. Cabrera (2015). "A simple constitutive model for predicting flow stress of medium carbon microalloyed steel during hot deformation". In: *Materials and Design* 77, pp. 126–131. DOI: [10.1016/j.matdes.2015.04.005](https://doi.org/10.1016/j.matdes.2015.04.005).
- Al-Obaidi, Amar, Verena Kräusel, and Dirk Landgrebe (2015). "Hot single-point incremental forming assisted by induction heating". In: *The International Journal of Advanced Manufacturing Technology* 82.5-8, pp. 1163–1171. DOI: [10.1007/s00170-015-7439-x](https://doi.org/10.1007/s00170-015-7439-x).
- Ambrogio, G. et al. (2004). "Influence of some relevant process parameters on the dimensional accuracy in incremental forming: a numerical and experimental investigation". In: *Journal of Materials Processing Technology* 153-154, pp. 501–507. DOI: [10.1016/j.jmatprotec.2004.04.139](https://doi.org/10.1016/j.jmatprotec.2004.04.139).



- Ashrafi, Mahdi and Mark E. Tuttle (2016). "Measurement of Strain Gradients Using Digital Image Correlation by Applying Printed-Speckle Patterns". In: *Experimental Techniques* 40.2, pp. 891–897. DOI: [10.1007/s40799-016-0090-0](https://doi.org/10.1007/s40799-016-0090-0).
- Ashtiani, H.R. Rezaei and P. Shahsavari (2016). "A comparative study on the phenomenological and artificial neural network models to predict hot deformation behavior of AlCuMgPb alloy". In: *Journal of Alloys and Compounds* 687, pp. 263–273. DOI: [10.1016/j.jallcom.2016.04.300](https://doi.org/10.1016/j.jallcom.2016.04.300).
- Aydin, Murat and Ozkan Oz (2018). "Application of digital image correlation technique to tensile test for printed pla specimens". In: *International Journal of 3D Printing Technologies and Digital Industry* 2, pp. 1–7.
- Bai, Yuanli and Tomasz Wierzbicki (2008). "A new model of metal plasticity and fracture with pressure and Lode dependence". In: *International Journal of Plasticity* 24.6, pp. 1071–1096. DOI: [10.1016/j.ijplas.2007.09.004](https://doi.org/10.1016/j.ijplas.2007.09.004).
- Banerjee, A. et al. (2015). "Determination of Johnson cook material and failure model constants and numerical modelling of Charpy impact test of armour steel". In: *Materials Science and Engineering: A* 640, pp. 200–209. DOI: [10.1016/j.msea.2015.05.073](https://doi.org/10.1016/j.msea.2015.05.073).
- Bansal, Ankush et al. (2017). "Prediction of forming forces in single point incremental forming". In: *Journal of Manufacturing Processes* 28, pp. 486–493. DOI: [10.1016/j.jmapro.2017.04.016](https://doi.org/10.1016/j.jmapro.2017.04.016).
- Bao, Yingbin (2005). "Dependence of ductile crack formation in tensile tests on stress triaxiality, stress and strain ratios". In: *Engineering Fracture Mechanics* 72.4, pp. 505–522. DOI: [10.1016/j.engfracmech.2004.04.012](https://doi.org/10.1016/j.engfracmech.2004.04.012).
- Baruah, Angshuman, C. Pandivelan, and A.K. Jeevanantham (2017). "Optimization of AA5052 in incremental sheet forming using grey relational analysis". In: *Measurement* 106, pp. 95–100. DOI: [10.1016/j.measurement.2017.04.029](https://doi.org/10.1016/j.measurement.2017.04.029).

- Behera, Amar Kumar, Bert Lauwers, and Joost R. Duflou (2014). "Tool path generation framework for accurate manufacture of complex 3D sheet metal parts using single point incremental forming". In: *Computers in Industry* 65.4, pp. 563–584. DOI: [10.1016/j.compind.2014.01.002](https://doi.org/10.1016/j.compind.2014.01.002).
- Behera, Amar Kumar et al. (2013). "Tool path compensation strategies for single point incremental sheet forming using multivariate adaptive regression splines". In: *Computer-Aided Design* 45.3, pp. 575–590. DOI: [10.1016/j.cad.2012.10.045](https://doi.org/10.1016/j.cad.2012.10.045).
- Bharath, K.N., G.B. Manjunatha, and K. Santhosh (2019). "Failure analysis and the optimal toughness design of sheep–wool reinforced epoxy composites". In: pp. 97–107. DOI: [10.1016/b978-0-08-102293-1.00005-x](https://doi.org/10.1016/b978-0-08-102293-1.00005-x).
- Bobbili, Ravindranadh, V. Madhu, and A.K. Gogia (2014). "Neural network modeling to evaluate the dynamic flow stress of high strength armor steels under high strain rate compression". In: *Defence Technology* 10.4, pp. 334–342. DOI: [10.1016/j.dt.2014.06.012](https://doi.org/10.1016/j.dt.2014.06.012).
- Bobbili, Ravindranadh, Vemuri Madhu, and Ashok Kumar Gogia (2016). "Tensile behaviour of aluminium 7017 alloy at various temperatures and strain rates". In: *Journal of Materials Research and Technology* 5.2, pp. 190–197. DOI: [10.1016/j.jmrt.2015.12.002](https://doi.org/10.1016/j.jmrt.2015.12.002).
- Brunig, Michael et al. (2008). "A ductile damage criterion at various stress triaxialities". In: *International Journal of Plasticity* 24.10, pp. 1731–1755. DOI: [10.1016/j.ijplas.2007.12.001](https://doi.org/10.1016/j.ijplas.2007.12.001).
- Buzyurkin, A.E., I.L. Gladky, and E.I. Kraus (2015). "Determination and verification of Johnson–Cook model parameters at high-speed deformation of titanium alloys". In: *Aerospace Science and Technology* 45, pp. 121–127. DOI: [10.1016/j.ast.2015.05.001](https://doi.org/10.1016/j.ast.2015.05.001).

- Cai, Jun et al. (2011). "Constitutive equations for elevated temperature flow stress of Ti-6Al-4V alloy considering the effect of strain". In: *Materials & Design* 32.3, pp. 1144–1151. DOI: [10.1016/j.matdes.2010.11.004](https://doi.org/10.1016/j.matdes.2010.11.004).
- Cai, Jun et al. (2015). "'A Modified Johnson-Cook Constitutive Equation to Predict Hot Deformation Behavior of Ti-6Al-4V Alloy'". In: *Journal of Materials Engineering and Performance* 24 (1), pp. 32–44. DOI: [10.1007/s11665-014-1243-x](https://doi.org/10.1007/s11665-014-1243-x).
- Cao, T.-S. et al. (2014a). "A Lode-dependent enhanced Lemaitre model for ductile fracture prediction at low stress triaxiality". In: *Engineering Fracture Mechanics* 124-125, pp. 80–96. DOI: [10.1016/j.engfracmech.2014.03.021](https://doi.org/10.1016/j.engfracmech.2014.03.021).
- Cao, Y. et al. (2014b). "Hot Deformation Behavior of Alloy 800H at Intermediate Temperatures: Constitutive Models and Microstructure Analysis". In: *Journal of Materials Engineering and Performance* 23.12, pp. 4298–4308. DOI: [10.1007/s11665-014-1220-4](https://doi.org/10.1007/s11665-014-1220-4).
- Chai, Rong xia, Cheng Guo, and Li Yu (2012). "Two flowing stress models for hot deformation of XC45 steel at high temperature". In: *Materials Science and Engineering: A* 534, pp. 101–110. DOI: [10.1016/j.msea.2011.11.047](https://doi.org/10.1016/j.msea.2011.11.047).
- Chang, Zhidong and Jun Chen (2019). "Analytical model and experimental validation of surface roughness for incremental sheet metal forming parts". In: *International Journal of Machine Tools and Manufacture* 146, p. 103453. DOI: [10.1016/j.ijmactools.2019.103453](https://doi.org/10.1016/j.ijmactools.2019.103453).
- (2020). "Mechanism of the twisting in incremental sheet forming process". In: *Journal of Materials Processing Technology* 276, p. 116396. DOI: [10.1016/j.jmatprotec.2019.116396](https://doi.org/10.1016/j.jmatprotec.2019.116396).
- Chang, Zhidong, Ming Li, and Jun Chen (2019). "Analytical modeling and experimental validation of the forming force in several typical incremental sheet forming processes". In: *International Journal of Machine Tools and Manufacture* 140, pp. 62–76. DOI: [10.1016/j.ijmactools.2019.03.003](https://doi.org/10.1016/j.ijmactools.2019.03.003).

- Chen, Dong-Dong et al. (2017). “Dislocation substructures evolution and an adaptive-network-based fuzzy inference system model for constitutive behavior of a Ni-based superalloy during hot deformation”. In: *Journal of Alloys and Compounds* 708, pp. 938–946. DOI: [10.1016/j.jallcom.2017.03.029](https://doi.org/10.1016/j.jallcom.2017.03.029).
- Chen, Yajun et al. (2019). “The Application of DIC Technique to Evaluate Residual Tensile Strength of Aluminum Alloy Plates with Multi-Site Damage of Collinear and Non-Collinear Cracks”. In: *Metals* 9.2, p. 118. DOI: [10.3390/met9020118](https://doi.org/10.3390/met9020118).
- Chuan, Wang, Yu Lei, and Zhang Jianguo (2014). “Study on optimization of radiological worker allocation problem based on nonlinear programming function-fmincon”. In: *2014 IEEE International Conference on Mechatronics and Automation*. IEEE. DOI: [10.1109/icma.2014.6885847](https://doi.org/10.1109/icma.2014.6885847).
- Davarpanah, Mohammad Ali et al. (2015). “Effects of incremental depth and tool rotation on failure modes and microstructural properties in Single Point Incremental Forming of polymers”. In: *Journal of Materials Processing Technology* 222, pp. 287–300. DOI: [10.1016/j.jmatprotec.2015.03.014](https://doi.org/10.1016/j.jmatprotec.2015.03.014).
- Fan, Guoqiang et al. (2008). “Electric hot incremental forming: A novel technique”. In: *International Journal of Machine Tools and Manufacture* 48.15, pp. 1688–1692. DOI: [10.1016/j.ijmachtools.2008.07.010](https://doi.org/10.1016/j.ijmachtools.2008.07.010).
- Fiorentino, A., C. Giardini, and E. Ceretti (2015). “Application of artificial cognitive system to incremental sheet forming machine tools for part precision improvement”. In: *Precision Engineering* 39, pp. 167–172. DOI: [10.1016/j.precisioneng.2014.08.005](https://doi.org/10.1016/j.precisioneng.2014.08.005).
- Gambirasio, Luca and Egidio Rizzi (2014). “On the calibration strategies of the Johnson–Cook strength model: Discussion and applications to experimental data”. In: *Materials Science and Engineering: A* 610, pp. 370–413. DOI: [10.1016/j.msea.2014.05.006](https://doi.org/10.1016/j.msea.2014.05.006).

- Gambirasio, Luca and Egidio Rizzi (2016). "An enhanced Johnson–Cook strength model for splitting strain rate and temperature effects on lower yield stress and plastic flow". In: *Computational Materials Science* 113, pp. 231–265. DOI: [10.1016/j.commatsci.2015.11.034](https://doi.org/10.1016/j.commatsci.2015.11.034).
- GAN, Chun lei et al. (2014). "Constitutive equations for high temperature flow stress prediction of 6063 Al alloy considering compensation of strain". In: *Transactions of Nonferrous Metals Society of China* 24.11, pp. 3486–3491. DOI: [10.1016/s1003-6326\(14\)63492-0](https://doi.org/10.1016/s1003-6326(14)63492-0).
- Ganesh, P. et al. (2021). "Optimization of pyramid shaped single point incremental forming of AA5052 alloy sheet". In: *Materials Today: Proceedings* 45, pp. 5892–5898. DOI: [10.1016/j.matpr.2020.08.573](https://doi.org/10.1016/j.matpr.2020.08.573).
- Gatea, Shakir et al. (2017). "Modelling of ductile fracture in single point incremental forming using a modified GTN model". In: *Engineering Fracture Mechanics* 186, pp. 59–79. DOI: [10.1016/j.engfracmech.2017.09.021](https://doi.org/10.1016/j.engfracmech.2017.09.021).
- Grażyna, Mrówka-Nowotnik et al. (2020). "Microstructure and Properties of As-Cast and Heat-Treated 2017A Aluminium Alloy Obtained from Scrap Recycling". In: *Materials* 14.1, p. 89. DOI: [10.3390/ma14010089](https://doi.org/10.3390/ma14010089).
- GUO, La feng, Bao cheng LI, and Zhi min ZHANG (2013). "Constitutive relationship model of TC21 alloy based on artificial neural network". In: *Transactions of Nonferrous Metals Society of China* 23.6, pp. 1761–1765. DOI: [10.1016/s1003-6326\(13\)62658-8](https://doi.org/10.1016/s1003-6326(13)62658-8).
- Han, Ying et al. (2013). "A comparative study on constitutive relationship of as-cast 904L austenitic stainless steel during hot deformation based on Arrhenius-type and artificial neural network models". In: *Computational Materials Science* 67, pp. 93–103. DOI: [10.1016/j.commatsci.2012.07.028](https://doi.org/10.1016/j.commatsci.2012.07.028).
- He, An et al. (2013). "A comparative study on Johnson–Cook, modified Johnson–Cook and Arrhenius-type constitutive models to predict the high temperature

- flow stress in 20CrMo alloy steel". In: *Materials and Design* 52, pp. 677–685. DOI: [10.1016/j.matdes.2013.06.010](https://doi.org/10.1016/j.matdes.2013.06.010).
- He, Dao Guang et al. (2018a). "Microstructural evolution and support vector regression model for an aged Ni-based superalloy during two-stage hot forming with stepped strain rates". In: *Materials and Design* 154, pp. 51–62. DOI: [10.1016/j.matdes.2018.05.022](https://doi.org/10.1016/j.matdes.2018.05.022).
- He, Jianli et al. (2018b). "A modified Johnson-Cook model for 10%Cr steel at elevated temperatures and a wide range of strain rates". In: *Materials Science and Engineering: A* 715, pp. 1–9. DOI: [10.1016/j.msea.2017.10.037](https://doi.org/10.1016/j.msea.2017.10.037).
- Hedayati, N., R. Madoliat, and R. Hashemi (2017). "Strain measurement and determining coefficient of plastic anisotropy using digital image correlation (DIC)". In: *Mechanics & Industry* 18.3, p. 311. DOI: [10.1051/meca/2016060](https://doi.org/10.1051/meca/2016060).
- Honarpisheh, M., M. J. Abdolhoseini, and S. Amini (2015). "Experimental and numerical investigation of the hot incremental forming of Ti-6Al-4V sheet using electrical current". In: *The International Journal of Advanced Manufacturing Technology* 83.9-12, pp. 2027–2037. DOI: [10.1007/s00170-015-7717-7](https://doi.org/10.1007/s00170-015-7717-7).
- Hou, Qing Yu and Jing Tao Wang (2010). "A modified Johnson-Cook constitutive model for Mg–Gd–Y alloy extended to a wide range of temperatures". In: *Computational Materials Science* 50, pp. 147–152. DOI: [10.1016/j.commatsci.2010.07.018](https://doi.org/10.1016/j.commatsci.2010.07.018).
- Huang, Changqing, Xiaodong Jia, and Zhiwu Zhang (2018). "A Modified Back Propagation Artificial Neural Network Model Based on Genetic Algorithm to Predict the Flow Behavior of 5754 Aluminum Alloy". In: *Materials* 11.5, p. 855. DOI: [10.3390/ma11050855](https://doi.org/10.3390/ma11050855).
- Jawale, Kishore et al. (2018). "Microstructural investigation and lubrication study for single point incremental forming of copper". In: *International Journal of Solids and Structures* 151, pp. 145–151. DOI: [10.1016/j.ijsolstr.2017.09.018](https://doi.org/10.1016/j.ijsolstr.2017.09.018).

- Jeon, Chi-Hoon et al. (2014). "Material properties of graphene/aluminum metal matrix composites fabricated by friction stir processing". In: *International Journal of Precision Engineering and Manufacturing* 15.6, pp. 1235–1239. DOI: [10.1007/s12541-014-0462-2](https://doi.org/10.1007/s12541-014-0462-2).
- Ji, Guoliang et al. (2011). "A comparative study on Arrhenius-type constitutive model and artificial neural network model to predict high-temperature deformation behaviour in Aermet100 steel". In: *Materials Science and Engineering: A* 528.13-14, pp. 4774–4782. DOI: <https://doi.org/10.1016/j.msea.2011.03.017>.
- Jiang, Yu Qiang et al. (2018). "Isothermal tensile deformation behaviors and fracture mechanism of Ti-5Al-5Mo-5V-1Cr-1Fe alloy in  $\beta$  phase field". In: *Vacuum* 156, 187–197. DOI: [10.1016/j.vacuum.2018.08.020](https://doi.org/10.1016/j.vacuum.2018.08.020).
- Kirbach, C. et al. (2015). "Digital Image Correlation Used for Experimental Investigations of Al/Mg Compounds". In: *Strain* 51.3, pp. 223–234. DOI: [10.1111/str.12135](https://doi.org/10.1111/str.12135).
- Krishnan, S.A. et al. (2011). "Prediction of high temperature flow stress in 9Cr–1Mo ferritic steel during hot compression". In: *International Journal of Pressure Vessels and Piping* 88.11-12, pp. 501–506. DOI: [10.1016/j.ijpvp.2011.07.009](https://doi.org/10.1016/j.ijpvp.2011.07.009).
- Kumar, Ajay and Vishal Gulati (2019). "Experimental investigation and optimization of surface roughness in negative incremental forming". In: *Measurement* 131, pp. 419–430. DOI: [10.1016/j.measurement.2018.08.078](https://doi.org/10.1016/j.measurement.2018.08.078).
- Kumari, Minashree and Sunil Kumar Gupta (2018). "Removal of aromatic and hydrophobic fractions of natural organic matter (NOM) using surfactant modified magnetic nanoadsorbents (MNPs)". In: *Environmental Science and Pollution Research* 25.25, pp. 25565–25579. DOI: [10.1007/s11356-018-2611-0](https://doi.org/10.1007/s11356-018-2611-0).
- Kuo, Yiyo, Taho Yang, and Guan-Wei Huang (2008). "The use of grey relational analysis in solving multiple attribute decision-making problems". In: *Computers & Industrial Engineering* 55.1, pp. 80–93. DOI: [10.1016/j.cie.2007.12.002](https://doi.org/10.1016/j.cie.2007.12.002).



- Kyunghoon, Lee et al. (2017). "A Comparative Study on Arrhenius-Type Constitutive Models with Regression Methods". In: *Transactions of Materials Processing* 26.1, pp. 18–27. DOI: [10.5228/KSTP.2017.26.1.18](https://doi.org/10.5228/KSTP.2017.26.1.18).
- Lee, Chang-Whan and Dong-Yol Yang (2020). "Study on the Formability of Magnesium Alloy Sheets in the Incremental Forming Process with External Heating Sources". In: *International Journal of Precision Engineering and Manufacturing* 21.8, pp. 1519–1527. DOI: [10.1007/s12541-020-00352-6](https://doi.org/10.1007/s12541-020-00352-6).
- Lee, Jin-Hyuk et al. (2015). "Calculation of plastic strain ratio of AA1050 Al alloy sheet processed by heavy asymmetric rolling–annealing followed by light rolling–annealing". In: *Computational Materials Science* 100, pp. 45–51. DOI: [10.1016/j.commatsci.2014.09.049](https://doi.org/10.1016/j.commatsci.2014.09.049).
- Lei, Bingwang et al. (2019). "Constitutive Analysis on High-Temperature Flow Behavior of 3Cr-1Si-1Ni Ultra-High Strength Steel for Modeling of Flow Stress". In: *Metals* 9.1, p. 42. DOI: <http://dx.doi.org/10.3390/met9010042>.
- Li, Changmin et al. (2018). "Hot Deformation Behavior and Constitutive Modeling of H13-Mod Steel". In: *Metals* 8.10, p. 846. DOI: [10.3390/met8100846](https://doi.org/10.3390/met8100846).
- Li, Hong-Ying et al. (2012). "Application of artificial neural network and constitutive equations to describe the hot compressive behavior of 28CrMnMoV steel". In: *Materials & Design* 35, pp. 557–562. DOI: [10.1016/j.matdes.2011.08.049](https://doi.org/10.1016/j.matdes.2011.08.049).
- Li, Hong Ying et al. (2013a). "A comparative study on modified Johnson Cook, modified Zerilli-Armstrong and Arrhenius-type constitutive models to predict the hot deformation behavior in 28CrMnMoV steel". In: *Materials and Design* 49, pp. 493–501. DOI: [10.1016/j.matdes.2012.12.083](https://doi.org/10.1016/j.matdes.2012.12.083).
- Li, Hong-Ying et al. (2013b). "A modified Johnson Cook model for elevated temperature flow behavior of T24 steel". In: *Materials Science and Engineering: A* 577, pp. 138–146. DOI: <http://dx.doi.org/10.1016/j.msea.2013.04.041>.



- Li, Huabing et al. (2016). "Deformation Characteristic and Constitutive Modeling of 2707 Hyper Duplex Stainless Steel under Hot Compression". In: *Metals* 6.9, p. 223. DOI: [10.3390/met6090223](https://doi.org/10.3390/met6090223).
- Li, Huiping et al. (2013c). "Constitutive relationships of hot stamping boron steel B1500HS based on the modified Arrhenius and Johnson–Cook model". In: *Materials Science and Engineering: A* 580, pp. 330–348. DOI: <http://dx.doi.org/10.1016/j.msea.2013.05.023>.
- Liang, Zhenglong and Qi Zhang (2018). "Quasi-Static Loading Responses and Constitutive Modeling of Al–Si–Mg alloy". In: *Metals* 8.10, p. 838. DOI: [10.3390/met8100838](https://doi.org/10.3390/met8100838).
- Lin, Y. C. and Xiao Min Chen (2011). "A critical review of experimental results and constitutive descriptions for metals and alloys in hot working". In: *Materials and Design* 32 (4), pp. 1733–1759. DOI: [10.1016/j.matdes.2010.11.048](https://doi.org/10.1016/j.matdes.2010.11.048).
- Lin, Y. C., Xiao Min Chen, and Ge Liu (2010). "A modified Johnson–Cook model for tensile behaviors of typical high-strength alloy steel". In: *Materials Science and Engineering A* 527, pp. 6980–6986. DOI: [10.1016/j.msea.2010.07.061](https://doi.org/10.1016/j.msea.2010.07.061).
- Lin, Y. C. et al. (2018). "Phase transformation and constitutive models of a hot compressed TC18 titanium alloy in the  $\alpha+\beta$  regime". In: *Vacuum* 157, pp. 83–91. DOI: [10.1016/j.vacuum.2018.08.020](https://doi.org/10.1016/j.vacuum.2018.08.020).
- Liu, Zhaobing (2018). "Heat-assisted incremental sheet forming: a state-of-the-art review". In: *The International Journal of Advanced Manufacturing Technology* 98.9-12, pp. 2987–3003. DOI: [10.1007/s00170-018-2470-3](https://doi.org/10.1007/s00170-018-2470-3).
- Liu, Zhaobing, Yanle Li, and Paul A. Meehan (2014). "Tool path strategies and deformation analysis in multi-pass incremental sheet forming process". In: *The International Journal of Advanced Manufacturing Technology* 75.1-4, pp. 395–409. DOI: [10.1007/s00170-014-6143-6](https://doi.org/10.1007/s00170-014-6143-6).

- MA, Ming long et al. (2011). "Establishment and application of flow stress models of Mg-Y-MM-Zr alloy". In: *Transactions of Nonferrous Metals Society of China* 21.4, pp. 857–862. DOI: [10.1016/s1003-6326\(11\)60793-0](https://doi.org/10.1016/s1003-6326(11)60793-0).
- Maheshwari, Amit Kumar (2013). "Prediction of flow stress for hot deformation processing". In: *Computational Materials Science* 69, pp. 350–358. DOI: [10.1016/j.commatsci.2012.11.054](https://doi.org/10.1016/j.commatsci.2012.11.054).
- Mandal, Sumantra et al. (2009). "Constitutive equations to predict high temperature flow stress in a Ti-modified austenitic stainless steel". In: *Materials Science and Engineering: A* 500.1-2, pp. 114–121. DOI: [10.1016/j.msea.2008.09.019](https://doi.org/10.1016/j.msea.2008.09.019).
- Maqbool, Fawad and Markus Bambach (2018). "Dominant deformation mechanisms in single point incremental forming (SPIF) and their effect on geometrical accuracy". In: *International Journal of Mechanical Sciences* 136, pp. 279–292. DOI: [10.1016/j.ijmecsci.2017.12.053](https://doi.org/10.1016/j.ijmecsci.2017.12.053).
- (2019). "Experimental and Numerical Investigation of the Influence of Process Parameters in Incremental Sheet Metal Forming on Residual Stresses". In: *Journal of Manufacturing and Materials Processing* 3.2, p. 31. DOI: [10.3390/jmmp3020031](https://doi.org/10.3390/jmmp3020031).
- Memicoglu, P., O. Music, and C. Karadogan (2017). "Simulation of incremental sheet forming using partial sheet models". In: *Procedia Engineering* 207, pp. 831–835. DOI: [10.1016/j.proeng.2017.10.837](https://doi.org/10.1016/j.proeng.2017.10.837).
- Min, Junying et al. (2018). "Experimental and numerical investigation on incremental sheet forming with flexible die-support from metallic foam". In: *Journal of Manufacturing Processes* 31, pp. 605–612. DOI: [10.1016/j.jmapro.2017.12.013](https://doi.org/10.1016/j.jmapro.2017.12.013).
- Mirnia, Mohammad Javad and Mohsen Shamsari (2017). "Numerical prediction of failure in single point incremental forming using a phenomenological ductile fracture criterion". In: *Journal of Materials Processing Technology* 244, pp. 17–43. DOI: [10.1016/j.jmatprotec.2017.01.029](https://doi.org/10.1016/j.jmatprotec.2017.01.029).

- Mirone, G. and D. Corallo (2010). "A local viewpoint for evaluating the influence of stress triaxiality and Lode angle on ductile failure and hardening". In: *International Journal of Plasticity* 26.3, pp. 348–371. DOI: [10.1016/j.ijplas.2009.07.006](https://doi.org/10.1016/j.ijplas.2009.07.006).
- Mirzadeh, H. and A. Najafizadeh (2010). "Flow stress prediction at hot working conditions". In: *Materials Science and Engineering: A* 527.4-5, pp. 1160–1164. DOI: [10.1016/j.msea.2009.09.060](https://doi.org/10.1016/j.msea.2009.09.060).
- Mirzaie, Tina, Hamed Mirzadeha, and Jose Maria Cabrerab (2016). "'A simple Zerilli–Armstrong constitutive equation for modeling and prediction of hot deformation flow stress of steels'". In: *Mechanics of Materials* 94, pp. 38–45. DOI: [10.1016/j.mechmat.2015.11.013](https://doi.org/10.1016/j.mechmat.2015.11.013).
- Mohanraj, Murugesan, Kang Beom-Soo, and Lee Kyunghoon (2015). "Multi-Objective Design Optimization of Composite Stiffened Panel Using Response Surface Methodology". In: *Composites Research* 28.5, pp. 297–310. DOI: [10.7234/composres.2015.28.5.297](https://doi.org/10.7234/composres.2015.28.5.297).
- Murugesan, Mohanraj and Dong Jung (2019a). "Johnson Cook Material and Failure Model Parameters Estimation of AISI-1045 Medium Carbon Steel for Metal Forming Applications". In: *Materials* 12.4, p. 609. DOI: [10.3390/ma12040609](https://doi.org/10.3390/ma12040609).
- Murugesan, Mohanraj and Dong Won Jung (2019b). "Two flow stress models for describing hot deformation behavior of AISI-1045 medium carbon steel at elevated temperatures". In: *Heliyon* 5.4, e01347. DOI: [10.1016/j.heliyon.2019.e01347](https://doi.org/10.1016/j.heliyon.2019.e01347).
- (2021). "Formability and Failure Evaluation of AA3003-H18 Sheets in Single-Point Incremental Forming Process through the Design of Experiments". In: *Materials* 14.4, p. 808. DOI: [10.3390/ma14040808](https://doi.org/10.3390/ma14040808).
- Murugesan, Mohanraj, Muhammad Sajjad, and Dong Won Jung (2019a). "Hybrid Machine Learning Optimization Approach to Predict Hot Deformation Behavior

- of Medium Carbon Steel Material". In: *Metals* 9.12, p. 1315. DOI: [10.3390/met9121315](https://doi.org/10.3390/met9121315).
- (2019b). "Investigation On Single Point Incremental Forming Process Considering Various Tool Path Definitions". In: *International Journal of Mechanical and Production Engineering Research and Development* 9.6, pp. 511–524. DOI: [10.24247/ijmperdddec201944](https://doi.org/10.24247/ijmperdddec201944).
- (2020a). "Experimental Investigations on Incremental Sheet Forming of Commercial Aluminum Alloys for Maximum Production Quality". In: *International Journal of Mechanical Engineering and Robotics Research*, pp. 1264–1270. DOI: [10.18178/ijmerr.9.9.1264-1270](https://doi.org/10.18178/ijmerr.9.9.1264-1270).
- (2020b). "Formability evaluation of aluminum alloy sheets in incremental sheet forming process using various forming parameters". In: *International Journal of Mechanical and Production Engineering Research and Development* 10.3, pp. 6621–6632. DOI: [10.24247/ijmperdjun2020630](https://doi.org/10.24247/ijmperdjun2020630).
- (2020c). "Microstructure Evaluation and Constitutive Modeling of AISI-1045 Steel for Flow Stress Prediction under Hot Working Conditions". In: *Symmetry* 12.5, p. 782. DOI: [10.3390/sym12050782](https://doi.org/10.3390/sym12050782).
- (2021a). "Assessing Material Properties of Commercial Magnesium Alloy with Digital Image Correlation (DIC) Technique for Forming Applications". In: *Materials Science Forum* 1033, pp. 8–12. DOI: [10.4028/www.scientific.net/msf.1033.8](https://doi.org/10.4028/www.scientific.net/msf.1033.8).
- (2021b). "Experimental and Numerical Investigation of AA5052-H32 Al Alloy with U-Profile in Cold Roll Forming". In: *Materials* 14.2, p. 470. DOI: [10.3390/ma14020470](https://doi.org/10.3390/ma14020470).
- Murugesan, Mohanraj et al. (2017). "A Comparative Study of Ductile Damage Models Approaches for Joint Strength Prediction in Hot Shear Joining Process".

- In: *Procedia Engineering* 207, pp. 1689–1694. DOI: [10.1016/j.proeng.2017.10.923](https://doi.org/10.1016/j.proeng.2017.10.923).
- Oraon, Manish, Soumen Mandal, and Vinay Sharma (2020). “Investigation into the process parameter of single point incremental forming (SPIF)”. In: *Materials Today: Proceedings* 33, pp. 5218–5221. DOI: [10.1016/j.matpr.2020.02.922](https://doi.org/10.1016/j.matpr.2020.02.922).
- Ortiz, Mikel et al. (2014). “Hot Single Point Incremental Forming of Ti-6Al-4V Alloy”. In: *Key Engineering Materials* 611-612, pp. 1079–1087. DOI: [10.4028/www.scientific.net/kem.611-612.1079](https://doi.org/10.4028/www.scientific.net/kem.611-612.1079).
- Panda, Amlana, Ashok Kumar Sahoo, and Arun Kumar Rout (2016). “Multi-attribute decision making parametric optimization and modeling in hard turning using ceramic insert through grey relational analysis: A case study”. In: *Decision Science Letters*, pp. 581–592. DOI: [10.5267/j.dsl.2016.3.001](https://doi.org/10.5267/j.dsl.2016.3.001).
- Peng, Wenwen et al. (2013). “Comparative study on constitutive relationship of as-cast Ti60 titanium alloy during hot deformation based on Arrhenius-type and artificial neural network models”. In: *Materials & Design* 51, pp. 95–104. DOI: [10.1016/j.matdes.2013.04.009](https://doi.org/10.1016/j.matdes.2013.04.009).
- Pradhan, Dr. Mohan Kumar (2012). “Multi-Objective Optimization of MRR, TWR and Radial Overcut of EDMed AISI D2 Tool Steel Using Response Surface Methodology, Grey Relational Analysis And Entropy Measurement”. In: *Journal for Manufacturing Science and Production* 12.1, pp. 51–63. DOI: [10.1515/jmsp-2012-0004](https://doi.org/10.1515/jmsp-2012-0004).
- Quan, Guo zheng et al. (2013). “Prediction of flow stress in a wide temperature range involving phase transformation for as-cast Ti-6Al-2Zr-1Mo-1V alloy by artificial neural network”. In: *Materials & Design* 50, pp. 51–61. DOI: [10.1016/j.matdes.2013.02.033](https://doi.org/10.1016/j.matdes.2013.02.033).
- Raju, C., Neelkamal Haloi, and C. Sathiya Narayanan (2017). “Strain distribution and failure mode in single point incremental forming (SPIF) of multiple commercially

- pure aluminum sheets". In: *Journal of Manufacturing Processes* 30, pp. 328–335. DOI: [10.1016/j.jmapro.2017.09.033](https://doi.org/10.1016/j.jmapro.2017.09.033).
- Rana, Pritam Kumar, R. Ganesh Narayanan, and Satish V. Kailas (2019). "Friction stir spot welding of AA5052-H32/HDPE/AA5052-H32 sandwich sheets at varying plunge speeds". In: *Thin-Walled Structures* 138, pp. 415–429. DOI: [10.1016/j.tws.2019.02.016](https://doi.org/10.1016/j.tws.2019.02.016).
- Rauch, Matthieu et al. (2009). "Tool path programming optimization for incremental sheet forming applications". In: *Computer-Aided Design* 41.12, pp. 877–885. DOI: [10.1016/j.cad.2009.06.006](https://doi.org/10.1016/j.cad.2009.06.006).
- Razavi, S V et al. (2011). "Artificial neural networks for mechanical strength prediction of lightweight mortar". In: *Scientific Research and Essays* 6.16, pp. 3406–3417. DOI: [10.5897/sre11.311](https://doi.org/10.5897/sre11.311).
- Ren, Fa cai and Jun Chen (2013). "Modeling Flow Stress of 70Cr3Mo Steel Used for Back-Up Roll During Hot Deformation Considering Strain Compensation". In: *Journal of Iron and Steel Research International* 20.11, pp. 118–124. DOI: [10.1016/S1006-706X\(13\)60206-X](https://doi.org/10.1016/S1006-706X(13)60206-X).
- Ren, Feng Zhang et al. (2013). "Constitutive Equation of Mg-3.5Zn-0.6Y-0.5Zr Alloy under Hot Compression Deformation". In: *Advanced Materials Research* 800, pp. 271–275. DOI: [10.4028/www.scientific.net/amr.800.271](https://doi.org/10.4028/www.scientific.net/amr.800.271).
- Ren, Huaqing et al. (2019). "In-situ springback compensation in incremental sheet forming". In: *CIRP Annals* 68.1, pp. 317–320. DOI: [10.1016/j.cirp.2019.04.042](https://doi.org/10.1016/j.cirp.2019.04.042).
- Rokni, M. R. et al. (2014). "The Strain-Compensated Constitutive Equation for High Temperature Flow Behavior of an Al-Zn-Mg-Cu Alloy". In: *Journal of Materials Engineering and Performance* 23.11, pp. 4002–4009. DOI: [10.1007/s11665-014-1195-1](https://doi.org/10.1007/s11665-014-1195-1).

- Said, L. Ben et al. (2016). "Effects of the tool path strategies on incremental sheet metal forming process". In: *Mechanics & Industry* 17.4, p. 411. DOI: [10.1051/meca/2015094](https://doi.org/10.1051/meca/2015094).
- (2017). "Numerical prediction of the ductile damage in single point incremental forming process". In: *International Journal of Mechanical Sciences* 131-132, pp. 546–558. DOI: [10.1016/j.ijmecsci.2017.08.026](https://doi.org/10.1016/j.ijmecsci.2017.08.026).
- Saidi, Badreddine et al. (2015). "Experimental force measurements in single point incremental sheet forming SPIF". In: *Mechanics & Industry* 16.4, p. 410. DOI: [10.1051/meca/2015018](https://doi.org/10.1051/meca/2015018).
- Saidi, Badreddine et al. (2017). "Experimental and Numerical Study on Force Reduction in SPIF by Using Response Surface". In: pp. 835–844. DOI: [10.1007/978-3-319-66697-6\\_81](https://doi.org/10.1007/978-3-319-66697-6_81).
- Sajjad, Muhammad, Mohanraj Murugesan, and Dong Won Jung (2020). "Longitudinal Bow Estimation of U-Shape Profile in Cold Roll Formed for Commercial Aluminum Alloys". In: *International Journal of Mechanical Engineering and Robotics Research*, pp. 1097–1103. DOI: [10.18178/ijmerr.9.8.1097-1103](https://doi.org/10.18178/ijmerr.9.8.1097-1103).
- Salehi, M., M. Saadatmand, and J. Aghazadeh Mohandesi (2012). "Optimization of process parameters for producing AA6061/SiC nanocomposites by friction stir processing". In: *Transactions of Nonferrous Metals Society of China* 22.5, pp. 1055–1063. DOI: [10.1016/s1003-6326\(11\)61283-1](https://doi.org/10.1016/s1003-6326(11)61283-1).
- Samantaray, D., S. Mandal, and A.K. Bhaduri (2009). "A comparative study on Johnson Cook, modified Zerilli–Armstrong and Arrhenius-type constitutive models to predict elevated temperature flow behaviour in modified 9Cr–1Mo steel". In: *Computational Materials Science* 47.2, pp. 568–576. DOI: [10.1016/j.commatsci.2009.09.025](https://doi.org/10.1016/j.commatsci.2009.09.025).

- Sankar, BR and P Umamaheswarrao (2016). "Optimisation of hardness and tensile strength of friction stir welded AA6061 alloy using response surface methodology coupled with grey relational analysis and principle component analysis". In: *International Journal of Engineering, Science and Technology* 7.4, p. 21. DOI: [10.4314/ijest.v7i4.3](https://doi.org/10.4314/ijest.v7i4.3).
- Sbayti, Manel et al. (2016). "Finite Element Analysis of hot Single Point Incremental forming of hip prostheses". In: *MATEC Web of Conferences* 80. Ed. by K. Saanouni, p. 14006. DOI: [10.1051/mateconf/20168014006](https://doi.org/10.1051/mateconf/20168014006).
- Shrot, Aviral and Martin Baker (2012). "Determination of Johnson–Cook parameters from machining simulations". In: *Computational Materials Science* 52.1, pp. 298–304. DOI: [10.1016/j.commatsci.2011.07.035](https://doi.org/10.1016/j.commatsci.2011.07.035).
- Siamak, Serajzadeh (2007). "Prediction of temperature distribution and required energy in hot forging process by coupling neural networks and finite element analysis". In: *Materials Letters* 61 (14-15), pp. 3296–3300. DOI: [10.1016/j.matlet.2006.11.056](https://doi.org/10.1016/j.matlet.2006.11.056).
- Singh, Bhupinder and J.P. Misra (2019). "Surface finish analysis of wire electric discharge machined specimens by RSM and ANN modeling". In: *Measurement* 137, pp. 225–237. DOI: [10.1016/j.measurement.2019.01.044](https://doi.org/10.1016/j.measurement.2019.01.044).
- Sivaiah, P. and D. Chakradhar (2019). "Modeling and optimization of sustainable manufacturing process in machining of 17-4 PH stainless steel". In: *Measurement* 134, pp. 142–152. DOI: [10.1016/j.measurement.2018.10.067](https://doi.org/10.1016/j.measurement.2018.10.067).
- Slooff, F.A. et al. (2007). "Constitutive analysis of wrought magnesium alloy Mg–Al4–Zn1". In: *Scripta Materialia* 57.8, pp. 759–762. DOI: [10.1016/j.scriptamat.2007.06.023](https://doi.org/10.1016/j.scriptamat.2007.06.023).
- Song, Qinbao and Martin Shepperd (2011). "Predicting software project effort: A grey relational analysis based method". In: *Expert Systems with Applications* 38.6, pp. 7302–7316. DOI: [10.1016/j.eswa.2010.12.005](https://doi.org/10.1016/j.eswa.2010.12.005).



- Song, Weidong et al. (2013). “A modified Johnson-Cook model for titanium matrix composites reinforced with titanium carbide particles at elevated temperatures”. In: *Materials Science and Engineering A* 576, pp. 280–289. DOI: [10.1016/j.msea.2013.04.014](https://doi.org/10.1016/j.msea.2013.04.014).
- Stendal, Johan et al. (2019). “Applying Machine Learning to the Phenomenological Flow Stress Modeling of TNM-B1”. In: *Metals* 9.2, p. 220. DOI: [10.3390/met9020220](https://doi.org/10.3390/met9020220).
- Su, Yu et al. (2020). “Multi-Objective Optimization of Cutting Parameters in Turning AISI 304 Austenitic Stainless Steel”. In: *Metals* 10.2, p. 217. DOI: [10.3390/met10020217](https://doi.org/10.3390/met10020217).
- Sun, Mingyue et al. (2011). “Modeling flow stress constitutive behavior of SA508-3 steel for nuclear reactor pressure vessels”. In: *Journal of Nuclear Materials* 418.1-3, pp. 269–280. DOI: [10.1016/j.jnucmat.2011.07.011](https://doi.org/10.1016/j.jnucmat.2011.07.011).
- Sy, Le Van and Nguyen Thanh Nam (2013). “Hot incremental forming of magnesium and aluminum alloy sheets by using direct heating system”. In: *Proceedings of the Institution of Mechanical Engineers, Part B: Journal of Engineering Manufacture* 227.8, pp. 1099–1110. DOI: [10.1177/0954405413484014](https://doi.org/10.1177/0954405413484014).
- Tan, Jin Qiang et al. (2015). “A modified Johnson-Cook model for tensile flow behaviors of 7050-T7451 aluminum alloy at high strain rates”. In: *Materials Science and Engineering A* 631, pp. 214–219. DOI: [10.1016/j.msea.2015.02.010](https://doi.org/10.1016/j.msea.2015.02.010).
- Tomáš, Miroslav et al. (2019). “Physical Modelling and Numerical Simulation of the Deep Drawing Process of a Box-Shaped Product Focused on Material Limits Determination”. In: *Metals* 9.10, p. 1058. DOI: [10.3390/met9101058](https://doi.org/10.3390/met9101058).
- Tonday, Hulas Raj and Anand Mukut Tigga (2019). “An empirical evaluation and optimization of performance parameters of wire electrical discharge machining in cutting of Inconel 718”. In: *Measurement* 140, pp. 185–196. DOI: [10.1016/j.measurement.2019.04.003](https://doi.org/10.1016/j.measurement.2019.04.003).

- Tonietto, Leandro et al. (2019). "New Method for Evaluating Surface Roughness Parameters Acquired by Laser Scanning". In: *Scientific Reports* 9.1. DOI: [10.1038/s41598-019-51545-7](https://doi.org/10.1038/s41598-019-51545-7).
- Udroiu, Razvan, Ion Braga, and Anisor Nedelcu (2019). "Evaluating the Quality Surface Performance of Additive Manufacturing Systems: Methodology and a Material Jetting Case Study". In: *Materials* 12.6, p. 995. DOI: [10.3390/ma12060995](https://doi.org/10.3390/ma12060995).
- Vahdani, Mostafa et al. (2019). "Electric hot incremental sheet forming of Ti-6Al-4V titanium, AA6061 aluminum, and DC01 steel sheets". In: *The International Journal of Advanced Manufacturing Technology* 103.1-4, pp. 1199–1209. DOI: [10.1007/s00170-019-03624-2](https://doi.org/10.1007/s00170-019-03624-2).
- Wang, Peng, Zhouquan Zhu, and Yonghu Wang (2016). "A novel hybrid MCDM model combining the SAW, TOPSIS and GRA methods based on experimental design". In: *Information Sciences* 345, pp. 27–45. DOI: [10.1016/j.ins.2016.01.076](https://doi.org/10.1016/j.ins.2016.01.076).
- Wang, Xiangyu et al. (2013). "Dynamic behavior and a modified Johnson–Cook constitutive model of Inconel 718 at high strain rate and elevated temperature". In: *Materials Science and Engineering A* 580, pp. 385–390. DOI: [10.1016/j.msea.2013.05.062](https://doi.org/10.1016/j.msea.2013.05.062).
- Wang, Y. H. et al. (2010). "Whole field sheet-metal tensile test using digital image correlation". In: *Experimental Techniques* 34.2, pp. 54–59. DOI: [10.1111/j.1747-1567.2009.00483.x](https://doi.org/10.1111/j.1747-1567.2009.00483.x).
- Wei, Hongyu et al. (2019). "Investigation on the influence of springback on precision of symmetric-cone-like parts in sheet metal incremental forming process". In: *International Journal of Lightweight Materials and Manufacture* 2.2, pp. 140–145. DOI: [10.1016/j.ijlmm.2019.05.002](https://doi.org/10.1016/j.ijlmm.2019.05.002).
- Wu, Yuna et al. (2021). "Joint effect of micro-sized Si particles and nano-sized dispersoids on the flow behavior and dynamic recrystallization of near-eutectic Al–Si

- based alloys during hot compression". In: *Journal of Alloys and Compounds* 856, p. 158072. DOI: [10.1016/j.jallcom.2020.158072](https://doi.org/10.1016/j.jallcom.2020.158072).
- Xiao, X. et al. (2012). "A comparative study on Arrhenius-type constitutive equations and artificial neural network model to predict high-temperature deformation behaviour in 12Cr3WV steel". In: *Computational Materials Science* 62, pp. 227–234. DOI: [10.1016/j.commatsci.2012.05.053](https://doi.org/10.1016/j.commatsci.2012.05.053).
- Xiao, Xiao et al. (2020). "RSM and BPNN Modeling in Incremental Sheet Forming Process for AA5052 Sheet: Multi-Objective Optimization Using Genetic Algorithm". In: *Metals* 10.8, p. 1003. DOI: [10.3390/met10081003](https://doi.org/10.3390/met10081003).
- Yang, Li-Chih et al. (2015). "Constitutive Relationship Modeling and Characterization of Flow Behavior under Hot Working for Fe–Cr–Ni–W–Cu–Co Super-Austenitic Stainless Steel". In: *Metals* 5.3, pp. 1717–1731. DOI: <http://dx.doi.org/10.3390/met5031717>.
- Zhan, Hongyi et al. (2014). "Constitutive modelling of the flow behaviour of a titanium alloy at high strain rates and elevated temperatures using the Johnson–Cook and modified Zerilli–Armstrong models". In: *Materials Science and Engineering: A* 612, pp. 71–79. DOI: [10.1016/j.msea.2014.06.030](https://doi.org/10.1016/j.msea.2014.06.030).
- Zhang, Hongjian et al. (2009). "A modified Zerilli–Armstrong model for alloy IC10 over a wide range of temperatures and strain rates". In: *Materials Science and Engineering A* 527 (1-2), pp. 328–333. DOI: [10.1016/j.msea.2009.08.008](https://doi.org/10.1016/j.msea.2009.08.008).
- Zhang, Yan et al. (2019). "Avrami Kinetic-Based Constitutive Relationship for Armco-Type Pure Iron in Hot Deformation". In: *Metals* 9.3, p. 365. DOI: [10.3390/met9030365](https://doi.org/10.3390/met9030365).
- Zhanga, Y., J.C. Outeirob, and T. Mabroukic (2015). "On the selection of Johnson–Cook constitutive model parameters for Ti-6Al-4V using three types of numerical models of orthogonal cutting". In: *In Proceedings of the 15th CIRP Conference on Modelling of Machining Operations*, pp. 112–117.

- Zhu, Yanchun et al. (2011). "Artificial neural network approach to predict the flow stress in the isothermal compression of as-cast TC21 titanium alloy". In: *Computational Materials Science* 50.5, pp. 1785–1790. DOI: [10.1016/j.commatsci.2011.01.015](https://doi.org/10.1016/j.commatsci.2011.01.015).
- Zhuang, Xincun et al. (2012). "Experimental Methodology for Obtaining the Flow Curve of Sheet Materials in a Wide Range of Strains". In: *steel research international* 84.2, pp. 146–154. DOI: [10.1002/srin.201200104](https://doi.org/10.1002/srin.201200104).